Dissertation

submitted to the
Combined Faculties for the Natural Sciences and for Mathematics
of the Ruperto-Carola University of Heidelberg, Germany
for the degree of
Doctor of Natural Sciences

Presented by
Dipl.-Phys. Johannes David Goullon
born in
Heppenheim

Oral examination: 30.04.2014

One- and two-electron processes in charge transfer and single ionization in ion-lithium collisions

Referees: **Priv.-Doz. Dr. Daniel Fischer**
Prof. Dr. Andreas Wolf

Zusammenfassung

In dieser Arbeit werden ein- und zwei-Elektronenübergänge in Kollisionen von Ionen mit Lithium untersucht. Die Messungen werden mit einem neuartigen experimentellen Aufbau (MOTReMi) durchgeführt, der eine magneto-optische Falle (MOT) für ein Lithium Target mit einem Reaktionsmikroskop (ReMi) kombiniert, was eine impulsaufgelöste und koinzidente Detektion der Targetfragmente ermöglicht. Dieser Aufbau war in dem Ionenspeicherring TSR integriert, der elektronengekühlte Projektilstrahlen mit hohen Strömen und kleiner Impulsbreite bereitstellte. Die hohe Auflösung und die Möglichkeit optischer Anregung erlaubten zum ersten Mal die Messung zustands-selektiver volldifferentieller Wirkungsquerschnitte für Ionisation und Ladungstransfer durch Ionenstoß. Dabei wurden Übergänge der $1s$, $2s$ und $2p$ Elektronen des Lithium Targets untersucht, die Aufschluss über die Rolle der Projektilkohärenz, die Elektronenkorrelation in zwei-Elektronenübergängen sowie Target Polarisationseffekte geben, was zu einem besseren Verständnis des Mehr-Teilchen Problems der Quantendynamik beiträgt.

Abstract

In this work the dynamics of one- and two-electron transitions in ion-lithium collisions is investigated. The measurements are performed with a novel experimental technique (MOTReMi) combining a magneto-optically trapped (MOT) Li target with a Reaction Microscope (ReMi) enabling the momentum resolved and coincident detection of the target fragments. This apparatus was implemented in the ion storage ring TSR providing electron-cooled projectile beams with high currents and low momentum spread. Due to the high resolution and by means of optical excitation, for the first time initial state selective fully differential cross sections for ion-impact induced ionization and charge transfer became available. Transitions of $1s$, $2s$ and $2p$ target electrons were investigated shedding light on the role of the projectile coherence length, electronic correlation in two-electron transitions and target polarization effects, thereby enhancing our understanding of the few-body problem in quantum dynamics.

Contents

1. Introduction

One of the most fundamental problems in physics is the so-called few-body problem, which arises because the equations of motions can generally not be solved analytically for more than two mutually interacting particles. For non-relativistic atomic systems the equation of motion is given by the Schrödinger equation. Though the underlying interaction, the Coulomb force, is precisely known, also here the exact quantum state can not be calculated analytically. Hence numerical methods or approximations have to be used to obtain solutions. Atomic collision physics is a well suited testing ground for theoretical approaches tackling the few-body problem. On the one hand, controlling and varying the number of interacting particles is very easy, and on the other hand, the underlying Coulomb force is well understood.

In the last 15 years, the theoretical description of dynamic atomic few-body systems experienced substantial advancements. With the development of numerical methods like exterior complex scaling (ECS) (Rescigno et al., 1999) or convergent close coupling (CCC) (Bray, 2002) the momentum balance e.g. in electron impact ionization of hydrogen or photo double ionization of helium is predicted with tremendous precision. These methods are, however, not directly applicable to ion-atom collisions, because approximations like the partial wave expansion do (at typical collision velocities) not converge for ionic projectiles. For such systems perturbative methods, most prominent the continuum distorted wave - eikonal initial state (CDW-EIS) (Crothers and McCann, 1983), have been developed which are expected to provide reasonable agreement to experiment at least for sufficiently 'weak' interaction between projectile and target, i.e. for small perturbations. The perturbation parameter is given by $\eta = Z_p/v_p$ (Z_p and v_p are projectile charge and velocity, respectively) and corresponds to the expansion parameter in the Born series (Born, 1926). Most notably, ions represent a particular versatile class of projectiles because they allow accessing (by varying their charge and velocity) a much wider range of perturbations than e.g. electrons, and in relativistic collisions with highly charged ions even short (and most intense electro-magnetic pulses) can be generated in a regime that is not accessible by any other experimental method.

Also from the experimental side, the study of atomic collision dynamics experienced a boost in the last two decades. Though the first measurement of fully differential

cross sections FDCS (i.e. which are not integrated over any component in the final momentum space) was reported already in (Ehrhardt et al., 1969), again this technique is not directly applicable to ion collisions. In this experiment, the angular correlation of the two outgoing electrons in singly-ionizing electron-helium collision was studied for fixed electron energies by using two detectors to detect the electron projectile and the ionized electron, each of which covering only a very small fraction of the full solid angle. The angular emission characteristics could only be measured by moving the detectors, i.e. changing the setup mechanically. Such very involving and time-consuming measurements became obsolete with the advent of reaction microscopes (ReMi) (Ullrich et al., 2003). Here, electric and magnetic fields enable a 4π acceptance for electrons and ions. This way FDCS became for the first time accessible also for ionization by heavy projectiles (Schulz et al., 2003), where the projectile momentum change is often immeasurable small (or can be obtained only with very limited resolution).

These advanced theoretical and experimental techniques triggered detailed investigations of many processes occurring in ion atom collisions. A rather simple class of reactions are one-electron processes, where only one (target) electron undergoes a transition during the collision process. There are essentially two possibilities (resulting in the creation of a target ion): Single ionization and single electron capture.

Total cross-sections of ion-impact induced single ionization have been studied since many years (for a review see (Cocke and Olson, 1991)). Later measurements were differential in the angle and energy of the emitted electron (a review is given in (Rudd et al., 1992)) or in the transverse momentum change of the projectile or recoil ion (e.g. (Schuch et al., 1988; Ullrich et al., 1989)). A first kinematically complete experiment using a ReMi was reported in (Moshammer et al., 1994). In the following, the CDW-EIS theory achieved excellent agreement with experimental data for doubly differential electron emission spectra for ion-impact ionization of helium, even for large perturbations (Rodriguez and Barrachina, 1998; Moshammer et al., 1999). However, puzzling discrepancies between theory and experimental data were observed in doubly differential cross sections including the three particle momentum exchange (Moshammer et al., 2001) as well as in fully differential cross sections throughout all perturbation regimes (Fischer et al., 2003b; Schulz et al., 2001; Schulz et al., 2003; Foster et al., 2006), that are not fully resolved until today.

Single electron capture gained considerable interest already in the early days of quantum physics. It was reported in (Davis, 1923) for α particles swiftly moving through a gas, where single or double electron capture from the gas to the bare helium ion was observed. Later experiments measured the charge state of helium and found clear evidences for electron capture (Rutherford, 1924; Davis and Barnes, 1929). In (Thomas, 1927) a capture process involving two steps was proposed, where the electron scatters at the projectile and the target, while other theoretical investigations described the capture as a matter of velocity matching of the electron and the projectile (Oppenheimer, 1928; Brinkmann and Kramers, 1930). Even nowadays single electron capture is subject of investigation, theoretically (Mancev et al., 2003; Vinitsky et al., 2005), and experimentally (Horsdal-Pedersen et al., 1983; Fischer et al., 2006). One- and two step capture processes could be separated clearly and qualitative agreement with state-of-the-art calculations was achieved, however, even in this simple process quantitative discrepancies between experiment and theory remain.

For two-electron processes our knowledge is generally more incomplete, as now four particles are involved in the collision. Typical processes are double ionization (Moshammer et al., 1996; Fischer et al., 2003b), mutual projectile and target ionization (Montenegro et al., 1992; Wang et al., 2011), ionization-excitation and transfer ionization, the two latter being investigated in this work.

In ionization-excitation one target electron is excited and another one emitted into the continuum. This process was already observed in ion-lithium collisions by electron auger spectroscopy (Tanis et al., 1999). For electron-helium collisions this process was used to investigate the strong correlation of the two K-shell electrons (Sakhelashvili et al., 2005; Bellm et al., 2006; Ngoko Djiokap et al., 2010; Zatsarinny and Bartschat, 2011).

In transfer ionization (TI) one electron is captured by the projectile, while another one is ionized, leaving the target atom doubly ionized. Two main processes can be distinguished: correlated TI, where the electron-electron interactions are responsible for the emission and/or capture of the second electron (Thomas, 1927; Briggs and Taulbjerg, 1979), and independent TI, where the projectile interacts with each electron (Belkic et al., 1984; Gayet and Salin, 1991). While these two processes can be distinguished clearly in measurements (Mergel et al., 1997; Schneider, 2012), a new correlated TI mechanism was found in (Voitkiv et al., 2008), in qualitative agreement with experimental observations (Mergel et al., 2001; Schulz et al., 2012).

The discrepancies between theory an experiment are, in particular for the one electron processes, very puzzling and were vividly debated in the last decade. While first only the validity of theoretical approximations regarding the target structure (which was in most experiments a helium atom) or the interaction between projectile and target was considered (Voitkiv et al., 2003; Fiol et al., 2006; Schulz et al., 2007; McGovern et al., 2010), in the last two years the investigations start to focus on another effect which is controversially discussed (Colgan et al., 2011; Walters and Whelan, 2012; Wang et al., 2012; Kouzakov et al., 2012; Schulz et al., 2013; Kouzakov et al., 2013; Feagin and Hargreaves, 2013) but at the same time maybe most promising: The influence of the projectile coherence on the collision dynamics. In (Egodapitiya et al., 2011; Sharma et al., 2012) influences of the projectile coherence length in proton-H_2 collisions were reported, triggering a closer look at the measurement conditions in (Schulz et al., 2003). Here the coherence length was about 10^{-3} a.u., i.e. it was much smaller than the target atom. The comparison with proton on helium collisions of the same perturbation with the much higher coherence length of 3 a.u. revealed that interference effects can be the reason for the differences in the cross sections (Wang et al., 2012). The importance of the coherence length was also reported in (Schneider et al., 2013), where the dependence on the impact parameter was shown. The emission characteristics of the electrons showed interference effects in transfer ionization (small impact parameter) and no interference in single ionization (large impact parameter). Hence, the coherence length has to be compared to the impact parameter of the observed process and not to the actual size of the atom, as already proposed by (Sarkadi, 2010).

In this thesis the aim was study the dynamics one- and two-electron processes in ion lithium collisions. Lithium became available as a target for kinematically complete studies only very recently with the development of a new experimental technique, the MOTReMi. Here the target is not a gas jet as in conventional ReMis, but a

magneto optical trap (MOT). The temperature of the MOT target is two orders of magnitude lower than in gas jets, resulting in a higher resolution of the recoil ions. It also enables the use of target atoms other than rare gases. For the present setup lithium was chosen, which has the advantage of still being a relatively simple system with only three electrons. It is possible to observe reactions of a 'hydrogen-similar' system (when the valence electron is considered) and a 'helium-similar' system (when focusing on transitions of the inner shell electrons). Another benefit of optically cooling and trapping the target is that it allows to easily excite and even polarize the target. The experiments presented in this thesis were performed in the ion storage ring TSR. This allows for high beam qualities, in particular excellent coherence properties are achieved by electron cooling.

The one-electron processes presented in this work focus on the dependence of the initial target state. Especially interesting is the single ionization of a polarized target, allowing to observe an orientational dichroism, which is a symmetry breaking in respect to the direction of the momentum transfer of the collision. Such a dichroism was already observed for electron-impact induced ionization of sodium atoms (Dorn et al., 1998); the results in this work build on previous works with the same setup (Hubele et al., 2013; Hubele, 2013).
Also presented are first results of electron capture. The measurements is quite challenging due to the rather small signal to noise ratio (the cross section for electron capture is two orders of magnitude smaller than for single ionization (*The ORNL CFADC Redbooks* 2014)) and the low target density.

The two electron process ionization-excitation for the presented ion-lithium collision is rather different than for a helium target. With a lithium target, the K-shell electron is captured and the L-shell electron ionized, hence the correlation is weak in comparison to the helium target. This gives rise to a higher order process involving two interactions with the projectile rather than a correlation between the active electrons (Fischer et al., 2012). Ionization-excitation also depends on the initial target state, enabling the investigation of this process for a polarized target.
The transfer ionization measurement is also demanding in a similar way as explained for electron capture. However, the difficulties could be overcome, thus allowing to investigate electron correlation effects of the lithium target.

The first chapter will provide basic concepts of the investigation of ion-atom collisions, including dynamics, kinematics and theoretical models (chapter 2). Chapter 3 will introduce the experimental techniques and their combination. The principles of the data analysis will be explained in chapter 4, where also a newly invented correction method will be introduced. Finally, in chapter 5 the results for the measurements are presented and discussed.

2. Ion-atom collisions

In ion-atom collisions different charge changing reaction channels can be investigated. The general reaction equation of such processes with a lithium target is

$$\mathrm{X}^{(Z_p-n_p^i)+} + \mathrm{Li}^{(*)} \rightarrow \mathrm{X}^{(Z_p-n_p^f)+,(*)} + \mathrm{Li}^{n+,(*)} + (n + n_p^i - n_p^f)\mathrm{e}^- + n_{ph}\gamma \qquad (2.1)$$

A projectile X with charge $Z_p - n_p^i$ collides with atomic lithium. After the collision the projectiles charge is $Z_p - n_p^f$, the lithium target loses n electrons and n_{ph} photons are created. For $n_p^i - n_p^f > 0$ the projectile is ionized, while for $n_p^i - n_p^f < 0$ the projectile captures an electron. The target and/or the projectile can also be excited (indicated by (*)).

The reaction channels relevant for the processes analyzed in this work are single ionization (SI), single electron capture (SC) and transfer ionization (TI). For SI it is $n_p^i - n_p^f = 0$, $n = 1$ and $n_{ph} = 0$, for SC it is $n_p^i - n_p^f = -1$, $n = 0$ and $n_{ph} = 0$ and for TI it is $n_p^i - n_p^f = -1$, $n_I = 1$ and $n_{ph} = 0$. Photon emission will not be discussed, but target excitation will be investigated. As projectiles several ion species with various charge states were used, which will be introduced in chapter 5.

In atomic collisions, the electromagnetic force is the by far dominant interaction. It is given by the Coulomb potential $\phi(t) \propto \frac{Z}{r(t)}$, where Z is the charge and $r(t)$ the distance of the collision partners, the latter depending on the velocity of the projectile v_p and the impact parameter b. In the following chapter several factors that influence the cross sections will be introduced. Subsequently, the kinematics of collision processes will be explained and a short overview over theoretical methods is given.

2.1 Characteristics of the collision system

The theoretical description of a collision process requires the knowledge of many properties of the collision partners. In this chapter these properties will be addressed.

Two particle scattering: the Rutherford cross section

In order to get a first insight in the scattering process, we will take a look at the simplest ionization mechanism, the two particle scattering. Assuming the electron being initially at rest and neglecting the target core, there are only two involved particles, the projectile and the electron. The description of such a system is given by the Rutherford scattering cross section (e.g. Rudd et al., 1992)

$$\frac{d\sigma}{dE_e} \propto \frac{2\pi}{m_e v_p^2} \left(\frac{Z_p}{W}\right)^2 \tag{2.2}$$

with the projectile charge Z_p and velocity v_p, the electron mass m_e and the energy of the electron $W = E_e + I_p$. This energy W accounts for the bound electron with an ionization potential I_p and the final energy of the free electron E_e. However, this formula approximates the cross section only for $E_e \gg I_p$, otherwise the target structure has to be considered.

In this description the target properties are ignored besides the ionization potential of the emitted electron. However, here only binary collisions between the projectile and the electron are considered – in general the target core has a strong influence on the collision properties as well.

2.1.1 Target

The target does not consist only of the electron that is ionized, but also of other electrons and a nucleus. This increasing number of involved particles complicates the theoretical description of the collision system significantly.

Electron(s)

Bound electrons have an initial velocity distribution, which is described by the Compton profile. The modification of the scattering cross section by the initial electron momentum distribution was first predicted in (Jauncey, 1925). In (Dumond, 1933) this effect was measured in the scattering of monochromatic x-rays, whose spectral width was broader after elastic scattering. In ion-atom collisions, the Compton profile depends on the quantum mechanical state of the electron and results in a broadened energy distribution of the ionized electron, which could be measured for low-energy electrons in (Moshammer et al., 1999).

All neutral atoms but the hydrogen hold more than one electron. This complicates the description of collisions in two ways: first, the potential which the electron experiences is not a Coulomb potential, but it is screened. Second, the electrons can interact with each other resulting in correlation effects.

For the effective one-electron system, the target core charge acting on the electron can be considered by introducing an effective charge Z_{eff}, allowing to use a Coulomb-like potential (Slater, 1930; Clementi and Raimondi, 1963). However, this approach does not include that the 'strength' of the screen depends on the distance of the electron to the nucleus. This effect can be included by more complex approximations, e.g. Hartree-Fock potentials, which have successfully been implemented in theories as continuum distorted wave with eikonal initial state (CDW-EIS) (Clementi and Roetti, 1974; Gulyas et al., 1995).

The correlation of the electrons is especially important in collision processes with two active electron like transfer ionization or shake-off, which will be discussed in section 2.2. However, recent calculations showed that also in SI theoretical calculations differ, whether one or two electrons are included (Colgan et al., 2011). When considering interactions between electrons explicitly, the target state cannot be described by just the product of the one-electron states (Hartree-Fock), but the modeling is much more challenging. An overview over electron correlation dynamics can be found in (McGuire, 1997).

In this work lithium is used as target atom. Here the electron correlation is very strong between the two inner-shell electrons, but very weak between $1s$ and $2s$ electrons. In earlier measurements, differences between $1s$ and $2s$ ionization were related to two- and three-body effects in (Stolterfoht et al., 1998).

Target nucleus

The target nucleus was also not included in the two particle scattering above. However, with the electron and the projectile, three particles are involved in the collision. The Coulomb field of the target nucleus affects the electron as well as the projectile.

After a collision, an emitted electron is still interacting with the Coulomb potential of the target nucleus. This is especially significant for low-energy electrons (Fainstein et al., 1996). In perturbation theory, this can be considered by choosing an appropriate wave function for the electron in the final state (specifically a Coulomb wave).

On the other hand, the projectile cannot only scatter at the electron, but also on the target nucleus. This influences the electron emission at low (Schulz et al., 2003; Madison et al., 2003) and high perturbations (Moshammer et al., 2001). These interactions have been included in theoretical models and proven to have in most cases a considerable influence (e.g. (Rodriguez and Barrachina, 1998; LaForge et al., 2013)).

2.1.2 Projectile

In the simplest case, a bare projectile has a charge Z_p and a velocity v_p. By varying these parameters, the collision characteristics can be changed. Fist order perturbation theory (see 2.3.1.1) delivers the dependance of the cross section on these parameters as $\sigma \propto \eta^2$ with $\eta = Z_p/v_p$ being the perturbation parameter: higher charge and lower velocity give rise to a larger perturbation. There is a large variety of possible perturbations in ion-atom collisions, as the charge can be varied from 1 e up to about a 100 e, while also the energy (respectively the velocity) can be changed over several orders of magnitude. Thus, the perturbation can be changed from a photon-like perturbative regime ($\eta \ll 1$) to a strongly non-perturbative regime ($\eta \geq 1$), where even quasi-molecules can form (see fig. 2.1). The lines and colors indicate the validity of different theories; for larger perturbations approaches like CDW-EIS can be used, which are applicable for $\eta' = Z_p/v_p^2$ (Crothers and McCann, 1983). These theories are discussed in section 2.3. The projectiles that will be subject of this work are also shown in this plot, ranging from $\eta = 0.1$ a.u. up to $\eta = 1.1$ a.u..

The theoretical description of these collisions is more challenging than for collisions with electron or photon projectiles, as a much higher mass is involved. Therefore,

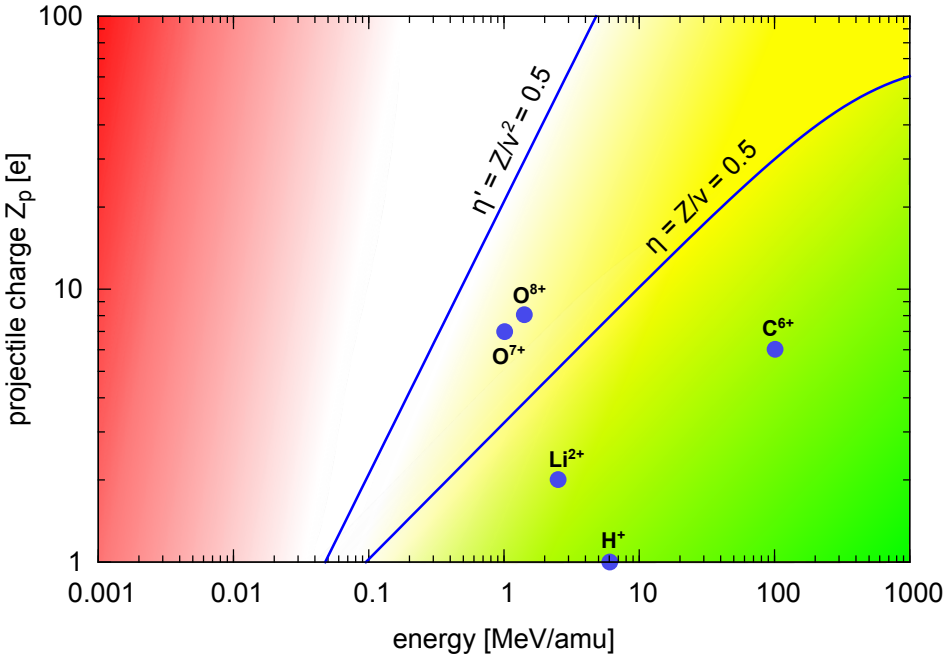

Figure 2.1: Illustration of the perturbation parameter in ion-atom collisions. For small perturbations it is given by $\eta = Z_p/v_p$. The colored areas mark the validity of different theoretical approaches: in the green area the first Born approximation and in the yellow region theories like CDW-EIS can be utilized. The red region marks a very high perturbation, where quasi-molecules can form, which can be described by molecular orbital models (Eichler and Wille, 1974).

approximations used for electron impact, e.g. partial wave expansion, are not converging for ion impact. In spite of these complications, doubly differential cross sections for electron emission up to a rather high perturbation of $\eta = 4.4$ a.u. can be described in good agreement with the CDW-EIS model (Moshammer et al., 1999). However, the same theoretical model fails in describing doubly differential cross sections including the three body momentum exchange (Moshammer et al., 2001) as well as in the case of fully differential cross sections, where discrepancies remain even for a low perturbation of $\eta = 0.1$ a.u. (Schulz et al., 2003).

2.1.3 Projectile coherence

The influence of the projectile coherence is neglected in essentially all quantum mechanical models available today. Usually, plane or distorted waves with an infinite transverse coherence length $l_\perp$ are used to describe the projectiles. However, the fact that the target can be coherently or incoherently (i.e. $l_\perp <$ target size) 'illuminated' could have a considerable influence on the cross section of the reaction.

2.1.3.1 Coherence in atomic collisions

Coherence describes the ability of waves to interfere with each other stationary. This requires a constant relative phase between them. A textbook example of interference is Young's double slit experiment (Young, 1804), where a light wave passes through two slits and the intensity of the evanescent waves is measured as a function of position. Coherent waves show a spatially oscillating interference pattern, while the intensity of two superimposed incoherent emerging waves corresponds just to the sum

of the intensity patterns of two single slits. The interference pattern is composed of maxima (constructive interference) and minima (destructive interference), which have a greater (smaller) amplitude than either wave. Mathematically, interference is obtained when calculating the intensity of two (or more) superimposed waves ψ_1 and ψ_2:

$$\begin{aligned} I(\mathbf{r}) &= |\psi_1(\mathbf{r},t) + \psi_2(\mathbf{r},t)|^2 \\ &= |\psi_1(\mathbf{r},t)|^2 + |\psi_2(\mathbf{r},t)|^2 + 2cos(\phi(t))\,|\psi_1(\mathbf{r},t)|\,|\psi_2(\mathbf{r},t)| \end{aligned} \tag{2.3}$$

where $\phi(t)$ is the phase angle between the two waves. Incoherence is the fluctuation of $\phi(t)$ in time, resulting in a vanishing interference term.

The coherence properties can be separated into longitudinal ($l_\parallel$, also called temporal) and transverse coherence ($l_\perp$, also called spatial). Similar deductions as the following can also be found e.g. in (Demtröder, 2002).

Longitudinal coherence

Longitudinal coherence describes the coherence in direction of propagation. It is defined by the time τ_c in which the wave packet can interfere with itself. At maximum, this time can be the temporal length of the wave packet. With Fourier transformation τ_c can be related to a frequency ν:

$$\Delta\tau_c \propto \frac{1}{\Delta\nu} \tag{2.4}$$

As time and length are related by the velocity v_p, the longitudinal coherence length is given by

$$\Delta l_\parallel = \Delta\tau_c v_p \propto \frac{v_p}{\Delta\nu} \tag{2.5}$$

Using $\Delta E = h\Delta\nu$, the longitudinal coherence length can be expressed with the longitudinal momentum:

$$\Delta l_\parallel \approx \frac{2h}{\Delta p_\parallel} \tag{2.6}$$

Transverse coherence

The transverse coherence can be best explained in analogy to optics (see fig. 2.2). A projectile wave propagates through a slit with the width a and diffracts at an object, e.g. a double slit with a separation Δr in distance L to the slit. According to the Huygens-Fresnel principle, each point of the slit becomes a source of a spherical wave. The path difference Δs of two waves results in a phase difference $\Delta\phi$ at the diffraction object:

$$\Delta\phi = \Delta s \frac{2\pi}{\lambda} \tag{2.7}$$

The path difference can also be related to the separation of the target, the slit distance L and the slit width a:

$$\Delta s = \Delta r \cdot \sin(\theta) \approx \Delta r \frac{a/2}{L} \tag{2.8}$$

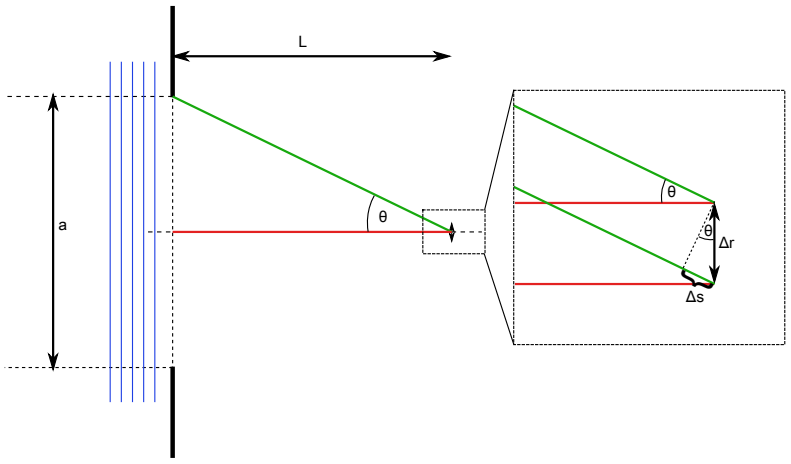

Figure 2.2: Illustration of the path difference Δs. Two waves interfering at a double slit like diffraction object after propagating through a slit.

The transversal coherence length is the maximum separation of the double slit still allowing for interference. The interference takes place up to a maximum phase difference $\Delta\phi = \pi$.

$$\Delta l_\perp \approx \frac{L}{a}\lambda \approx \frac{\lambda}{2 \cdot \Delta\theta} \tag{2.9}$$

For a projectile beam, the angular slit width $\Delta\theta$ can be expressed in terms of momenta $\Delta\theta = \Delta p_\perp / p_\parallel$. By considering the de Broglie wavelength $p = h/\lambda$, eq. (2.9) results in

$$\Delta l_\perp \approx \frac{h}{2 \cdot \Delta p_\perp} \tag{2.10}$$

It should be noted, that in the derivation shown here the projectile wave is assumed to have a coherence length of $\Delta l_\perp = 0$ at the position of the entrance slit. However, as will be detailed in section 2.1.3.2 eq. (2.10) is generally applicable to calculate $\Delta l_\perp$ (while eq. (2.8) is not).

Now it is possible to estimate the coherence lengths of the projectiles used in this work. For the longitudinal coherence length the longitudinal momentum spread in the TSR has to be known, which is about $\Delta p_\parallel / p_\parallel \approx 10^{-4}$ (Grieser et al., 2012). With a typical emittance of $\epsilon = 0.05\,\text{mm mrad}$ and a beam size of about $r = 1\,\text{mm}$ the maximum transverse momentum can be calculated with $p_\perp = p_\parallel \cdot \epsilon / r$ (see section 3.3). The resulting coherence lengths are shown in table 2.1. The transverse coherence lengths are twice as large as the longitudinal ones. However, all values are smaller than the size of the lithium target atom, which is about 3 a.u.. Thus, despite the elaborate cooling techniques employed in the TSR, the target is never illuminated completely coherently.

However, for atomic collisions the coherence length does not need to be compared to the size of the whole atom, but rather to the impact parameters of the observed processes (Sarkadi, 2010). Thus, interference effects can be switched on and off by selecting different impact parameters (Schneider et al., 2013).

2.1.3.2 Coherence properties behind a slit

In this chapter it is discussed in more detail how a slit influences the coherence properties of an incoming beam. Exemplarily, 75 keV protons were chosen as projectiles.

projectile	l_l [a.u.]	l_x [a.u.]
24 MeV O^{8+}	0.54	0.28
16 MeV O^{7+}	0.68	0.34
16 MeV Li^{2+}	1.02	0.51

Table 2.1: Longitudinal $l_\parallel$ and transverse $l_\perp$ coherence lengths in the storage ring TSR. The listed projectiles were used in this work.

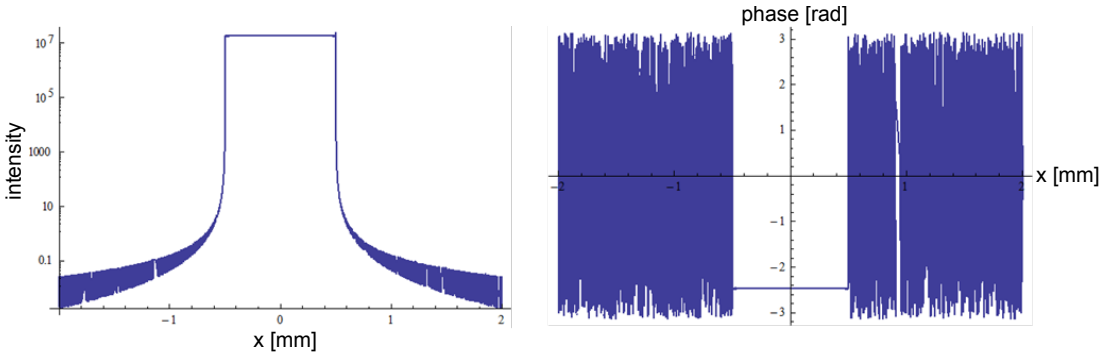

Figure 2.3: Intensity (a) and phase (b, at an arbitrary time) of a plane wave after propagating through a slit.

The intensities and phases are calculated at a distance of 500 mm from the slit with Kirchhoff's diffraction formula (e.g. Griffith, 2012).

Coherent projectile wave

In the first step a plane wave (which has an infinite coherence length) propagates through a slit with a width of 1 mm. The intensity and phase are shown in fig. 2.3. No intensity or phase fluctuations can be seen at an accuracy of better than 0.01%, which implicates that the slit did not change the coherence properties.

When the plane wave is diffracted by two separated atoms with a distance r (which is equivalent to a double slit), a point at a screen can be reached on two different paths from the same point at the slit. Such a setup is shown in fig. 2.4, where the two paths are drawn as a green and a dashed red line. The difference in path lengths should

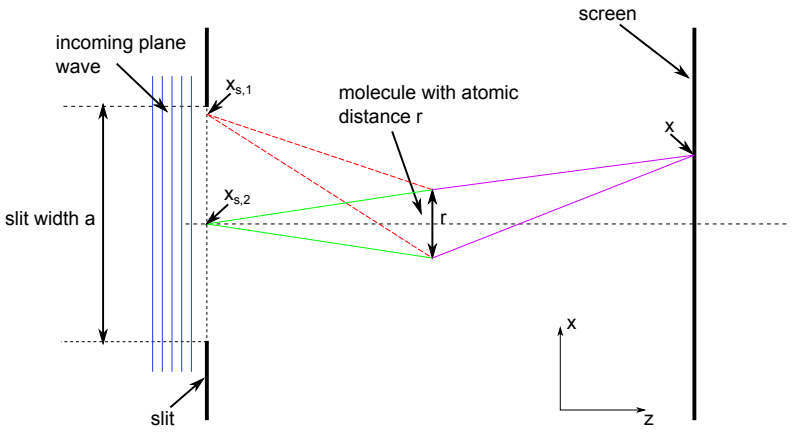

Figure 2.4: Different paths with the same start- and end-point. A plane wave can be diffracted at two atoms separated by Δr and reach the same point at the screen by two different paths (red and green).

lead to a phase difference at the screen. However, this phase difference depends on the source point at the slit x_s. For a coherence length of $\Delta l_\perp = 0$ at the slit, the waves emerging from different source positions do not interfere and the intensity is calculated being $\int dx_s |\Psi(x, x_s)|^2$. However, this is not the correct approach, if the relative phases of any pair of two x_s is fixed. Here the absolute square has to be taken after integration:

$$I \propto \left| \int dx_s \Psi(x, x_s) \right|^2 \tag{2.11}$$

which results again in an interference pattern on the screen.

In conclusion, the slit does not decrease the coherence length of a beam. However, how is an incoherent beam influenced by a slit?

Incoherent projectile wave

Since the plane wave is the standard theoretical model for the projectile ion, the question of the justification of this assumption arises. The wave fronts have to be parallel for a wave to be coherent. In the setup discussed above, the wavelength of the projectile is about 0.002 a.u. while the slit width is 2×10^7 a.u.. According to eq. (2.10), for a projectile wave of this kind the transverse momentum spread has to be smaller than 3×10^{-11} a.u. in order to illuminate the slit coherently. Such a condition is, however, unrealistic. Hence it is important to know how an incoherent wave is influenced by a slit.

A wave can be seen as sum of spatially separated wave packets (almost) not overlapping with each other. A slit is the source for many of these waves, each undergoing Fraunhofer diffraction. For parallel waves ($l_\perp = \infty$) the divergence resulting from the diffraction is negligible, see fig. 2.3, hence each point x at the screen is illuminated by only one wave. In this case the slit is obsolete (in contrary to eq. (2.8)). Waves with $l_\perp < a$ have a larger momentum spread at the slit, thus, the beams of the wave packets are divergent, i.e. a point at the screen is illuminated by more than one initial wave packet. This leads to a washing out of the interference structures.

However, in ion-atom collisions the target is much smaller than the slit, i.e. it is possible that the beam of only one wave packet illuminates the target. So even a wave packet with $l_\perp < a$ can diffract coherently at a sufficiently small target. In fig. 2.5 an incoherent beam is cut by a slit, illustrated in phase space. At the target the divergence can be seen, which results in a larger coherence length than at the slit for small targets. Hence, eq. (2.10) is only a lower limit for the coherence length:

$$\Delta l_\perp > \frac{h}{\Delta p_\perp} \tag{2.12}$$

Hereby a six-dimensional phase space can be defined, in which the individual waves are completely coherent:

$$\Delta l_x \Delta l_y \Delta l_z \Delta p_x \Delta p_y \Delta p_z > h^3 \tag{2.13}$$

Interference structures in atomic collisions due to the the scattering on two nuclei of H_2 were already predicted in (Tuan and Gerjuoy, 1960). In recent years, traces for

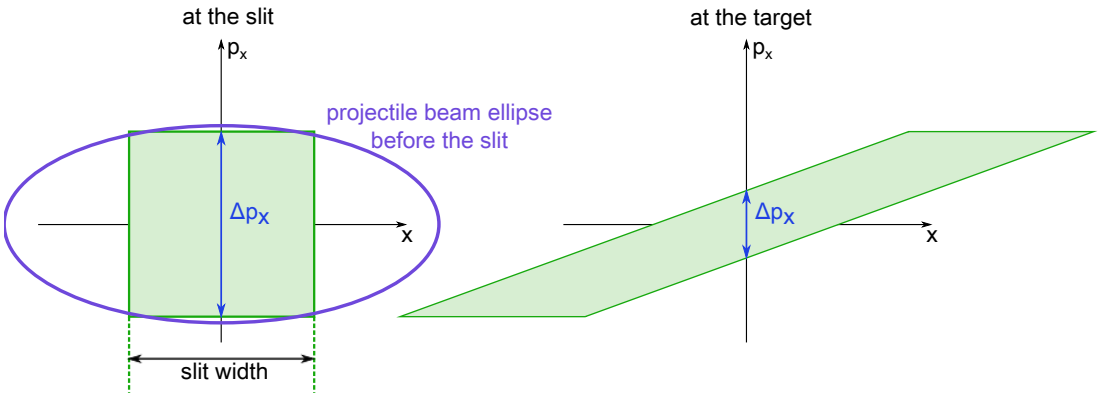

Figure 2.5: Influence of a slit to an incoherent beam. The phase space is shown at the slit and at the target. The coherence length increases, especially for small targets.

interference were found in the electron emission (Stolterfoht et al., 2001; Misra et al., 2004; Alexander et al., 2008) and even in the projectile scattering angle (Schmidt et al., 2008).

The role of the projectile coherence was first considered in (Egodapitiya et al., 2011) and (Sharma et al., 2012). In these experiments a proton beam was collided with H_2, investigating single ionization and electron capture, respectively. The transverse coherence length of the projectile beam was varied by a slit with variable distance to the target. A difference in the DDCS ($d\sigma/(d(\Delta E)d\Omega_p)$ with the projectile energy loss ΔE and scattering angle Ω_p) was observed for slit distances corresponding to coherence lengths smaller (no interference) and larger (interference) than the molecular target. However, this coherence lengths were determined with eq. (2.8), which in fact only delivers a lower limit for the coherence length (as explained above). In the following, these publications were discussed controversially, e.g. (Feagin and Hargreaves, 2013), where observed differences are attributed to off-axis contributions of the incident beam (i.e. projectiles with an initial transverse momentum), which are washing out interference structures equivalent to resolution effects to the projectile initial momentum spread. However, this interpretation does also not fully explain the experimental observation.

A definite conclusion of the influence of projectile coherence would require experimental and theoretical input: first, experimental data where the projectile coherence length is varied systematically and where cross sections are studied that are insensitive on the projectile momentum resolution and second, theoretical models which include the projectile coherence length as a parameter. Both are presently not available.

2.2 Kinematics

In this chapter momentum and energy conservation in atomic collisions will be discussed. The consideration of conservation laws is very important, as not all momenta and energies of the reaction are directly measured but subsequently derived. For N involved particles momentum space has 3N dimensions. Momentum and energy conservation reduces the degrees of freedom by four, therefore only 3N-4 independent parameters have to be measured.

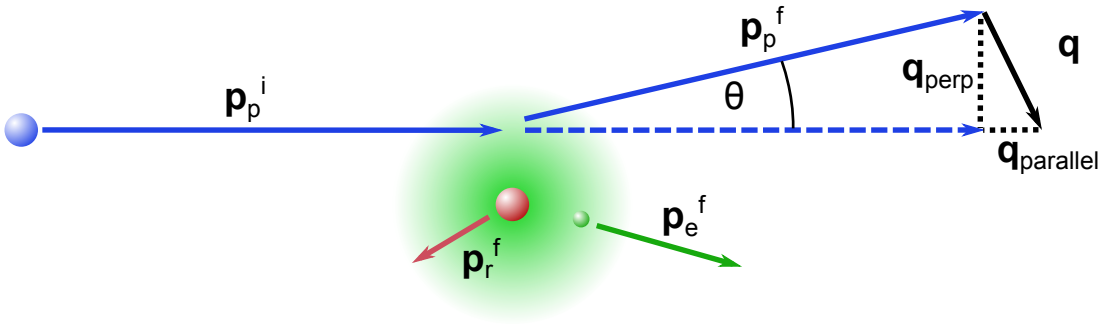

Figure 2.6: Kinematics of an ionization process. The superscripts i and f refer to initial and final state, the subscripts p, r and e to projectile, recoil ion and electron, respectively. **p** denotes the momentum and **q** the momentum transfer.

The momentum vectors in an ionization process are depicted in fig. 2.6. The initial projectile momentum $\mathbf{p}_p^i$ defines the z-axis. The projectile is scattered by the target core and its electron and, thereby, transfers the momentum **q** to the target system:

$$\mathbf{q} = \mathbf{p}_p^i - \mathbf{p}_p^f \tag{2.14}$$

These reactions are cylindrically symmetric with respect to the initial projectile direction, therefore the momenta are often expressed in cylindrical coordinates.

The momenta in the target frame ($\mathbf{p}_r^i = 0$) can be expressed by the following equation:

$$\mathbf{p}_p^i = \mathbf{p}_p^f + \mathbf{p}_r^f + \sum_{j=1}^{n_I} \mathbf{p}_{ej}^f + n_C \mathbf{v}_p \tag{2.15}$$

where the last term represents n_C electrons that are captured by the projectile and therefore have the velocity v_p (this is only valid for $\frac{|v_p^f - v_p^i|}{v_p} \ll 1$). Energy conservation in the target frame ($E_r^i = 0$) gives:

$$E_p^i = E_p^f + E_r^f + Q + \sum E_e j^f{}_{j=1}^{n_I} \tag{2.16}$$

with the difference of the binding energies in the initial and final state

$$Q = E_{bind}^f - E_{bind}^i \tag{2.17}$$

Fast collisions

In the collision systems investigated in this thesis the velocities are high, i.e. $\mathbf{q} \ll \mathbf{p}_p$. On the other hand, the projectile velocities did not exceed 10 a.u., hence relativistic effects can be neglected.

In fast collisions the momenta of the recoil ions and the electrons are of similar magnitude. Hence the mass difference between electrons and ions gives rise in a much smaller recoil ion energy compared to electron and projectile energies. Neglecting the recoil ion energy, the energy conservations can be written as

$$\frac{p_p^{i2} - p_p^{f2}}{2M_p} = Q + \sum_{j=1}^{n_I} E_{ej}^f + \frac{v_p^2}{2} n_C \tag{2.18}$$

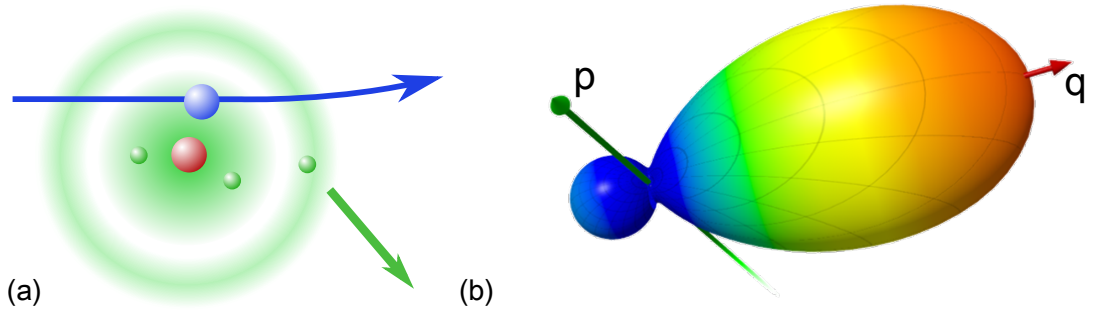

Figure 2.7: Single ionization of lithium (a) and typical electron emission angle distribution in single ionization (b). The latter shows a calculation of a 100 MeV/amu C^{6+}+He collision. **p** depicts the momentum of the projectile, **q** the momentum transfer (Schulz et al., 2003).

where M_p is the initial projectile mass and the last term accounts for the mass change in the projectile at electron capture. Combined with eq. (2.15) this results in a longitudinal recoil momentum of

$$p^f_{r\parallel} = \frac{Q}{v_p} - \frac{v_p}{2} n_C + \sum_{j=1}^{n_I} \left(\frac{E^f_{ej}}{v_p} - p^f_{ej\parallel} \right) \tag{2.19}$$

In fast collisions the scattering angle θ of the projectile is quite small. This allows for the approximation $\mathbf{p}^f_{p\perp} \approx \mathbf{p}^f_{p\parallel}\theta_p \approx M_p v_p \theta_p$ which results in a transverse momentum of

$$\mathbf{p}^f_{r\perp} \approx -M_p v_p \theta_p - \sum_{j=1}^{n_I} \mathbf{p}^f_{ej\perp} \tag{2.20}$$

In conclusion, the longitudinal momentum transfer eq. (2.19) contains only kinematic information and it allows deriving the difference in binding energies Q. The transverse momentum transfer in contrast delivers information about the dynamics of the collision.

2.2.1 Single Ionization

In single ionization (SI, see fig. 2.7 (a)) one target electron is ionized by the projectile:

$$X^{Z_p+} + Li \rightarrow X^{Z_p+} + Li^+ + e^- \tag{2.21}$$

The momentum transfer **q** is given by

$$\mathbf{q} = \mathbf{p}^f_r + \mathbf{p}^f_e \tag{2.22}$$

The FDCS (see section 4.3) of such a process is shown in fig. 2.7 (b). Here the CDW-EIS calculation of a 100 MeV/amu C^{6+} projectile on a helium target is shown for $E_e = 6.5$ eV and $q = 0.75$ a.u.. The typical double lobe structure consists of a pronounced peak in direction of the momentum transfer **q**, usually called 'binary' peak, and a smaller peak in the opposite direction, referred to as 'recoil' peak.

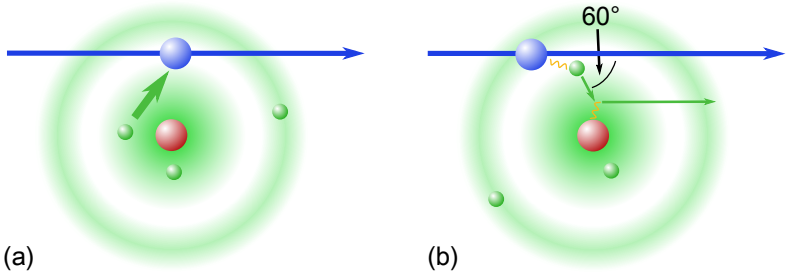

Figure 2.8: Single capture of lithium. (a) illustrates the process while (b) shows the Thomas capture mechanism. Details see text.

2.2.2 Single Capture

Single capture (SC) is a rather simple collision process. One electron from the target is transferred to the projectile, which results in a charge changed projectile and a lithium ion in the final state (see also fig. 2.8):

$$X^{Z_p+} + Li \rightarrow X^{(Z_p-1)+} + Li^{+} \tag{2.23}$$

The momentum transfer $\mathbf{q}$ is identical to the recoil momentum

$$\mathbf{q} = \mathbf{p}_r^f \tag{2.24}$$

As there is no free electron in the final state, SC is essentially an inelastic two particle collision. Equation (2.19) results in

$$p_{r\|}^f = \frac{Q}{v_p} + \frac{v_p}{2} \tag{2.25}$$

where the longitudinal recoil ion momentum features a discrete distribution because of its Q-dependence. A schematic drawing of the process is shown in fig. 2.8 (a). In electron capture, mainly two models are distinguished: the 'kinematic' (Oppenheimer, 1928; Brinkmann and Kramers, 1930) and the Thomas capture (Thomas, 1927). The former describes the capture due to matching velocities of the bound electron and the projectile, i.e. the Compton profiles of the projectile and target overlap. Thomas capture is a two step process: first the projectile scatters the electron, which is subsequently scattered by the target core and emitted in projectile direction with a velocity similar to v_p, hence allowing a bound state with the projectile (see fig. 2.8 (b)). This process is dominant at high projectile velocities, as the dependence of the total cross section is $\sigma \propto 1/v_p^{-11}$ (Briggs and Taulbjerg, 1979), while for kinematic capture $\sigma \propto 1/v_p^{-12}$. In (Fischer et al., 2006) the two processes were measured in proton on helium collisions.

2.2.3 Transfer Ionization

The Transfer ionization process (TI) is a combination of single ionization and single capture. One electron is captured by the projectile, while another one is ionized (see fig. 2.9):

$$X^{Z_p+} + Li \rightarrow X^{(Z_p-1)+} + Li^{2+} + e^{-} \tag{2.26}$$

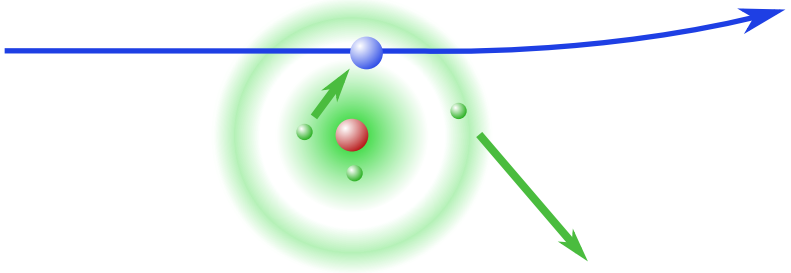

Figure 2.9: Schematic drawing of transfer ionization (TI) of lithium.

In TI, the definition of the momentum transfer $\mathbf{q}$ has to be changed in order to account for the change of energy of the captured electron. This can easily be done by adding the projectile velocity (which is also the velocity of the captured electron):

$$\mathbf{q} = \mathbf{p}_r^f + \mathbf{p}_e^f + \mathbf{v}_p \tag{2.27}$$

As there is only one electron in the continuum, the final state of this process is similar to SI. However, small impact parameters are required to enable the capture process, which results in a high q and large scattering angles.

In general two different TI processes can be distinguished: independent TI and correlated TI. The first consists of two independent interactions of the projectile with the electrons, while in the latter the projectile interacts only with one electron and in a second step an electron-electron interactions results in the loss of the second electron.

A schematic drawing of the independent TI process is shown in fig. 2.10 (a). The two interactions of the projectile require more time than only one interaction, so this process is more likely for slow projectile velocities, when the interaction time is long.

In correlated TI processes the emission of an electron enables the capture process. The projectile interacts only once with the target, which makes this process more likely at higher projectile energies than the independent TI. An illustration of the process is shown in fig. 2.10 (b). The collision properties and the type of electron-electron interactions can lead to different final states of the emitted electron. The most likely processes are the Thomas TI (Thomas, 1927; Briggs and Taulbjerg, 1979) where the electron is emitted perpendicular to the projectile direction, the eeTI (Voitkiv et al., 2008) where the electron is emitted backwards and shake-off or shake-over TI with an isotropic electron emission.

2.3 Theoretical methods

In this chapter a brief overview over several different theoretical concepts will be given, i.e. the perturbative, the distorted wave and the ab-initio approach. Most of the following descriptions in this chapter can be found in more detail in (McDowell and Coleman, 1970) or (Taylor, 2006).

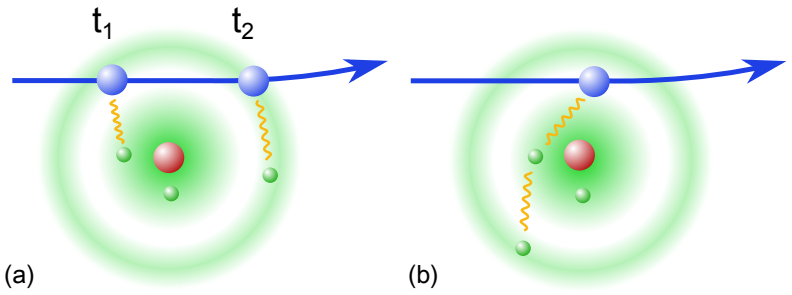

Figure 2.10: Schematic drawing of independent (a) and correlated (b) TI of lithium.

2.3.1 The perturbative approach

For a collision process the Hamiltonian can be written as the sum of the unperturbed Hamiltonian H_0 and the interaction between the projectile and the target V:

$$H = H_0 + V \tag{2.28}$$

The solution of such a system is given by the time-independent Schrödinger equation:

$$(H - E)\,|\Psi\rangle = 0 \tag{2.29}$$

$$(H_0 - E_0)\,|\Phi\rangle = 0 \tag{2.30}$$

where $|\Psi\rangle$ and $|\Phi\rangle$ are the electronic wave functions of the full Hamiltonian and for the non-interacting system, respectively. These states can be seen as the solution of the Hamiltonian at different times: $\lim_{t\to+\infty} |\Psi(t)\rangle = |\Phi_f\rangle$ and $\lim_{t\to-\infty} |\Psi(t)\rangle = |\Phi_i\rangle$, because $V \to 0$ for $t \to \pm\infty$, where $|\Phi_i\rangle$ and $|\Phi_f\rangle$ denote the initial and final state of the unperturbed system. $|\Phi_i\rangle$ evolves into $|\Psi_i\rangle$, when the perturbation potential V cannot be neglected anymore. The solutions of the time-dependent Schrödinger equation are

$$|\Psi\rangle = e^{-iEt}\,|\Psi\rangle \qquad \text{and} \qquad |\Phi\rangle = e^{-iEt}\,|\Phi\rangle \tag{2.31}$$

The transition amplitude corresponds to the ratio of a particular final state to all possible final states, which is given by the projection of $\lim_{t\to+\infty} |\Psi(t)\rangle$ on the unperturbed final state $|\Phi^f\rangle$:

$$A^{fi} = \lim_{t\to+\infty} \langle\Phi_f|\Psi_i(t)\rangle \tag{2.32}$$

The cross section is given by the square of this amplitude: $\sigma \propto |A^{fi}|^2$.

Equation (2.32) contains oscillating integrals (caused by the phases in eq. (2.31)), which have to be damped, resulting in (McDowell and Coleman, 1970; Fischer, 2003):

$$A^{fi} = -2\pi i T^{fi} \delta(E_f - E_i) \tag{2.33}$$

with the T-matrix

$$T^{fi} = \langle\Phi_f|V|\Psi_i^+\rangle \tag{2.34}$$

The '+' denotes that the state satisfies outgoing-wave boundary conditions. These equations are the exact solution to the scattering problem. However, it is non-trivial

to find the eigenstate $|\Psi_i^+\rangle$ of the complete Hamiltonian. An iterative solution can be obtained with the *Lippmann-Schwinger equation* (McDowell and Coleman, 1970):

$$|\Psi_i^\pm\rangle = |\Phi\rangle + G_0^\pm V\,|\Psi_i^\pm\rangle \tag{2.35}$$

with the Green's function operator

$$G_0^\pm = \lim_{\epsilon\to 0}\frac{1}{E_0 - H_0 \pm i\epsilon} \tag{2.36}$$

With the *Lippmann-Schwinger equation* eq. (2.35), $|\Psi_i^\pm\rangle$ can be regarded as the sum of the 'incident' plane wave $|\Phi\rangle$ and the 'distortion' $G_0^\pm V\,|\Psi_i^\pm\rangle$ caused by the potential. The iteration of the state $|\Psi_i^+\rangle$

$$|\Psi_i^+\rangle = |\Phi_i\rangle + G_0^+ V\,|\Phi_i\rangle + G_0^+ V G_0^+ V\,|\Phi_i\rangle + G_0^+ V G_0^+ V G_0^+ V\,|\Psi_i^+\rangle \tag{2.37}$$

can be used to determine the T-matrix:

$$T^{fi} = \langle\Phi_f|V|\Phi_i\rangle + \langle\Phi_f|V G_0^+ V|\Phi_i\rangle + \langle\Phi_f|V G_0^+ V G_0^+ V|\Phi_i\rangle + ... \tag{2.38}$$

Here T^{fi} is expanded in a series of powers of the perturbations potential V, i.e. for low perturbations higher order terms can be neglected.

2.3.1.1 First Born approximation

In the first Born approximation, only the first term of the Born series (eq. (2.38)) is considered, while the second includes the first two terms ($T_{SB}^{fi} = \langle\Phi_f|V|\Phi_i\rangle + \langle\Phi_f|V G_0^+ V|\Phi_i\rangle$). The Born series only converges in the case of weak potentials or high energies. This chapter will only address the first Born approximation, further details can be found in (Taylor, 2006; McDowell and Coleman, 1970).

For a projectile that can be expressed by plane waves, the eigenstates of H_0 can be written as $|\Phi\rangle = e^{i\mathbf{p}_p\mathbf{r}_p}|\varphi\rangle$, where $\mathbf{p}_p$ and $\mathbf{r}_p$ are the projectile momentum and its distance to the target nucleus, respectively, while $|\varphi\rangle$ is the electron wave function.

$$T_{(FB)}^{fi} = \langle\phi_f|V|\phi_i\rangle = \langle\varphi_f|e^{i\mathbf{q}_p\mathbf{r}_p}\cdot V|\varphi_i\rangle \tag{2.39}$$

Here $\mathbf{q} = \mathbf{p}_f^p - \mathbf{p}_i^p$ is the momentum transfer (introduced in section 2.2).

In a collision process the interaction is given by the Coulomb potential for N target electrons:

$$V = \frac{Z_p Z_t}{r_p} - \sum_{j=1}^{N}\frac{Z_p}{|\mathbf{r}_p - \mathbf{r}_{e_j}|} \tag{2.40}$$

where Z_p and Z_t are the charge states of the projectile and target and $\mathbf{r_{e_j}}$ is the distance of the electron to the target. After inserting this potential into eq. (2.39), the transition matrix is given by (Bethe's integral, see e.g. (McGuire, 1997))

$$T_{(FB)}^{fi} \propto \left\langle \varphi_f \left| \sum_{j=1}^{N} e^{i\mathbf{q}\mathbf{r}_{e_j}} \right| \varphi_i \right\rangle \tag{2.41}$$

Because of the orthogonality of the eigenstates $\varphi_{f,i}$, the first term of eq. (2.40) does not contribute. For small momentum transfers, the exponential function can be expanded, resulting in

$$T^{fi}_{(FB)} \propto \left\langle \varphi_f \left| \sum_{j=1}^{N} i\mathbf{q}\mathbf{r}_{e_j} \right| \varphi_i \right\rangle \tag{2.42}$$

when higher order terms are neglected. Again, the first term vanishes due to orthogonality of the states. Equation (2.42) is the dipole approximation, which is equivalent to the theoretical treatment of photo-ionization, where the corresponding operator is $\boldsymbol{\epsilon} \cdot \mathbf{r}$, with the linear polarization direction $\boldsymbol{\epsilon}$.

In the first Born approximation any interactions between the projectile and the target core as well as multiple projectile-electron interactions are neglected. In the next chapters theoretical models will be introduced that include some higher order effects.

2.3.2 Distorted wave approximation

The first Born approximation is only valid for weak perturbations. However, this is often not the case, therefore the distorted wave approximation can be employed (further details in (Taylor, 2006)).

Here the potential is split into two parts

$$V = V_I + V_{II} \tag{2.43}$$

where V_I is exactly known (or can be approximated well) and the effects of V_{II} are small. In electron-nuclei scattering V_I could describe the exact Coulomb potential, while V_{II} would represent the deviation from pure Coulomb inside the nucleus.

The T matrix (eq. (2.34)) can be written for the full potential V and for the known potential V_I:

$$T^{fi} = \langle \Phi_f | V | \Psi_i^+ \rangle \qquad \text{and} \qquad T_I^{fi} = \langle \Phi_{f,I} | V_I | \Phi_{f,I} \rangle \tag{2.44}$$

i.e. $|\Phi_I^f\rangle$ and $|\Phi_I^f\rangle$ are the 'distorted waves' corresponding to scattering by only V_I, and they are known or at least well approximated quantities (as well as T_I^{fi}). This results in the following T matrix

$$T^{fi}_{DW} = T_I^{fi} + \langle \psi^-_{f,I} | V_{II} | \psi_i^+ \rangle \tag{2.45}$$

where the first term is known and only the second term depends on V_{II}. In the *distorted wave Born approximation* (DWBA) all terms that are of the order V_{II}^2 and higher are dropped. While the first term is independent of V_{II}, the second term contains V_{II} explicitly, so only the effects of V_{II} on $|\psi_+\rangle$ have to be removed, i.e. $|\psi_+\rangle \approx |\psi_{+,I}\rangle$. This gives

$$T^{fi}_{DWBA} \approx T_I^{fi} + \langle \psi^-_{f,I} | V_{II} | \psi^+_{i,I} \rangle \tag{2.46}$$

The differences to the first Born approximation $T^{fi}_{(FB)} = \langle \phi_f | V | \phi_i \rangle$ are that part of the potential (V_I) is accounted for to all orders, while the second term is a matrix element of the small potential V_{II} between distorted waves – and not between plane

waves as in the first Born approximation. These distorted waves are appropriate to V_I - hence this potential scatters the projectile (first term) and distorts the waves for the second potential (second term).

The *continuum distorted wave* (CDW) approximation expands the first-order DWBA by including a second-order term that accounts for intermediate states of two-body sub-systems (Belkic, 1978).

Another extension was introduced as *continuum distorted wave - eikonal initial state* model (CDW-EIS) (Crothers and McCann, 1983; Fainstein et al., 1991). Here the initial bound state is distorted by a projectile eikonal phase, while the final state is the same as in CDW.

2.3.3 Ab-initio methods

Ab-initio methods are numerical calculations without approximations, i.e. these are complete calculations solving the Schrödinger equation numerically. The main obstacle are the infinite non-discrete continuum states that have to be considered. In the *convergent close coupling* (CCC) method these continuum states are replaced by a set of discrete 'pseudostates'. Especially for higher continuum states this is a poor approximation, however, convergence to the true states can be reached by increasing the number of pseudostates (Bray and Stelbovics, 1992; Bray and Stelbovics, 1993; Bray and Fursa, 1996).

2.3.4 Few-electron transitions

The **independent electron approximation** effectively reduces the N electron problem to solving the one electron problem N times. In a scattering process the Hamiltonian including electron-electron interactions for N electrons is

$$\begin{aligned} H = &-\frac{\nabla^2}{2M_r} + \frac{Z_p Z_t}{r_p} - \sum_{j=1}^{N} \frac{Z_p}{|\mathbf{r}_p - \mathbf{r}_{e_j}|} \\ &+ \sum_{j=1}^{N} \left[-\frac{\nabla_j^2}{2} - \frac{Z_t}{r_{e_j}} + \sum_{k,(k>j)} \frac{1}{|\mathbf{r}_{e_k} - \mathbf{r}_{e_j}|} \right] \end{aligned} \tag{2.47}$$

with reduced mass M_r. The electron correlation can be approximated with an average (or mean field) potential:

$$\sum_{k,(k>j)} \frac{1}{|\mathbf{r}_{e_k} - \mathbf{r}_{e_j}|} \approx v_j(r_j) \tag{2.48}$$

Now the Hamiltonian is a sum of single electron terms, hence the full electron wave function Ψ can be written as a product of the single electron wave functions:

$$|\Psi\rangle = \prod_j |\Psi_j\rangle \tag{2.49}$$

Thus, in the **independent electron approximation** also the transition probability $\sigma = |A^{fi}|^2$ is a product of the corresponding independent single electron probabilities, hereby simplifying the many body problem significantly. Further detail can be found in (McGuire, 1997).

3. The experimental setup

The experimental setup used in this work combines three state-of-the-art technologies: a reaction microscope (ReMi), a magneto optical trap (MOT) and an ion storage ring. This chapter aims to give a short overview of these three techniques, as the setup was already described in (Hubele, 2013) and (Fischer et al., 2012). Especially the application of a MOT as a target instead of a supersonic gas jet traditionally used in ReMis has a lot of implications, e.g. it significantly improves the resolution and permits the use of non rare gas atomic targets. The use of an ion storage ring provides additional advantages with respect to the obtainable resolution due to its excellent beam quality.

3.1 Reaction microscopes

Reaction microscopes are widely used tools in atomic physics as the full momentum vectors of all particles in collision processes can be obtained in coincidence (Ullrich et al., 2003). The working principle is illustrated in fig. 3.1. Atoms in a target gas are ionized by a projectile beam. The resulting ion and the electron(s) are accelerated towards the position- and time-sensitive detectors by an electric field and pass a drift region after wards. A superimposed magnetic field forces the particles on a cyclotron trajectory and hereby increases the transverse acceptance for high energetic electrons significantly. In the following the z-axis is chosen to be the spectrometer axis, while the detectors are parallel to the x,y-plane.

3.1.1 The spectrometer design

The spectrometer design has to fulfill several requirements: the MOT coils have to be kept as small as possible (see section 3.2.4.1), the aperture has to be big enough to allow an uncooled ion beam to pass (about 40 mm) and a longitudinal extraction direction is needed for a large electron acceptance. This results in a conically shaped spectrometer, which is inclined by 8° in respect to the storage ring (fig. 3.2).

The spectrometer itself consists of 84 ring-electrodes that produce the electric field for the extraction of the target fragments. It is divided into three parts (see fig. 3.2):

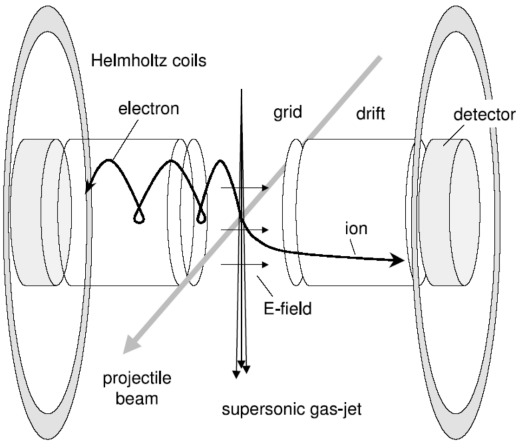

Figure 3.1: Working principle of a reaction microscope. Taken from (Ullrich and Shevelko, 2003).

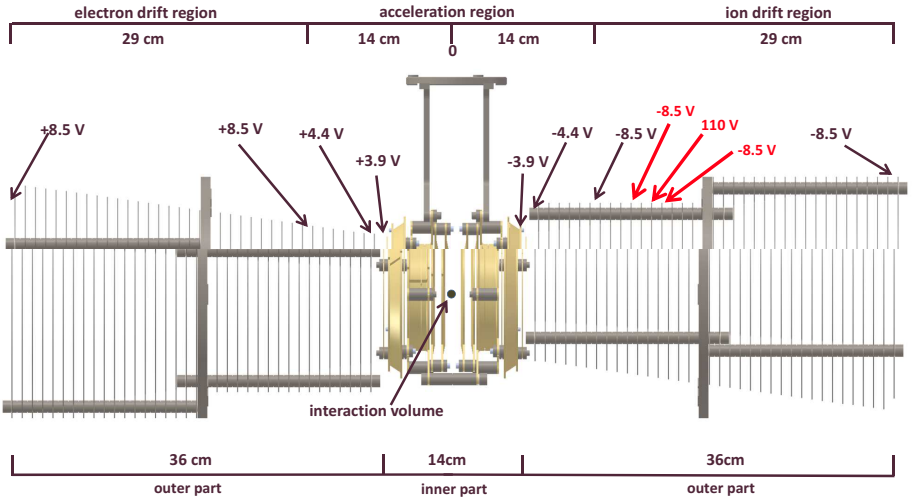

Figure 3.2: Design of the spectrometer. Also shown are the electric connections and a typical voltage configuration of about 20 V/m. The voltages in red are only applied in switching mode section 3.1.1

the outer parts consist of 35 electrodes each, which are connected in a chain by 100 kΩ resistors and the inner part 14 electrodes connected by 17 kΩ resistors representing a voltage divider. Several electrodes can be electrically connected from the outside of the vacuum chamber in order to apply the voltages required for extraction.

The magnetic field is generated by Helmholtz coils. As this field has to be homogeneous throughout the whole spectrometer, the coils have to have a rather large diameter, in the present case 85 cm, and are located outside the chambers. A typical value for the resulting magnetic field in the spectrometer is 10 Gs.

Time and position focusing

With time and position focusing the finite extension of the reaction volume (the overlap of the projectile beam and the gas jet (or MOT) target) can be compensated. For a homogeneous electric extraction field the time-of-flight (TOF) and the position on the detector of a charged particle would also depend on the location of the collision.

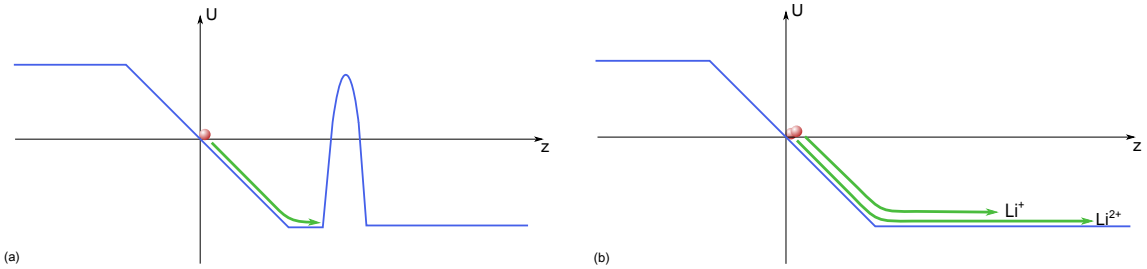

Figure 3.3: Potential in the ReMi with (a) and without (b) the switching voltage.

In z- (i.e. TOF-) direction this can be avoided in first order by using the specific ratio of the acceleration and drift lengths $l_d = 2 \cdot l_a$, which is called time focusing (Wiley and McLaren, 1955).

In transverse direction position focusing can be achieved by applying electrical lenses close to the reaction volume. In the presented measurements position focusing was not used, as it distorts the trajectories of the electrons.

Switching the spectrometer

Switching the spectrometer is a powerful technique to dispose of specific types of background. It can be employed in collision processes with small cross sections, that allow to measure an almost instantaneous time signal of the reaction (e.g. a charge-changed projectile or a photon) at a low rate (below 10 kHz). Here a higher charged recoil ion can be separated from Li^+ and heavy residual gas ions.

In this setup it was used in Transfer Ionization measurements (TI, see section 2.2.3). Here the collision results in a charge changed projectile, a Li^{2+} ion and an electron. The detection of the charge changed projectile serves as time information in contrary to measurements of e.g. Single Ionization (SI, see section 2.2.1), where a bunched projectile beam has to be employed to get a time reference. However, in TI a continuous projectile beam is used as its quality is better than a bunched beam. The cross section of TI (being a two-step process) is several orders of magnitude smaller than the cross section of SI (being a one-step process), which results in a constant background of Li^+-ions originating from SI.

In the presented measurements of the TI process, a switching voltage is applied at one electrode as shown in fig. 3.2 (red arrrows) on the ion side of the spectrometer. This voltage of 110 V provides an effective barrier of about 9 V in the middle of the spectrometer.

The working principle is shown in fig. 3.3: Without switching all ions reach the detector after passing through the acceleration and drift parts of the spectrometer. While the switching voltage is applied, only the few residual gas ions that are ionized in the drift region after the potential barrier can reach the detector. If now a charge changed projectile is measured, a Li^{2+}-ion starts at $z = 0$. After about 5 µs the switching voltage is removed and all particles can reach the detector again. However, now the "measured TOF" is mass and charge selective, e.g. higher charged and less massive ions reach the detector earlier. Therefore the Li^{2+}-ion reaches the detector before the Li^+-ion. It has to be noted, that the "measured TOF" is not the real TOF of the ions anymore, as it depends on the switching time. The data acquisition

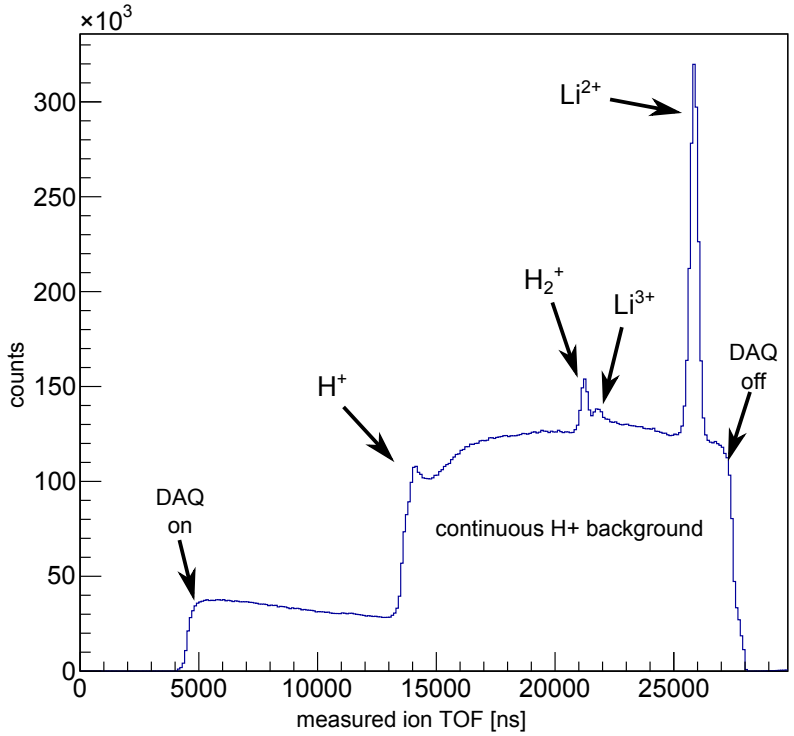

Figure 3.4: Measured ion TOF spectrum in switching mode. The shown TOF is influenced by the switching, wherefore it is not the actual TOF of the ions. Li^+ would be expected at a TOF of about 37 µs.

system is also gated with the projectile and only acquires data up to a certain ion-TOF (see fig. 3.4).

3.1.2 Detectors

The detectors in a ReMi have to be position- and time-sensitive in order to reconstruct the 3D momenta. Two detectors are used in order to both detect the positively charged ions and the negatively charged electrons, which are accelerated in opposite directions by the electric field. In this setup the active diameter of these detectors is 80 mm and they are movable as the projectile beam in the storage ring can change its size and position during the injection and storing cycle. The time information is measured by a micro channel plate (MCP), while a delay-line anode determines the position. These two components are described briefly in the following, an extensive description can be found in (Sell, 2010) and (*MCP Delay Line Detector Manual*).

The MCP consists of an array of channels with a diameter of 25 µm each in a glass plate with low-resistive layers on the front and back side and works as a secondary electron multiplier. If an incident particle hits the wall of such a channel, it starts an avalanche of secondary electrons which is then accelerated by a potential difference of about 1 kV between the front and the back of the MCP (see fig. 3.5 (a)). The electron cloud leaves the MCP towards the delay-line anode. In order to prevent particles from passing a channel without hitting its walls, MCPs are usually stacked, i.e. two (the so-called ”chevron” configuration) or three (”Z-stack”) channel plates of opposite inclination are put on top of each other.

The delay-line anode consists essentially of four wires wrapped around an insulator, two of which are perpendicular to the others. The electron cloud leaving the MCP

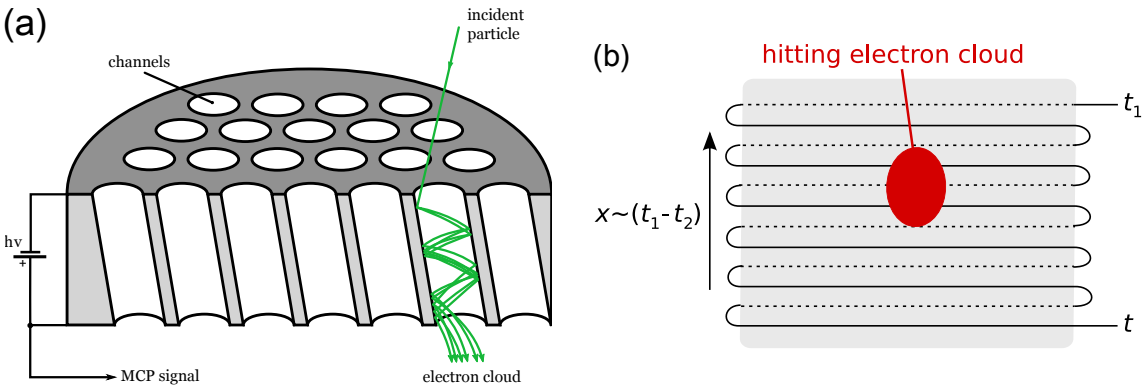

Figure 3.5: Working principle of a micro channel plate (a) and a delay line anode (b) For details see text. Taken from (Pflüger, 2012) and (Senftleben, 2009).

hits the wires and the resulting charge deposit is measured on both ends of each wire. The time difference of these signals is proportional to the position of the cloud perpendicular to the wire direction (see fig. 3.5 (b)). The second wire of each pair is a reference wire, which is connected to a smaller potential than the main wire. While noise appears equally in both wires, the electron detection is more efficient in the main wire with the higher potential. The difference of the signals on the wires delivers a noise-reduced signal.

3.1.3 Data acquisition

The signals coming from the detectors are processed by a data acquisition system. After being amplified by a fast amp, a CFD (Constant Fraction Discriminator) converts the analog signal into a NIM pulse. These pulses are digitized by a TDC (Time to Digital Converter) and subsequently sent to a PC. Here they are saved and can be monitored online via the ROOT (*ROOT website*) based system *go4* developed by the GSI (*go4 website*).

The amount of data that is recorded can be reduced by employing coincidence conditions. This means that data is only recorded when e.g. an electron and a recoil ion are detected with an expected time difference. In transfer ionization, a triple coincidence between the electron, the recoil ion and the charge changed projectile is used. Hereby the background is reduced significantly.

3.2 Magneto optical trap

In the present setup a lithium MOT is used as a target. This has several advantages over gas jets that are conventionally used: the temperature of the target is several orders of magnitude lower than in a gas jet and confined in three dimensions, which results in a higher resolution. Additionally, lithium was chosen as target atom. While it is still a ”simple” atom with only three electrons, its asymmetric electronic structure makes it possible to observe effects for different electronic initial states and for different correlations. It is also possible to optically prepare the target, e.g. excitation and polarization can be performed with specific trapping laser configurations.

In the following the principle of a MOT will be explained as well as the combination with the ReMi. Further details of the following explanations can be found in (Hubele, 2013) and (Metcalf and Straten, 1999).

3.2.1 Working principle of a MOT

A magneto optical trap combines two techniques to produce ultra-cold atoms. While optical cooling with near-resonant lasers traps the atoms in momentum space, the inhomogeneous magnetic fields confines them in position space.

Laser cooling

The working principle of laser cooling is based on the atomic absorption and emission of photons. When an atom absorbs a photon from the laser beam, it absorbs its energy $E = \hbar\omega_l$ and its momentum $\vec{p} = \hbar\vec{k}$ with the magnitude of the wave vector $k = 2\pi/\lambda$, where ω_l is the frequency and λ the wavelength of the photons. The now excited atom decays to the ground state by spontaneous emission of another photon. The momentum gained from the absorbed photon points in laser beam direction, while the photon from the spontaneous emission is emitted isotropically and its momentum averages out over many cycles. Therefore the atom feels a net force F in direction of the laser beam:

$$\vec{F} = \hbar\vec{k}\Gamma \tag{3.1}$$

with the total light absorption and scattering rate Γ as a product of the decay rate $\gamma = 1/\tau$ and the population ρ_{ee} (Metcalf and Straten, 1999)

$$\Gamma = \gamma\rho_{ee} = \frac{\gamma}{2}\frac{s_0}{1 + s_0 + (2\delta/\gamma)^2} \tag{3.2}$$

with $s_0 = I/I_s$ as the ratio of light intensity I to saturation intensity $I_s = \pi hc/(3\lambda^3\tau)$ and the detuning from resonance $\delta = \omega_0 - \omega_l$, ω_0 being the resonance frequency of the transition and ω_l the laser frequency.

Atoms with an initial velocity $v = 0$ receive a push in laser beam direction. The motion of the atoms causes a Doppler shift of the laser light. That can be accounted for by introducing the Doppler term $-\vec{k}\vec{v}$ to the detuning:

$$\delta \to \delta' = \omega_0 - \omega_l - \vec{k}\vec{v} \tag{3.3}$$

If δ is red detuned ($\delta = \omega_0 - \omega_l < 0$), a laser beam counter-propagating to the atom will always be closer to resonance than a co-propagating beam. Therefore the atoms receive a push opposite to their initial velocity and are effectively slowed down.

In the one dimensional case we need two anti-parallel laser beams of the same frequency. In this so-called 1D optical molasses the atoms are slowed down in both directions. However, they are not trapped as there is no restoring force in position space. The resulting force is the sum of the forces from each beam

$$\vec{F}_{OM} = \vec{F}_+ + \vec{F}_- = \sum \pm\hbar\vec{k}\frac{\gamma}{2}\frac{s_0}{1 + s_0 + (2(\delta \mp |\vec{k}\vec{v}|)/\gamma)^2} \tag{3.4}$$

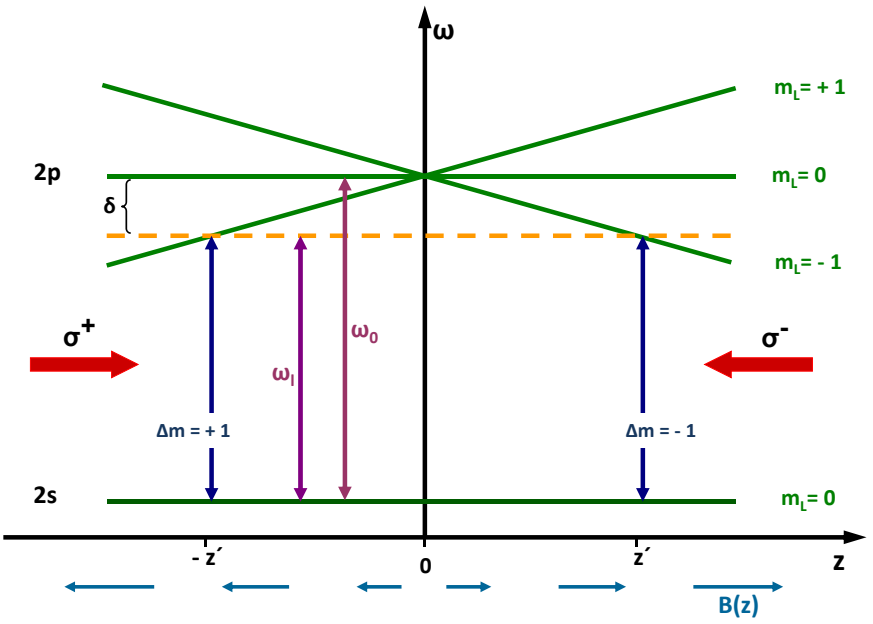

Figure 3.6: Working principle of a MOT. (Hubele, 2013)

For $|\vec{k}\vec{v}| \ll \gamma$ this results in

$$\vec{F}_{OM} \cong \frac{8\hbar k^2 \delta s_0 \vec{v}}{\gamma(1 + s_0 + (2\delta/\gamma)^2)^2} \equiv -\beta\vec{v} \tag{3.5}$$

where β represents an viscous damping coefficient. In order to achieve damping in three dimensions, the principle of the optical molasses can be extended by using three orthogonal pairs of cooling lasers.

Magneto optical trap

By applying an inhomogeneous magnetic field $B(z)$, a position dependent force is added to the optical molasses. It relies on the combination of polarized laser beams and the Zeeman splitting in the field. The general conception in one dimension is shown in fig. 3.6: The atom represents an effective two-level system, in this case the 2s and 2p states of lithium with an energy difference of $\hbar\omega_0$. Neglecting the electron and nuclear spin, the magnetic field introduces a Zeeman shift to the 2p level. The energy splitting induced by the magnetic momenta of the excited state μ_{2p}

$$\Delta E = \mu_{2p} B(z) \tag{3.6}$$

increases with the magnetic field and with the distance to the center at $z = 0$ (where $B = 0$). At a specific point z' the Zeeman shift is as big as the redshift of the cooling laser, which means that an atom with $v = 0$ at z' is in resonance with the cooling laser and receives a push. As a σ^+ (σ^-) photon only induces a $\Delta m = +1$ ($\Delta m = -1$) transition, the polarization of the beams leads to a push that is always directed into the center at $z = 0$. For describing the force on the atoms, the detuning has to account for the Zeeman splitting: $\delta' = \omega_0 - \omega_l \mp \vec{k}\vec{v} \pm \Delta\mu B(z)/\hbar$. For a Doppler

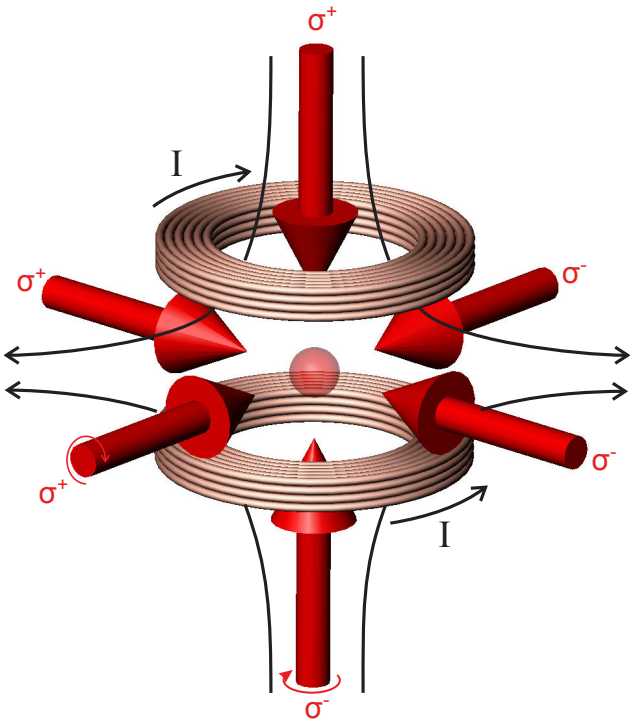

Figure 3.7: Setup of a 3D MOT. While three orthogonal pairs of laser beams with opposite polarizations provide an optical molasses, the confinement in position space is achieved by a quadrupole field generated by a pair of anti-Helmholtz coils. (Steinmann, 2007)

shift and Zeeman splitting small compared to γ the force can be written analogous to eq. (3.5):

$$\Delta F = -\beta \vec{v} - \kappa z \tag{3.7}$$

This equation describes a damped harmonic oscillator, so the atoms are confined and slowed down continuously.

In reality the Zeeman splitting is more complicated (caused by the electron and nuclear spin), however, the general concept of the MOT trapping mechanisms still applies.

In order to achieve magnetic trapping in three dimensions, a quadrupole field generated by anti-Helmholtz coils can be used (see fig. 3.7).

2D MOT

Atoms can only be captured in the 3D MOT if they have already a low velocity. The lithium atoms evaporate from an oven at about 350 °C, so they have to be cooled before they can be captured by the 3D MOT. This pre-cooling is typically done in either a Zeeman slower or a 2D MOT. However, as the magnetic fields of the Zeeman slower can affect the operation of a ReMi, a 2D MOT was employed in the present setup.

The operation of a 2D MOT as a source for cold lithium atoms is described in detail in (Tiecke et al., 2009). The principle is similar to the 3D MOT, but the

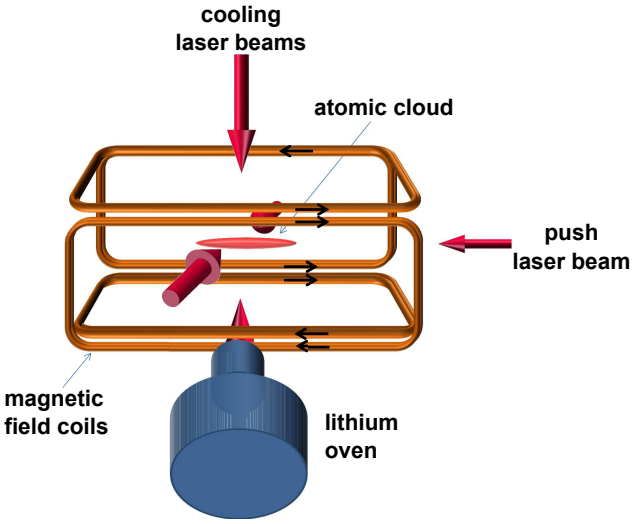

Figure 3.8: Setup of a 2D MOT. (Hubele, 2013)

magnetic trapping and optical molasses are only realized in two dimensions. The third dimension is used to transfer the atoms into the 3D MOT by the means of a push laser.

The experimental setup of the 2D MOT is shown in fig. 3.8. The magnetic field coils generate a uniform field along the push laser beam direction and a gradient of about 60 G/cm in transverse direction. This high magnetic field gradient is needed to capture a large number of lithium atoms from the oven. The whole 2D MOT setup is connected to the main chamber by a differential pumping stage sustaining the ultra high vacuum in the reaction chamber.

3.2.2 Lithium

Lithium was chosen as target due to its interesting electronic structure. It has three electrons and hence is more complex than helium, which has been investigated intensively in ReMis (e.g. (Kollmus et al., 2002; Fischer et al., 2003b)), while still being uncomplicated with only three electrons. Lithium is an alkali metal and therefore has only one electron in the outermost s-orbital. The remaining two electrons are in the 1s orbital ($1s^2 2s^1$). This electron configuration allows to study different strengths of electron-electron interactions by looking either at the two inner-shell electrons (strong e-e interaction like in helium) or at one inner- and one outer-shell electron (weak e-e interaction).

Lithium appears in two stable isotopes, ^{7}Li and ^{6}Li with an abundance of 92.4% and 7.6%, respectively (*NIST Atomic Weights and Isotopic Compositions* 2013). In the presented setup the ^{7}Li isotope is used, which has a nuclear spin of $I = 3/2$. Table 3.1 lists the properties of ^{7}Li that are relevant in the course of this thesis.

As discussed in section 3.2.1 laser cooling works in closed two level systems, more precisely it requires a cycling transition, i.e. the excited state has to decay back into the ground state. Considering the hyperfine splitting, lithium has actually more than two levels (see fig. 3.9): The cooling transition is the D2-line ($2^2S_{1/2} - 2^2P_{3/2}$) with a wavelength of 671 nm. With ideal conditions a cycling transition would be possible between the $2^2S_{1/2}, F = 2$ and the $2^2P_{3/2}, F = 3$ state, because the excited

Parameter	Symbol	Value	[Reference]
Atomic number	Z	3	
Natural abundance	η	92.4%	[1]
Atomic mass	m	7.016 004 u	[1]
		$1.165\,035 \times 10^{-26}$ kg	
Nuclear spin	I	3/2	
Ionization potential Li(1s)	$IP_{\mathrm{LI(1s)}}$	65.4 eV	[2]
Ionization potential Li(2s)	$IP_{\mathrm{LI(2s)}}$	5.4 eV	[2]
Ionization potential Li(2p)	$IP_{\mathrm{LI(2p)}}$	3.5 eV	[2]
Ionization potential Li^+	$IP_{\mathrm{LI^+}}$	75.6 eV	[2]
Ionization potential Li^{2+}	$IP_{\mathrm{LI^{2+}}}$	122.5 eV	[2]
D2-transition($2^2S_{1/2}$–$2^2P_{1/2}$):			
wavelength in vacuum	$\lambda_{\mathrm{vac,D2}}$	670.9616 nm	[3]
frequency	ν_{D2}	446 810.184 GHz	[3]
Energiedifferenz	E_{ph}	1.848 eV	
life time	τ	27.10 ns	[4]
inverse life time	γ	$36.90 \times 10^6\,\mathrm{s}^{-1}$	
natural line width	$\gamma/2\pi$	5.873 MHz	
hyperfinestructure constant $2^2S_{1/2}$	$\alpha_{\mathrm{HFS}}(2^2S_{1/2})$	401.76 MHz	[3]
hyperfinestructure constant $2^2P_{3/2}$	$\alpha_{\mathrm{HFS}}(2^2P_{3/2})$	-3.05 MHz	[3]
hyperfine splitting $2^2S_{1/2}$:			
energy difference	$\Delta E_{\mathrm{HFS}}/h$	803.504 MHz	[3]
cooling frequency D2, $F = 2 \rightarrow 3$	ν_{cool}	446 809.875 GHz	
pumping frequency D2, $F = 1 \rightarrow 2$	ν_{pump}	446 810.688 GHz	

Table 3.1: Atomic and spectroscopic properties of ^{7}Li. The references are: [1] (*NIST Atomic Weights and Isotopic Compositions* 2013), [2] (*NIST Atomic Spectra Database* 2013), [3] (Das and Natarajan, 2007), [4] (McAlexander et al., 1996).

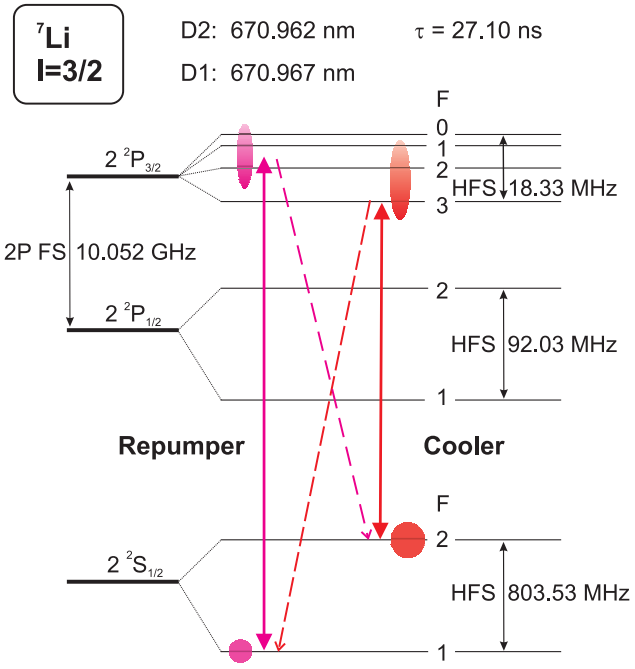

Figure 3.9: Fine and hyperfine structure of lithium. The two cooling laser (cooler and repumper) utilize the D2-transition. (Steinmann, 2007)

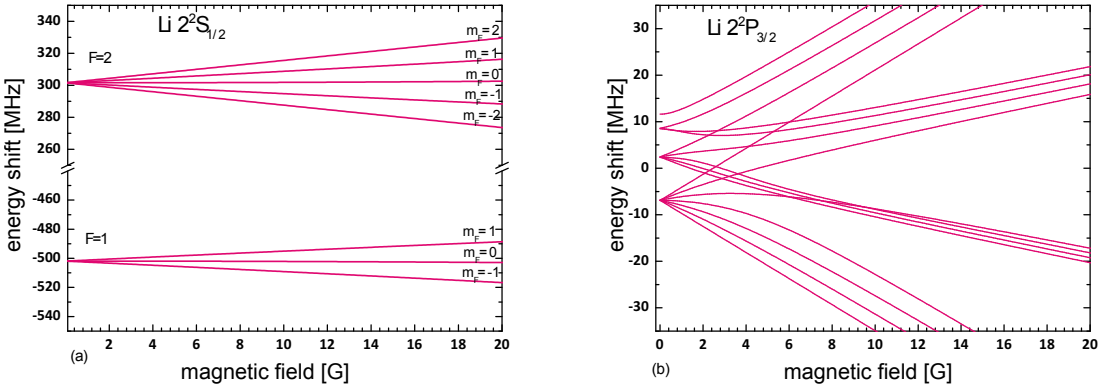

Figure 3.10: Hyperfine structure and Zeeman shift of lithium. (a) shows the $2^2S_{1/2}$ ground state and (b) the $2^2P_{3/2}$ excited state. (Hubele, 2013)

$|F = 3\rangle$ state can only decay to $|F = 2\rangle$ due to selection rules. But as the hyperfine splitting of all four $2^2P_{3/2}$ states is only 18.33 MHz, the cooling laser populates all of theses sub-states. Therefore some atoms decay to the $2^2S_{1/2}, F = 1$ state, which is a dark state, because the atoms cannot be excited from this state as they are far from the resonant transition. This effective coupling between the two $2^2S_{1/2}$ states can be countered by using a second laser frequency (the repumper), which is shifted by the hyperfine splitting of the ground state (800 MHz) as illustrated in fig. 3.9.

In an external magnetic field the hyperfine levels split due to the Zeeman effect (fig. 3.10). While in the ground state the I - J coupling is preserved, it breaks already for quite low magnetic fields in the excited state. This is caused by a small hyperfine structure constant of the excited state. At a typical magnetic field in the ReMi of 10 G the quantum number F is not preserved anymore, but the magnetic field is still too low for I an J to be decoupled completely.

3.2.3 Laser setup

The laser system has to provide a narrow bandwidth in the order of or smoother than the natural linewidth of the used transition ($\gamma/2\pi = 5.873\,\mathrm{MHz}$). At a wavelength of 671 nm this corresponds to a stability of 10^{-8}.

This stability can be achieved by an external-cavity-diode-laser (ECDL) in Littrow-configuration, which is shown in fig. 3.11 (a). The diffraction grating is selective to the wavelength $\lambda = g\sin(\phi)/n$ with the grating constant g, the angle of deflection ϕ and the refraction order n. Hence the output wavelength can be chosen by the angle of the grating. With this setup only a small part of the broad spectrum of the diode is back-reflected and amplified - the bandwidth is smaller than 1 MHz.
However, the maximum power that can be achieved with this kind of laser diode is about 30 mW for the required frequency, while several hundred mW are needed for the setup. Therefore the light is subsequently amplified in a Tapered Amplifier (TA, see fig. 3.11 (b)). Here the laser beam enters a single mode channel, which acts as a spatial mode filter. In the tapered gain region this mode cleaned beam gets amplified without losing its spectral and spatial characteristics (*High Power Diode Lasers and Amplifiers*).
Another important part of the laser setup are the Acousto-optic modulators (AOM). An AOM consists of a crystal that is attached to a piezoelectric transducer. By connecting an oscillating signal the transducer vibrates, which is transferred to the crystal. The resulting sound waves (or phonons) change the refraction index of the crystal and hereby create an optical lattice. A laser beam that hits the crystal at the Bragg angle changes its frequency by the multitudes of the phonon frequency $\nu_{Photon} \rightarrow \nu_{Photon} + m\nu_{Phonon}$, with $m \in \mathbb{Z}$. The intensities of the different orders can be varied by the intensity of the sound waves. These AOMs allow to change the frequency of a laser beam over several hundred MHz in about 100 ns.

The used laser setup changed several times in the course of this thesis, here only one version will be presented (see fig. 3.12). From the laser source a small part of the intensity is used to lock the laser frequency with the help of *Doppler-free saturation spectroscopy* (Bjorklund et al., 1983), which is explained in the following:

The beam is retro-reflected through a spectroscopy cell filled with hot lithium before its intensity is measured with a photo diode. By modulating the frequency periodically, a Doppler-broadened spectrum can be seen (fig. 3.13 (b)). The general shape (without the small peaks a,b,c) is the sum of the $2^2S_{1/2}, F = 1 \rightarrow 2^2P_{3/2}$ and the $2^2S_{1/2}, F = 2 \rightarrow 2^2P_{3/2}$ transitions.

The peaks a and c are called "Lamb-dips" and are caused by a saturation effect: atoms moving with velocity v see a Doppler-shifted beam and therefore absorb the beam from one direction more likely, hence the opposite beam excites different atoms. If the atoms have zero velocity in beam direction, they are excited by both beams in the same way, which results in less overall absorption of the laser light due to saturation.

The feature at b is the so-called "crossover-peak". If the Doppler shift of an atom is half the hyperfine structure splitting of the ground state of lithium (about 400 MHz), it can absorb both the cooler and the repumper laser beams from opposite directions. Due to rapid redistribution, no depopulation can occur, which means that both hyperfine states are populated constantly. Thus, these atoms can be continuously

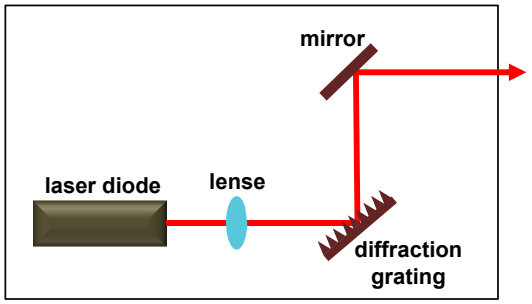

Figure 3.11: Working principle of a ECDL in Littrow configuration (a) and a Tapered Amplifier (b). (Hubele, 2013), (*High Power Diode Lasers and Amplifiers*)

pumped, which results in a minimum in the absorption spectrum. This minimum is the locking frequency, in our case 446 809.782 GHz.

The remaining part of the laser setup is straightforward: the beam is split into a repumper and a cooler part, which are frequency shifted by about ±400 MHz. This is accomplished by two AOMs, where the beams pass twice, each time being shifted about ±200 MHz. A small part of the repumper beam is used for the push laser, while the main part is overlapped with the cooler and used for the 2D and 3D MOT beams, respectively. Normally three back-reflected beams are used for a 3D MOT, in the presented setup one is reflected three times in order to cover two dimensions and hereby reduce the necessary intensities.

3.2.4 MOTReMi

The combination of a MOT and a ReMi bears the problem of two magnetic fields. While the MOT needs an inhomogeneous magnetic field with a high gradient in order to capture and trap atoms, the ReMi requires a homogeneous magnetic field to detect electrons. These problems are addressed in the two following sections.

3.2.4.1 Operation of a ReMi with a MOT

A ReMi measures the momentum distribution of the particles involved in a collision process, e.g. low energetic electrons. A quadrupole magnetic field such as used in a MOT would make the momentum reconstruction impossible. Hence it has to be switched off during measurements, which has to happen quite fast as the MOT is expanding rapidly without spatial confinement.

For fast switching it is essential to prevent eddy currents. Therefore the main aim is to spatially confine the magnetic field while keeping the field gradient. This was done as illustrated in fig. 3.14. (a) shows a MOT coil setup used e.g. in (Steinmann, 2007). In order to achieve the aim mentioned before, first the distance and diameter of the coils were scaled down (b), then compensation coils were employed (c). These compensation coils have a slightly larger diameter and distance than the MOT coils, but are connected to the same current, only in the opposing direction. This setup reduces the field at the chamber walls (distance about 20 cm from the center) by a

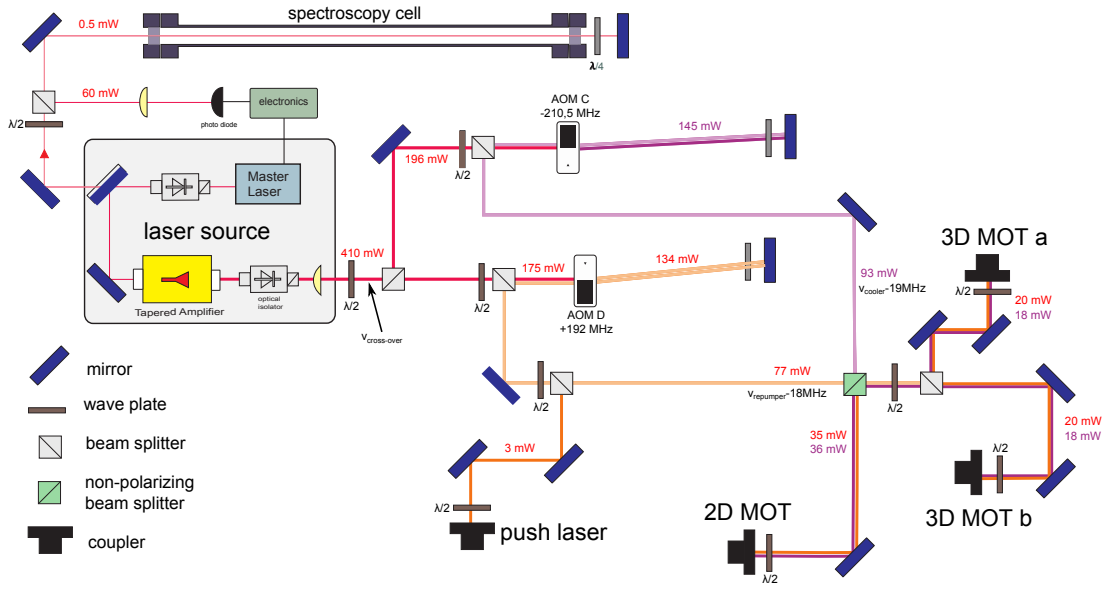

Figure 3.12: Schematic overview of a typical Laser setup. The main laser source is the gray box; the spectroscopy cell in the upper left is used for Doppler-free saturation spectroscopy. The part on the right shifts the frequencies to the needed ones. Based on (Hubele, 2013).

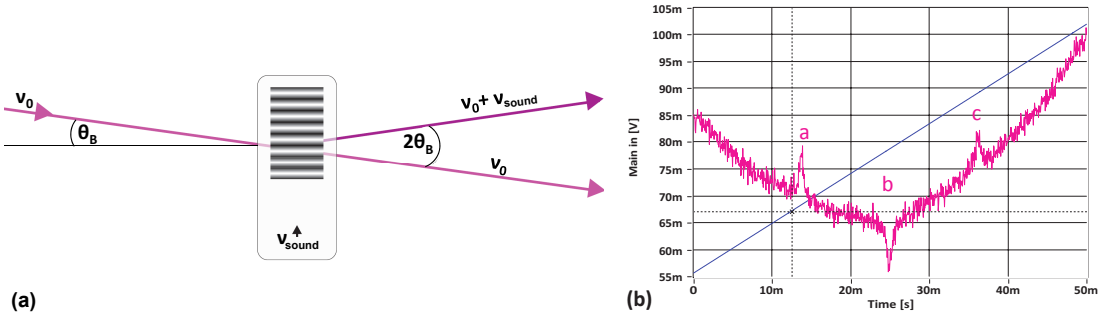

Figure 3.13: Working principle of an AOM (a) and absorption signal of the FM-spectroscopy (b). Here 10 ms relate to about 1 GHz frequency difference. (Hubele, 2013)

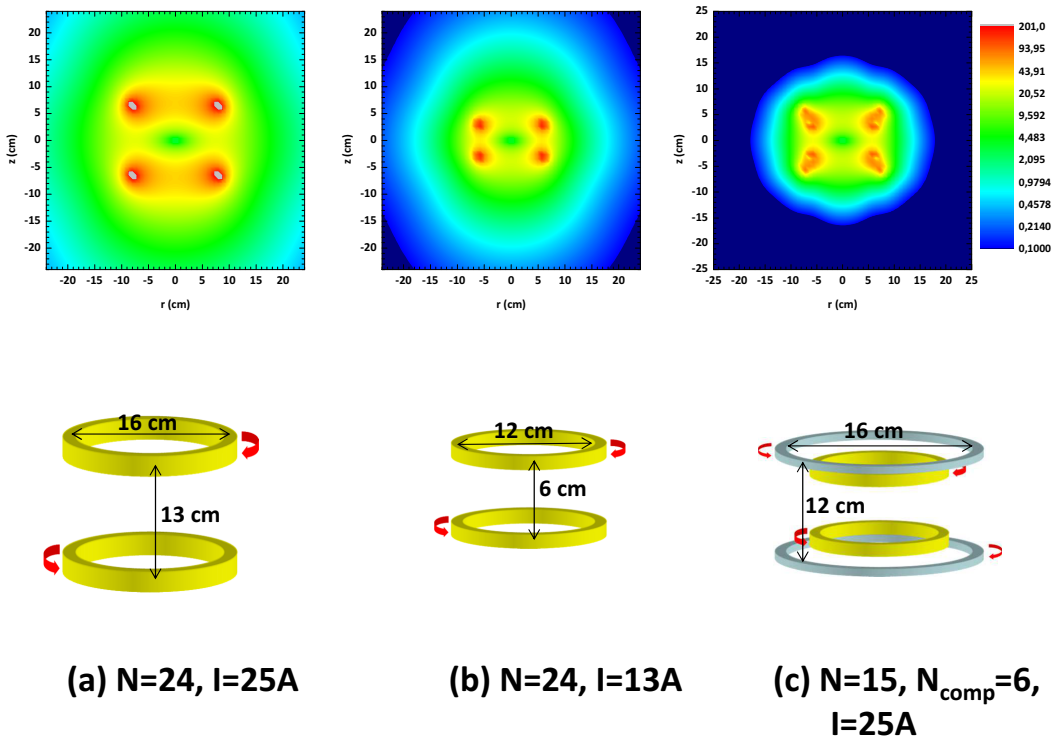

Figure 3.14: Magnetic fields of different MOT coil setups. (Hubele, 2013)

factor of 100 in comparison to a conventional setup shown in (a) and by a factor of 10 in comparison to (b) without compensation coils.

The switching of the current is done with a bridge circuit involving MOSFETs. This allows to switch off a current of 20 A in less than 250 µs. The duty cycle is illustrated in fig. 3.15. Data acquisition runs for about 900 µs while the magnetic field is completely switched off. Within this period also the cooling laser can be switched off (in fig. 3.15 for 200 µs) in order to allow for 100% 2s population of the target atoms. Then the recapturing begins - after about 4 ms the MOT has regained its original size and the magnetic field can be switched off again. The resulting relative measurement time is about 21%. In later experiments, duty cycles up to 50% have been achieved.

3.2.4.2 Operation of a MOT in a ReMi

The operation of the MOT is disturbed by the switching of its magnetic field explained above and by the homogeneous magnetic field of the ReMi.

When the MOT magnetic field is switched off, the number of atoms in the interaction volume decreases exponentially. In order to maintain a reasonable duty cycle, the cooled atoms have to be recaptured instead of completely loading the trap again. This is possible with the duty cycle shown in fig. 3.15 and was operated successfully in several MOTRims experiments before (Blieck et al., 2008; Steinmann, 2007).

A more complicating issue arises when adding the homogeneous field for electron detection, which is the reason why no previous MOTRims experiment could detect electrons. For electron detection a magnetic field is added in z-direction along the

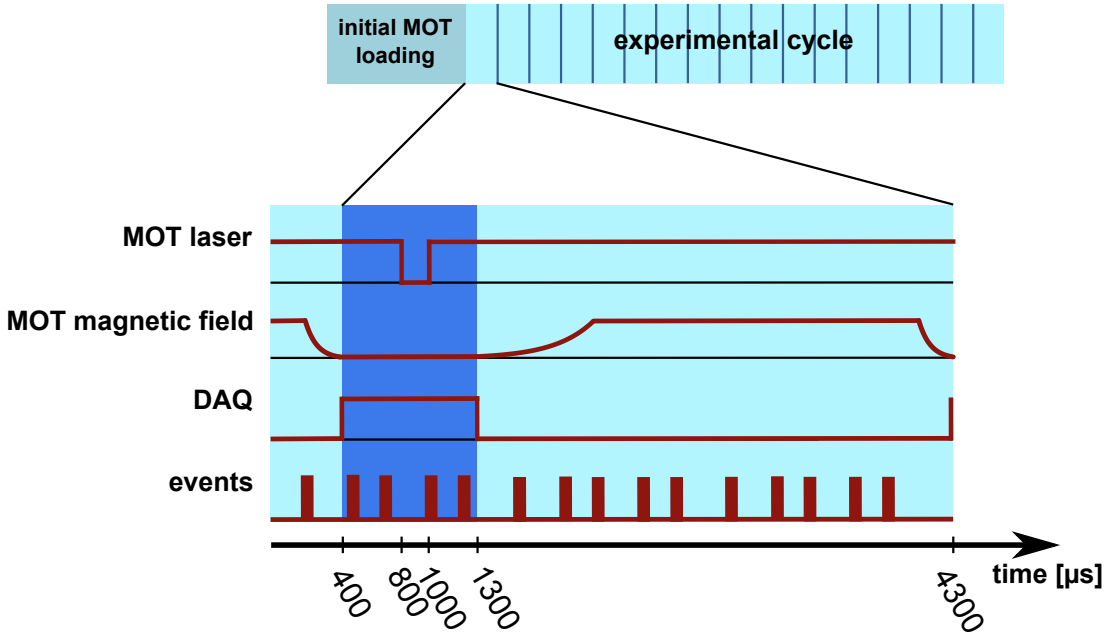

Figure 3.15: Typical duty cycle during measurements.

TOF axis of the particles. This changes the zeropoint of the magnetic quadrupole field as shown in fig. 3.16 (a). Hence in the normal 3D MOT operation with σ^+ - σ^- light there is an imbalance of the forces from the two directions (see the bottom of fig. 3.16 (a)) resulting in a shift of the MOT cloud. This hinders experiments as the cooled atoms are lost after only one switching cycle and the MOT would have to be reloaded, which takes about 1 s or longer. So a different setup was employed by using the same longitudinal laser polarization for both beams (fig. 3.16 (b)). Here the MOT does not shift anymore while switching, as there is no spatial confinement in longitudinal direction anymore, which obliterates the influence of the changing zero-point of the magnetic field. We refer to this configuration without positional trapping in z-direction as "2.5D MOT".

In order to achieve a high density, a different kind of trapping mechanism in z-direction was employed. A slight disalignment of the laser beams led to the best MOT operation. This effect was first reported in 1987 by the group of Chu and called "supermolasses" (Chu et al., 1987), where they observed an increase in storage time with disaligned laser beams. In the context of a MOT, similar behavior was observed by Walker et al. in 1992. Their "vortex-force atom trap" works on the principle of disaligned laser beams. Like in our case, they used typical MOT trapping in two dimensions, while in the third dimension the laser beams had the same polarization, σ^+ - σ^+ in (Walker et al., 1992b) and linear polarization in (Walker et al., 1992a). In the latter even a field gradient along the z-axes was absent. The vortex and MOT trapping can be described by a viscous damping force $-\alpha\vec{v}$, where $\vec{v}$ is the velocity. The equations of motion in the drift approximation are a vortex force in y and z direction and a trapping force in x and y direction: $\alpha v_x = -kx$, $\alpha v_y = -k'z - ky$ and $\alpha v_z = k'y$ which results in a spiraling motion towards $x = y = z = 0$.

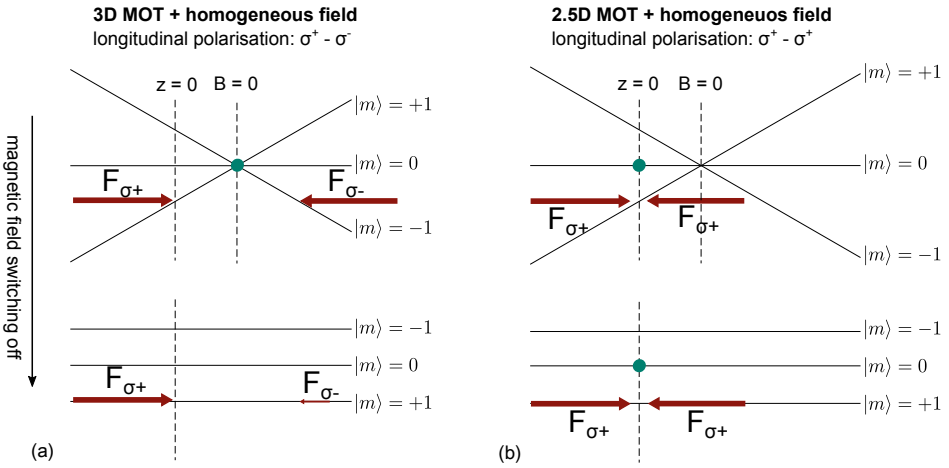

Figure 3.16: MOT positions during switching in a homogeneous field. (a) illustrates normal σ^+ - σ^- MOT polarization and (b) equal polarization (here σ^+ - σ^+).

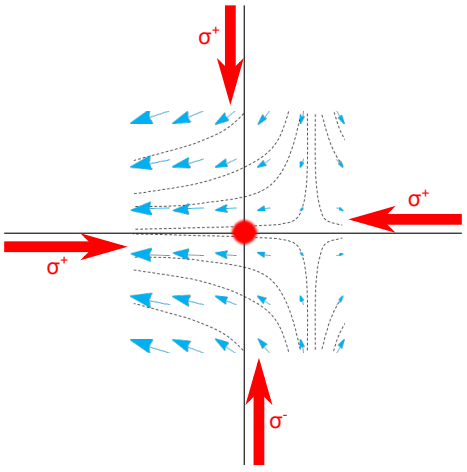

Figure 3.17: Mechanism of the vortex force created by dis-aligned laser beams.

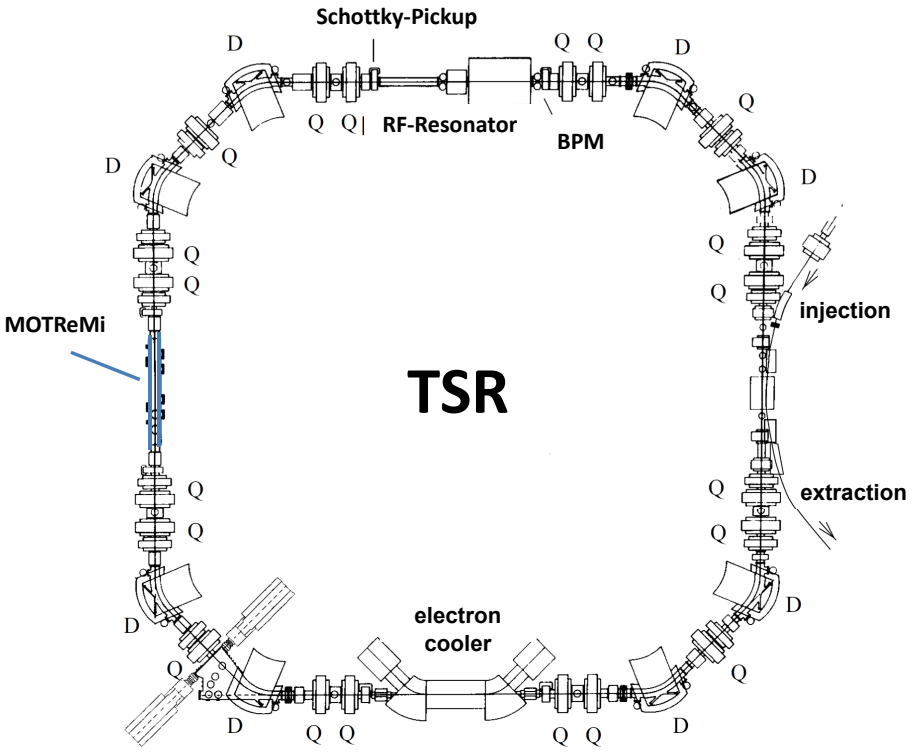

Figure 3.18: Structure of the TSR. (Grieser et al., 2012)

3.3 The ion storage ring TSR

In the late 1980s and early 90s the new technique of phase space cooling and an improved vacuum technology at moderate costs led to the construction of several small storage rings, which made it possible to store highly charged ions at several tens of MeV/amu. The Test Storage Ring TSR is one of these heavy ion cooler storage rings.

In the presented setup the TSR provides the projectile beam, which has several advantages in comparison to single pass experiments. First, a much higher beam intensity is possible by multi injection and secondly the beam is cooled and has therefore much better coherence properties ($\Delta p/p$) as well as a small emittance and beam size. In this chapter a brief summary of the TSR will be presented, for further details see (Grieser et al., 2012).

The structure of the TSR

An overview over the TSR can be found in fig. 3.18. Its circumference is 55.4 m and it has a fourfold symmetry. Each quarter contains five quadrupole magnets (labelled Q) for focusing and two dipole magnets (labeled D) with a bending radius of 45° each. As the adjacent focusing periods are antisymmetric, the superperiodicity of the ring is two. The four straight sections contain the beam injection/extraction, the electron cooler, the MOTReMi and the beam diagnostics and rf resonator, respectively. These will be explained separately in the following chapters.

Beam dynamics When an ion with transverse momentum propagates through the storage ring, it would be lost without the focusing magnets. These induce an

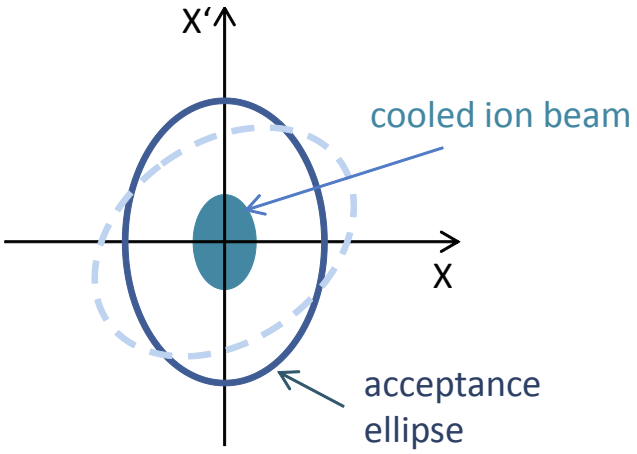

Figure 3.19: Phase-space ellipse of an ion in a storage ring. (Schneider, 2012)

oscillation of the stored particles, the so-called betatron oscillation. In the phase-space spanned by $x' = p_x/p_\parallel$ (with the momentum in transverse direction p_x and the momentum in beam propagation direction $p_\parallel$) and the transverse displacement x this results in an ellipse (e.g. fig. 3.19). The emittance ϵ is defined as $A = \pi \cdot \epsilon = \pi \cdot x'_{max} \cdot x_{max}$ with the area of the phase space ellipse A, while the acceptance is the largest emittance that is possible.

For an ion beam instead of x the standard deviation σ_x of its Gaussian shape is used. The electron cooling reduces the emittance of the beam significantly.

Beam production and injection

First, negative ions from p^+ to U^+ are generated by different kinds of sources (*The Heidelberg Ion Beam Facilities*). These are mostly created by gas discharge, where a gas is ionized by a flow of electric charge, or by a Cs sputter, where Cs^+-ions bombard a target from which ions are sputtered. A tandem Van-der-Graaf accelerator (Repnow et al., 1974), which can operate voltages of up to 12 MV, subsequently accelerates the ions. The high voltage is generated like in a Van-der-Graaf generator, where electrons are physically transported to a terminal. The negative ions are accelerated towards the terminal and stripped to change their charge polarity, which results in two accelerations - hence the name "tandem" accelerator. Before entering the beam line, a foil or gas target strips off electrons to create the desired charge state.

The beam is injected by using an electrostatic and two magnetic septa. In the TSR it is possible to inject while keeping the beam stored, which is called multi-turn injection. Hereby the position space can be filled completely. This technique permits stable beam currents over long time periods, as the existing beam can be intensified after a certain storage time.

Electron cooling

Electron cooling is applied in order to reduce the energy spread of the ion beam. An electron beam with the same velocity as the ion beam is merged with the latter. The ions undergo Coulomb scattering with the electrons and hence lose temperature until an equilibrium between intra-beam scattering and electron cooling is reached.

This technique reduces the beam size in the TSR from up to 40 mm directly after injection to only a few mm.

Electron cooling allows to apply the so-called electron cooling stacking. As the cooled ion beam now occupies much less phase space, this free space can be filled by means of multi-turn injection and cooled again. That technique leads to a much bigger beam intensity, only limited by the lifetime of the beam.

The life time of a stored ion beam is primarily influenced by interactions with the residual gas and the electrons in the electron cooler. These interactions mainly include Coulomb scattering, electron stripping and electron capture. The resulting life time of an ion beam depends on its charge and energy as well as the vacuum conditions in the TSR. E.g. a life time of 1.5 MeV/amu O^{8+} during the experiments described later was about 15 min.

Bunching of the beam

For collision processes it is important to have a time information of the projectile. This can be obtained by bunching the beam. Therefore a rf resonator applies a radio frequency at a multiple of the circulation frequency of the beam. The harmonic number is the number of bunches in the ring, their length is a few ns. This bunch length depends on the resonator voltage and the velocity and intensity of the ion beam.

4. Data analysis

In this chapter the analysis of the experimental data and its presentation will be described. After a reaction, the charged fragments are mapped on a detector, delivering position and time-of-flight information. The main task is to reconstruct the momenta directly after the collisions from these signals (section 4.1). In the presented experiments, photo ionization measurements with a UV-laser were used to calibrate the spectra as well as to attain the resolution of the experiment (section 4.2). The presentation of the results as differential cross sections will be discussed subsequently (section 4.3). The last part of this chapter will introduce a technique that addresses a general problem of ReMis. This "wiggle correction" method allows to reconstruct parts of the electron momentum space that is in other experiments not accessible due to the rather complicated cyclotron motion of the electrons in the magnetic field (section 4.4). However, this method is only applicable to setups in which the projectile beam axis is tilted with respect to the spectrometer axis. In the following atomic units will be used, if not otherwise noted.

4.1 Momentum reconstruction

The *go4* analysis software (*go4 website*) calculates from the raw data the position and time-of-flight (TOF) information of the charged fragments on both detectors as well as the time reference from the data acquisition system. With this information, the initial momenta of all involved particles can be calculated.

As the processes are cylindrically symmetric, the momenta are calculated in cylindrical coordinates. Longitudinal and transverse components will be discussed separately in the following.

4.1.1 Longitudinal momentum

The longitudinal momentum components, i.e. the one parallel to the symmetry axis, can be calculated solely with the TOF of the particle. The magnetic field has no influence, as the Lorentz force affects only the motion perpendicular to the spectrometer axis.

The TOF t of a particle of charge q and mass m, that has initially a momentum $p_\parallel$ and then propagates through an acceleration region with a potential change of qU and length l_a and a drift region with length l_d, is

$$t(p_\parallel) = m \cdot \left(\frac{2l_a}{\sqrt{p_\parallel^2 + 2mqU} \pm p_\parallel} + \frac{l_d}{\sqrt{p_\parallel^2 + 2mqU}} \right) \tag{4.1}$$

where the "+" is used for an initial particle emission in detector direction, and the "-" for emission opposite to the detector.

This formula cannot easily be inverted analytically. Moreover, the absolute TOF measured as the time of the instant of the collision is determined only with an offset. To overcome these obstacles, different methods are employed to calculate the momenta of the electrons and the recoil ions.

The recoil momentum can be calculated with an approximation: the momentum received in the collision $p_\parallel$ is several orders of magnitude smaller than the momentum gained in the electric acceleration field $\sqrt{2mqU}$. Thus, Δt can be approximated with the first order of the Taylor series around $p_\parallel = 0$

$$\Delta t_r = t(p_{r\parallel}) - t(p_{r\parallel} = 0) \approx \left[\frac{dt_r(p_{r\parallel})}{dp_{r\parallel}} \right]_{p_{r\parallel}=0} \cdot p_{r\parallel} \tag{4.2}$$

which results in (Fischer, 2003)

$$p_{r\parallel} = \frac{qU}{a} \Delta t_r \tag{4.3}$$

For the electrons this approximation is not valid, as the momenta gained in the collision and in the acceleration field are about equal because of the small electron mass. Hence eq. (4.1) is inverted numerically; here the Newton iteration was used. For this method the absolute TOF is required, which can be derived from the so-called wiggle spectrum shown in fig. 4.1. The electrons propagate in a cyclotron motion in the magnetic field. Electrons with no transverse momentum hit the detector on the spectrometer axis ($r = 0$), just as they do with any transverse momentum after an integral multiple of the full cyclotron period $T_c = 2\pi\omega_c$. The zero point of the TOF has to be such a wiggle, therefore a calculation of the electron TOF can be used to find the wiggle for $t = 0$ with high precision.

4.1.2 Transverse momentum

The transverse momenta can be calculated from the position and TOF of the electrons and recoil ions. Again, the calculation differs for electrons and ions, as for the electrons the motion in the magnetic field has to be accounted for. In fig. 4.2 the parameters needed in the calculation are shown.

For the recoil ion, the radius r on the detector is proportional to the TOF t_r and the transverse momentum $p_{r\perp}$:

$$r = \frac{p_{r\perp} t_r}{m_r} \tag{4.4}$$

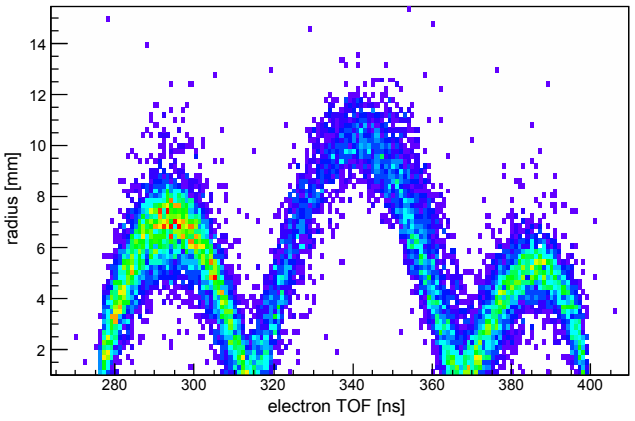

Figure 4.1: Radius r versus TOF t for electrons. The radial distribution features nodes for different TOFs, at e.g. $t = 314\,\text{ns}$ the cyclotron angle $\alpha = 0°$ and all electrons are at $r = 0$ (for an illustration of α and r see fig. 4.2), at $\alpha = 180°$ r is maximal and at about $t = 368\,\text{ns}$, $\alpha = 360°$ and $r = 0$ again. This structure is repeated several times, depending on the broadness of the electron TOF and the magnetic field. These knots (also called 'wiggles') appear in each cyclotron orbit ($n \cdot 360°$ with $n \in \mathbb{Z}$).

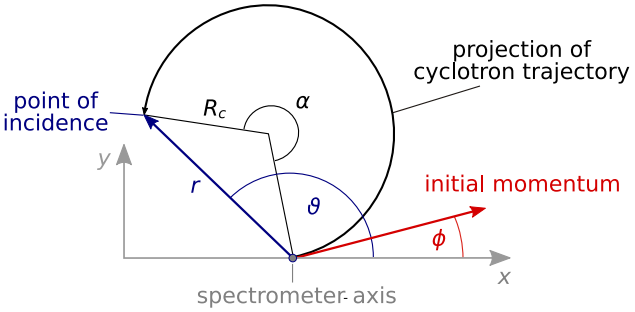

Figure 4.2: Parameters for the transverse momentum calculation. The cyclotron motion is illustrated as a projection in the azimuthal plane (i.e. perpendicular to the spectrometer axis). r and θ are measured as positions on the detector, R_c and α are the radius and angle of the cyclotron motion and ϕ is the angle of the momentum directly after the collision. (Senftleben, 2009)

with the ion mass m_r. t_r can be expressed with eq. (4.1) at $p_\parallel = 0$, because the change in TOF caused by the kick in the collision is several orders of magnitudes lower than the whole TOF. For the longitudinal recoil ion momentum it is obtained:

$$p_{r\perp} = \sqrt{mqU} \cdot \frac{r}{2l_a + l_d} \tag{4.5}$$

The angle of the initial momentum can be calculated from the position information $\phi = arctan(y/x)$. Here the magnetic field has to be considered, as it turns the trajectory of the ions around the spectrometer axis. However, this can be corrected easily in the calibration process (see section 4.2).

For the transverse momentum of the electrons the cyclotron motion caused by the magnetic field B with the frequency ω_c has a much stronger effect as a cyclotron period is typically much shorter than the electron TOF. It is:

$$\omega_c = \frac{qB}{m_e} \tag{4.6}$$

where q and m_e are the charge and mass of the electron. ω_c can be derived from fig. 4.1 as the distance between two adjacent wiggles. Geometrical considerations give the relation between r, R_c and α:

$$R_c = \frac{r}{2|sin(\alpha/2)|} \tag{4.7}$$

The transverse momentum is obtained with $p_{e\perp} = \sqrt{p_{ex}^2 + p_{ey}^2} = \omega_c m_e R$ and $\alpha = \omega_c t$:

$$p_{e\perp} = \frac{\omega_c m_e r}{2|sin(\omega_c t/2)|} \tag{4.8}$$

With the θ-angle the initial momentum angle can be calculated:

$$\phi_e = \theta - \frac{\omega_c t}{2} \tag{4.9}$$

4.2 Photoionization calibration measurements

The MOTReMi setup includes a UV-laser, which is used to ionize the lithium atoms in order to analyze the properties of the spectrometer. As the energy and momentum width of a laser are much smaller than the expected resolution of a ReMi, such a laser is a good choice to calibrate the spectrometer and determine the resolution. A more detailed discussion can be found in (Hubele, 2013).

The used laser is a passive Q-switched Nd:YAG solid state laser from *TeemPhotonics*, which provides 400 ps pulses at a wavelength of 266 nm. The peak power is 4 kW and the repetition rate is 7 kHz. At this wavelength the photon energy is $E_{ph} = 4.66\,\text{eV}$, which does not allow ionizing the ground state of lithium. However, as described in section 3.2.2, about 20% of the atoms are in the excited $2^2P_{3/2}$ state and these can be ionized, resulting in an excess energy of

$$E_{ph} - I_p = E_e + E_r = 1.12\,\text{eV} \approx E_e \tag{4.10}$$

with the kinetic electron energy E_e, the recoil ion energy E_r and the ionization potential I_p (see fig. 4.3). The momentum is equally shared between the recoil ion and the electron, as the photon has a negligible momentum:

$$p_r \approx p_e = \sqrt{2m_e E_e} = 0.287\,\text{a.u.} \tag{4.11}$$

Therefore, all the intensity in the final state momentum is on a spherical shell, which allows to calibrate easily the spectrometer and determine its resolution.

Calibration

For an accurate momentum calculation using the equations derived above, the knowledge of the exact electric field profile is necessary. As it is not easy to measure this, the above mentioned momentum distribution can be utilized. Electrons as well as protons have the momentum of 0.287 a.u. in UV-photoionization, hence the parameters (i.e. time offsets, voltages, length of drift and acceleration region, etc.) have to be adjusted accordingly.

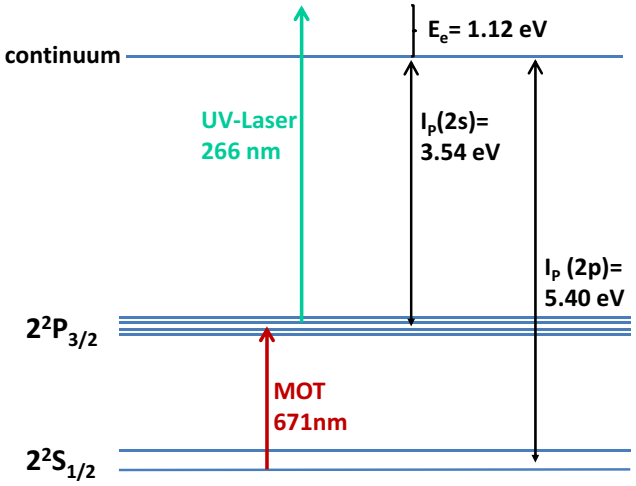

Figure 4.3: Energy level diagram to illustrate the UV photoionization. (Hubele, 2013)

	$\Delta p_\perp$ [a.u.]	$\Delta p_\parallel$ [a.u.]
recoil ions	$\geq$0.07	$\geq$0.035
electrons	0.1	0.01

Table 4.1: Longitudinal and transverse momentum resolution for electrons and ions in the MOTReMi setup.

Resolution

The resolution in a MOTReMi depends on many factors. The initial temperature of the target atoms given by the MOT temperature, the size of the reaction volume defined by the spatial overlap of the MOT and the projectile beam, the field inhomogeneities of the electric and magnetic fields and the temporal length of the projectile bunch influence the resolution as well as the accuracy of the detectors in position and time measurement. Caused by the wiggles (see fig. 4.1) the electron transverse momentum resolution also varies with the TOF. The best resolution is achieved in the center between two wiggles, as here the radius is at its maximum.

With the help of the photoionization spectra the resolution of the whole setup can easily be determined. The resulting values for this setup are shown in table 4.1. While the resolution for electrons is similar to that of other ReMis, the recoil ion resolution is significantly improved (by a factor of 2 to 4 compared to most other setups).

Acceptance

The acceptance in a ReMi depends on the particle species and its emission direction. The forces acting on a particle depend on its mass and charge, which is the reason for a different acceptance for electrons and ions. When a particle is emitted in transverse direction, the acceptance is limited by the detector size and defined by the electric and the magnetic fields. In longitudinal direction the particle can be emitted towards its detector or in the opposite direction. All particles are detected that are emitted towards the detector; if emitted backwards, the acceptance depends on the electric field strength.

For lithium **ions** the longitudinal acceptance in backwards direction depends on the spectrometer voltage U.

$$p_{\parallel,\max}[\text{a.u.}] = 30.62 \cdot \sqrt{q[\text{a.u.}]U[\text{V}]} \tag{4.12}$$

The transverse acceptance is generally limited by the detector size. A formula can be derived from eq. (4.4) and the maximum transverse momentum, which is for $p_\parallel = 0$:

$$t(p_\parallel = 0) = m \cdot \left(\frac{2l_a + l_d}{\sqrt{2mqU}} \right) \tag{4.13}$$

resulting in the maximum transverse momentum of

$$p_{\perp,\max} = r \cdot \frac{\sqrt{2mqU}}{2l_a + l_d} \tag{4.14}$$

$$p_{\perp,\max}[\text{a.u.}] = 2.15 \cdot \sqrt{q[\text{e}]U[\text{V}]} \tag{4.15}$$

where the maximum radius on the detector $r = 40\,\text{mm}$, the lithium mass and the spectrometer lengths were inserted in the latter.

For **electrons** the longitudinal acceptance for an electron emitted in backwards direction is similar to eq. (4.16), but with a different factor originating from the mass difference:

$$p_{l,max}[\text{a.u.}] = 0.27 \cdot \sqrt{U[\text{V}]} \tag{4.16}$$

The transverse acceptance depends on the magnetic field. Equation (4.8) gives

$$p_{r,max}[\text{a.u.}] = 0.16 \cdot B[\text{G}] \tag{4.17}$$

for a detector size of 80 mm. In ReMis, the acceptance of electrons is also restricted by the cyclotron motion. After each full cyclotron period the cyclotron radius is zero, which results in no resolution of the transverse momentum. This issue will be discussed in more detail in section 4.4.

4.3 Cross sections in atomic collisions

The observable in the presented experiments is the cross section. In fully differential cross sections (FDCS) all free parameters of the collision process are fixed – the process is kinematically completely determined (besides the spin). In single ionization this is the case for fixed emission of the electron into a fixed solid angle $d\Omega$, fixed electron energy dE_e and momentum transfer dq:

$$FDCS = \frac{d^3\sigma}{d\Omega dE_e dq} \tag{4.18}$$

Such an FDCS is illustrated in fig. 4.4 (a), here the target is ionized by photon impact. The emission angle of the electron is plotted in three dimensional polar plot; the further away from the point of the collision the larger the cross section, i.e. the probability for emission in this direction. When an electron is ionized from an s-state, a dipole transition (as induced by a single photon) leads to an ionized electron in the p-state, which has an $\cos^2$ angular distribution with respect to the

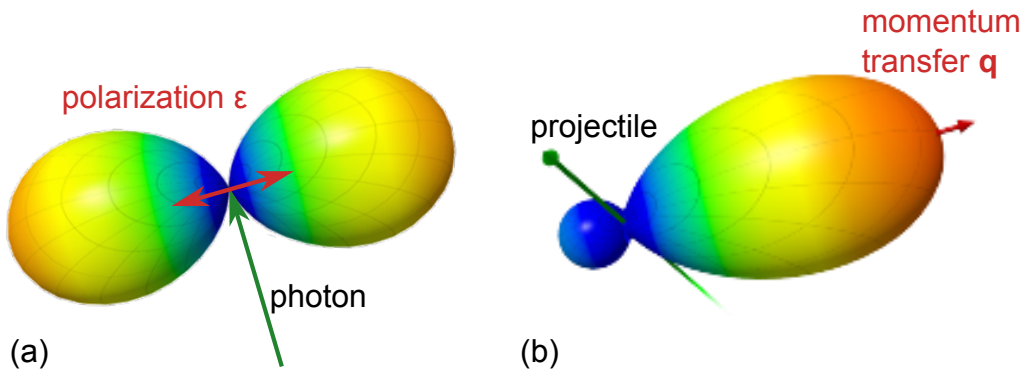

Figure 4.4: Illustration of FDCS for ionization by a photon (a) and by a projectile (b, (Schulz et al., 2003)).

polarization direction $\boldsymbol{\epsilon}$ (only $m_l = 0$ contributes (see eq. (2.41))). This results in a symmetric distribution with a suppressed emission perpendicular to this axis.

As noted in section 2.3.1.1, for high perturbations ionization by a projectile (e.g. electrons or ions) can be described by the exchange of a virtual photon, i.e. the FDCS should be similar to that in photoionization. In fig. 4.4 (b) such a FDCS is shown, and indeed a double lobe structure can be observed, with the symmetry axis being the momentum transfer $\mathbf{q}$. In photoionization no momentum is transferred, hence the similarity is most pronounced at vanishing momentum transfer, while the relative size of the lobes changes with increasing $|\mathbf{q}|$, caused by a preferred electron emission in $\mathbf{q}$-direction. Such structures were observed for electron (Ehrhardt et al., 1969; Lahmam-Bennani, 1991; Coplan et al., 1994) and for ionic projectiles (Schulz et al., 2001). In a classical picture these two peaks can be explained by a two and respectively a three body process (Coplan et al., 1994; Lahmam-Bennani, 2002; McConkey et al., 1972): the large peak in $\mathbf{q}$-direction is the interaction only of the projectile with the electron, the target is only a spectator, hence the name 'binary' peak. The electron is emitted in the opposite direction, when it is scattered from the potential of the residual ion after the collision (called 'recoil' peak). This is a three body process between the electron, the target atom and the projectile. More details on this can be found in (Ehrhardt et al., 1986).

For a quantitative comparison between experiment and theory it is sensible to look at cuts of these FDCS. The general coordinate system with the two planes that are important in the work is illustrated in fig. 4.5. The scattering (or xz) plane is spanned by the projectile momentum ($\mathbf{p}_0^i$) and the momentum transfer $\mathbf{q}$, while the azimuthal (or xy) plane is perpendicular to the initial projectile momentum.

In some cases it is interesting to integrate over one parameter, e.g. the momentum transfer, in order to investigate the dependence on only two parameters. These are the doubly differential cross sections $d\sigma/(d\Omega dE_e)$. Integration over another parameter gives the single differential cross sections, e.g. $d\sigma/dE_e$, which in this case allows to investigate the contribution of different electron energies to the total cross section.

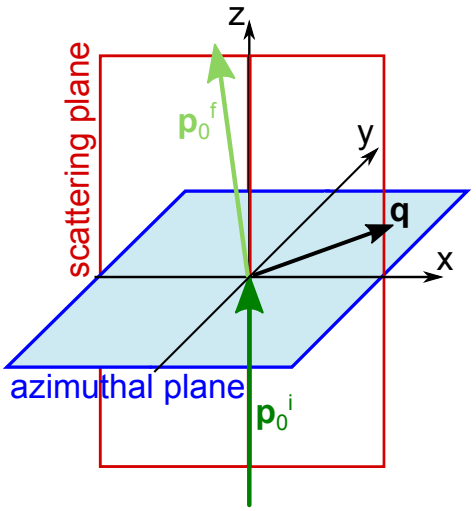

Figure 4.5: Azimuthal and scattering plane in a collision system. $\mathbf{p}_0^i$ and $\mathbf{p}_0^f$ are the initial and final projectile momenta and $\mathbf{q}$ is the momentum transfer.

4.4 The wiggle correction method

This chapter will introduce a novel analysis technique that is capable of restoring experimental information that has to be discarded due to the cyclotron motion of the electrons in the magnetic field.

In fig. 4.1 the cyclotron motion of the electrons is illustrated. At the position of the wiggles the radius of the cyclotron motion is zero, therefore no resolution of the transverse momentum can be obtained (eq. (4.8)). In order to achieve a reasonable resolution, data points in and around the wiggles are neglected in the analysis process. At certain longitudinal momenta all data points are removed, which can influence the measured cross sections, see section 4.4.3.

The general concept can be derived from fig. 4.6: in (a) the cross section as a function of the longitudinal and transverse momentum is shown with respect to the spectrometer axis, while in (b) the same is shown, but with respect to the projectile beam axis. This inclination is intrinsic to our setup, see section 3.1.1, and makes basically all parts in momentum space accessible. The symmetry with respect to the projectile beam axis allows the reconstruction of the neglected data points, which is explained in the following.

4.4.1 Principle of the wiggle correction method

The wiggle correction method requires an inclination between the spectrometer axis of the ReMi and the cylinder-symmetry axis of the collision process. As described in section 3.1.1, in the MOTReMi setup the inclination is 8°, which allows to apply this technique. As a result of this inclination, two coordinate systems emerge (see fig. 4.7 (a)): the projectile system (black) and the spectrometer system (blue). Here the two dimensional momentum space is illustrated for both coordinate systems.

The collision process is cylindrically symmetric, i.e. the cross section does not change for a certain momentum $\mathbf{p}$ (red) when rotating around p_z (dash-dotted magenta line) in the projectile system. Therefore at each point on the dash-dotted magenta circle the same cross section should be measured. However, a part of this circle might be

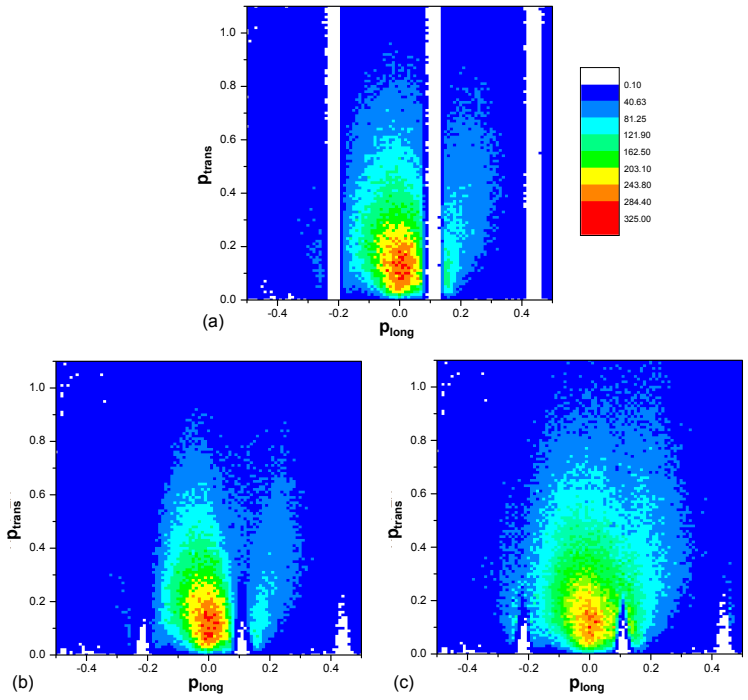

Figure 4.6: Momentum space with wiggles cut out unrotated (a), rotated (b) and corrected (c). Here single ionization of lithium by a 16 MeV Li^{2+} projectile is shown.

cut out, due to the above mentioned wiggle structure. The question is, what is the relative range of the angle ϕ (with $\tan(\phi) = p_y/p_x$) that is not cut out. The way to extract this number can be illustrated by projecting the circle in fig. 4.7 (a) on the p'_z axis. The full circle corresponds then to a *phi*-range of 180°. Due to the mirror symmetry with the p_x-p_z-plane it is sufficient to consider only the angle ϕ between 0° and 180°.

An example of this is shown in fig. 4.7 (b). Here one can already see how the cut out of the wiggles affects the analysis: parts of the rotated momentum are removed, which results in a smaller projection onto p_z in the spectrometer system (the green lines).

By looking more closely at this projected momentum circle (green lines in fig. 4.8) the contribution of missing counts can be calculated. In this example about $70° = 180° - (70° + 40°)$ are missing, therefore each measured point on the magenta circle has to be weighted by $w = 180/110$ to correst for the removed data points. Each momentum vector has its own weighting factor w that has to be calculated. The discussed example is only one possibility - specific cases are shown in fig. 4.9: in (a) the momentum is not affected by the wiggles - here the weighting factor is one, (b) illustrates the worst case, where the whole momentum circle is removed - here no data points exist, hence nothing can be weighted.

In 3D momentum space we look at $p_\perp = p_t = \sqrt{p_x^2 + p_y^2}$ over $p_\parallel = p_z$. The conversion to 3D is an integration of ϕ in the projectile system, which results in a rhomb-like structure of the wiggles. The calculated weighting factor illustrates this in fig. 4.10,

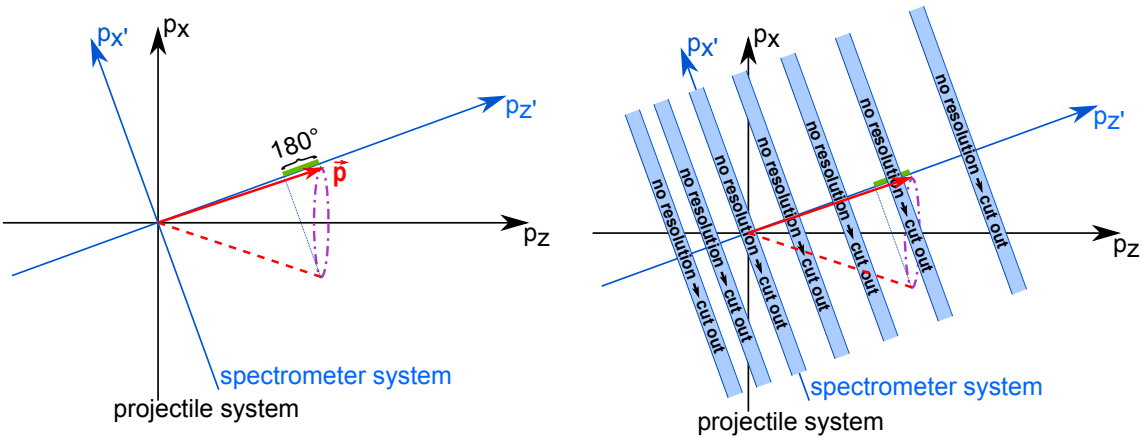

Figure 4.7: Illustration of the wiggle correction method in two dimensional momentum space. (a) shows the two coordinate systems and the projection of the rotated momentum vector, in (b) the removed wiggle parts are drawn.

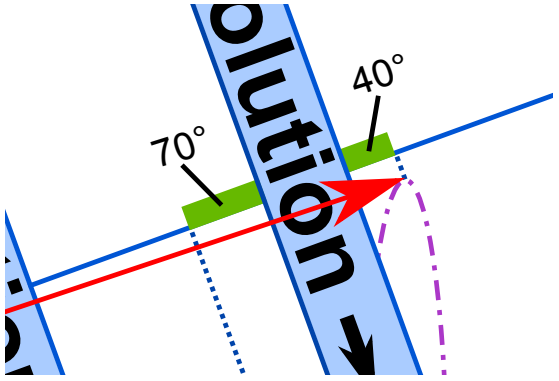

Figure 4.8: Zoom in the important part of fig. 4.7 (b). The whole projection is 180°, in this example 70° are missing, resulting in a weighting factor of $w = 180/110$.

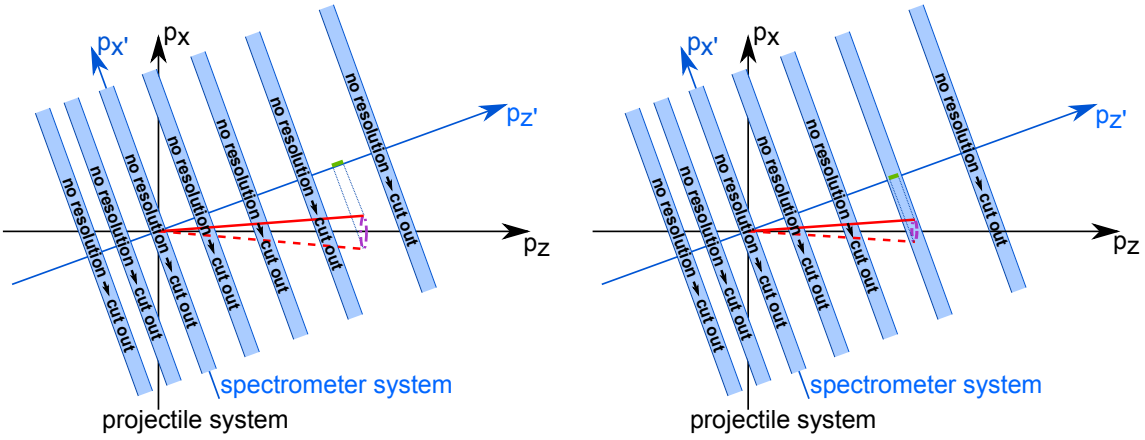

Figure 4.9: Specific cases of the wiggle correction. In (a) the weighting factor is one, in (b) no correction is possible.

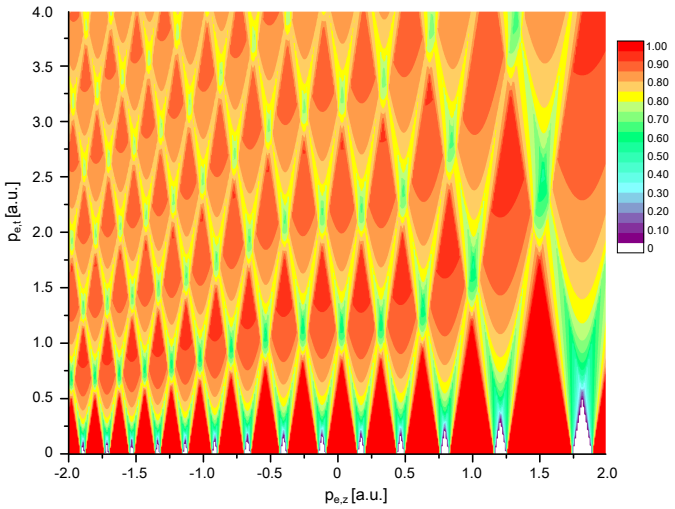

Figure 4.10: Calculated weighting factor. Here 1/w is plotted in 3D momentum space.

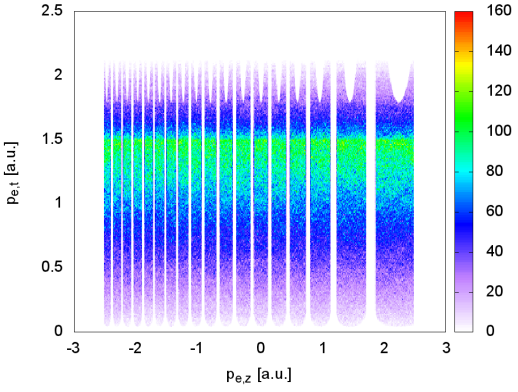

Figure 4.11: Uniform cuboid momentum distribution.

where $1/w$ is plotted in 3D momentum space. The white regions are the parts illustrated in fig. 4.9 (b), where no correction is possible, while the dark red regions correspond to fig. 4.9 (a), where the weighting factor is one.

4.4.2 Simulation of the wiggle correction

Before this correction method was applied to experimental data, simulations were employed to analyze its effect. At the beginning a uniform momentum distribution of p_x, p_y and p_z (a cuboid in momentum space) was chosen. In fig. 4.11 $p_{e,t} = \sqrt{p_x^2 + p_y^2}$ is plotted versus p_z. The wiggle parts are already removed, the structure at high $p_{e,t}$ is caused by the finite detector size. The increase of counts with $p_{e,t}$ emanates from solid angle considerations, while at high $p_{e,t}$ only the edges of the cuboid contribute causing the decrease beginning at about 1.5 a.u.. This implicates that in this simulation only the data up to $p_{e,t} = 1.5$ a.u. should be considered.

The next step is to rotate this uniform distribution by 8° to imitate the inclination of our spectrometer. The result can be seen in fig. 4.12 (a). As expected, rhomb-like structures can be observed. Applying the wiggle correction method gives fig. 4.12

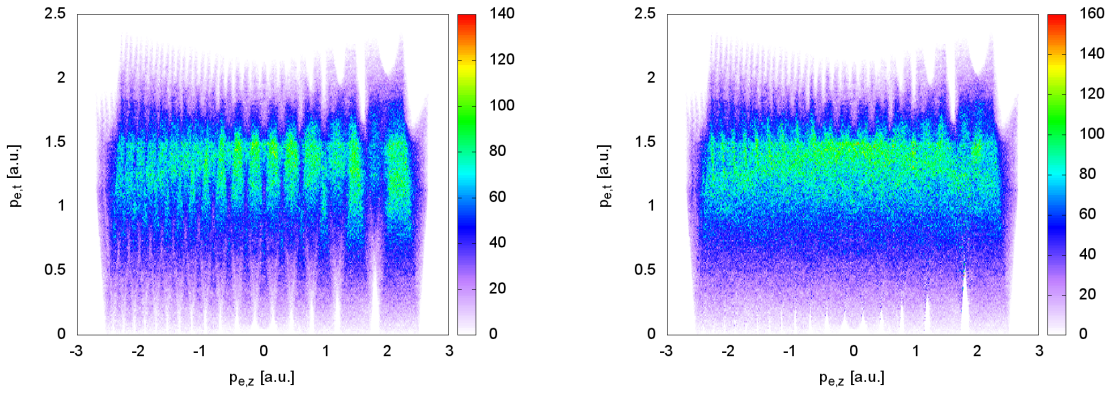

Figure 4.12: Momenta shown in fig. 4.11 rotated by 8° with (b) and without (a) wiggle correction.

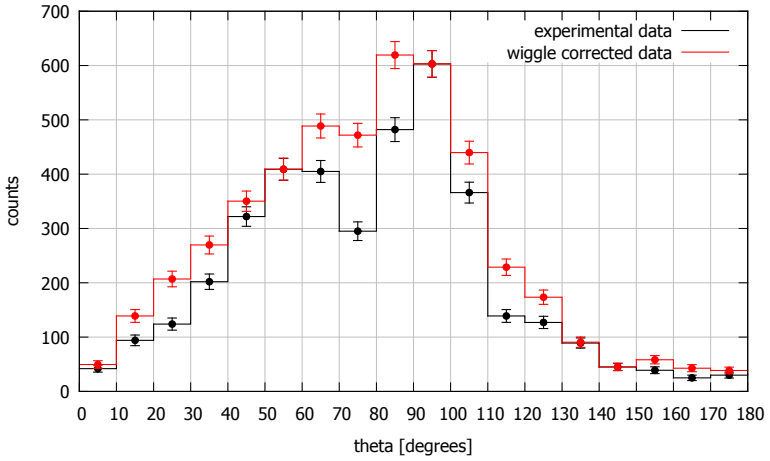

Figure 4.13: Comparison of FDCS for single ionization of lithium with and without correction in the scattering plane. The projectile was 24 MeV O^{8+}, the energy of the emitted electron is fixed at $E_e = 1.5\,\text{eV}$ and the momentum transfer at $q = 0.3\,\text{a.u.}$.

(b). The effect can clearly be seen, the structure below $p_{e,t} = 1.5\,\text{a.u.}$ is gone and a smooth distribution is visible. The only remnants are the triangles at the bottom, however, these are not correctable due to the effect illustrated in fig. 4.9 (b).

4.4.3 Experimental application

The wiggle correction has been implemented into the analysis code. In a first step the position of the wiggles with respect to the longitudinal momentum is calculated, which can easily be done as described in section 4.4.1. Then the correction factor is calculated for each data point separately.

In fig. 4.13 the effect of the wiggle correction is shown for a specific data set. Here the fully differential cross section (FDCS) of single ionization $O^{8+} + Li \rightarrow O^{8+} + Li^{+} + e^{-}$ are plotted, where lithium was initially in the ground state and a 2s electron was ionized. It can clearly be seen, that the recess at 75° is caused by a wiggle and hence weighted with with a higher correction factor. Although the final shape is not perfectly smooth, it is certainly much improved and the minimum has vanished.

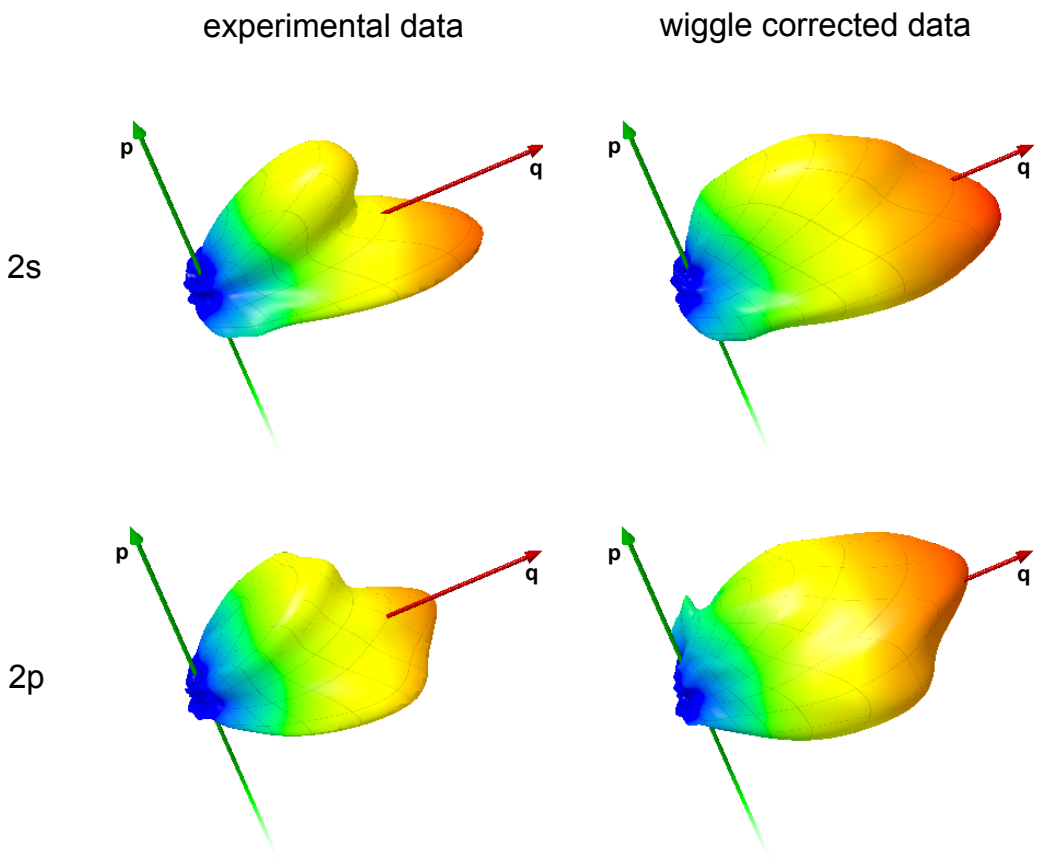

Figure 4.14: Comparison of FDCS for single ionization of lithium with and without correction. The projectile was 24 MeV O^{8+}, the energy of the emitted electron is fixed at $E_e = 1.5\,\text{eV}$ and the momentum transfer at $q = 0.3\,\text{a.u.}$. the electron emission angles are shown, with the projectile direction **p** and the momentum transfer **q**. $2s$ and $2p$ refer to the initial target state, i.e. whether the electron was emitted from the ground state or from an excited state.

The effect can also be seen in the 3D representation of the FDCS. In fig. 4.14 two examples are shown. The conditions are the same as in the previous figure, here the 2p ionization is depicted additionally. Again the vanishing of the recess can be observed, in 2p ionization the effect is even more drastic.

In conclusion, the wiggle correction method can be applied easily to experimental data and proves to remove to large extend artificial structures that in earlier experiments often limited the quality of experimental data.

5. Experimental Results

In this chapter the experimental results will be presented and discussed. The different processes single electron capture (SC), transfer ionization (TI) and single ionization (SI) will be addressed.

The total cross sections for these processes are very different. In the energy regime that was investigated in the framework of these thesis, the dominant channel resulting in the creation of recoil ions is single ionization. Experimentally, it represents a substantial challenge to extract SC and TI data and separate it from the 'background' caused by SI. This has been achieved in part by sophisticated switching techniques described in section 3.1.1. The obtained data are the first fully differential for capture from a lithium target. The present study of SI is a continuation and deepening of earlier results obtained with the same setup (Fischer et al., 2012; LaForge et al., 2013; Hubele et al., 2013). It is not only a systematic study of the earlier observed effects, but also new interpretation of initial state effects on the collision dynamics have been developed and tested with new data. In the following atomic units will be used, if not otherwise noted.

5.1 Single electron capture

As discussed in section 2.2.2, in SC one electron is transferred from the target to the projectile. In the system studied here, a 16 MeV O^{7+} projectile ($v_p = 6.3$ a.u.) captures an electron from a lithium target:

$$O^{7+} + Li \rightarrow O^{6+} + Li^{+} \tag{5.1}$$

In the final state there is only the charge changed projectile and the lithium ion, which were measured in coincidence. The electric field during this measurement was about 0.6 V/cm.

The projectile velocity influences the capture process significantly. At low v_p projectile and target form a quasi-molecule. In this region the cross section is determined by the distance of the corresponding energy levels from the projectile and the target, where closer energy levels lead to larger cross sections. For high v_p the cross

Shell	$E_{\mathrm{bind},O^{7+}}$ [eV]	ΔE_{bind} [a.u.]	$p_{r\parallel}$ [a.u.]
K	739	24.77	-7.08
L	171	3.90	-3.77
M	75	0.37	-3.21
N	41	-0.89	-3.01

Table 5.1: Different shells of O^{7+} with corresponding binding energies. $E_{\mathrm{bind},O^{7+}}$ are the binding energies of the O^{7+} shells, ΔE_{bind} includes the binding energy of the $1s$ electron in lithium and $p_{r\parallel}$ is the longitudinal momentum of the recoil ion (*NIST Atomic Spectra Database* 2013).

section increases when the projectile velocity v_p gets closer to the velocity of the bound electron v_e (Schöffler et al., 2013), a maximum being close to velocity matching ($v_p = v_e$). However, in our experiment the projectile velocity is larger than the electron velocities. The inner shell electron ($v_e \approx 2.2$ a.u.) is significantly faster than the outer shell electron ($v_e \approx 0.6$ a.u.) and therefore more likely to be captured by the projectile.

In SC measurements it is possible to determine the O^{7+} shells in which the electron is captured. According to eq. (2.25) the evaluation of the longitudinal momentum allows to obtain this information. Table 5.1 gives the expected values for the longitudinal momentum, where ΔE_{bind} includes the capture of an electron from Li($1s$), with an ionization energy of 65 eV (see table 3.1).

Capture into different shells of O^{7+} is shown in fig. 5.1. As listed in table 5.1 the resulting longitudinal recoil ion momentum is -3.8 a.u. for capture to the L-shell, it is -3.2 a.u. for capture to the M-shell and -3 a.u. for capture to the N-shell. The distribution of the N-shell is much broader – here also higher shells contribute, which cannot be resolved separately. K-shell capture cannot be seen in our data, as the cross section is quite small in comparison to other shells (Schöffler, 2006). Moreover, this transition requires small impact parameters, which results in large transverse momenta of the recoil ion, which are beyond the momentum acceptance of our spectrometer.

The transverse recoil ion momentum distribution for the capture in different shells are illustrated in fig. 5.2. In the past, such transverse momentum distributions of electron capture processes allowed to identify different mechanisms. Most prominently, this way it was possible to separate first (so-called 'kinematic capture') and second order ('Thomas capture') transfer mechanisms from hydrogen (Vogt et al., 1986) and helium targets (Horsdal-Pedersen et al., 1983; Fischer et al., 2006; Kim et al., 2012). Though in the present spectra also structures are observed, which seem to depend on the state to which the electron is transferred, the statistical significance is not sufficient, to perform a detailed study. However, the present results in combination with the data of transfer ionization represent a first step in understanding correlation and multiple scattering processes in charge transfer from few-electron atoms.

5.2 Transfer ionization

Transfer ionization (TI) is a combination of single ionization and single capture. The target looses two electrons, one is captured by the projectile and one is emitted to the

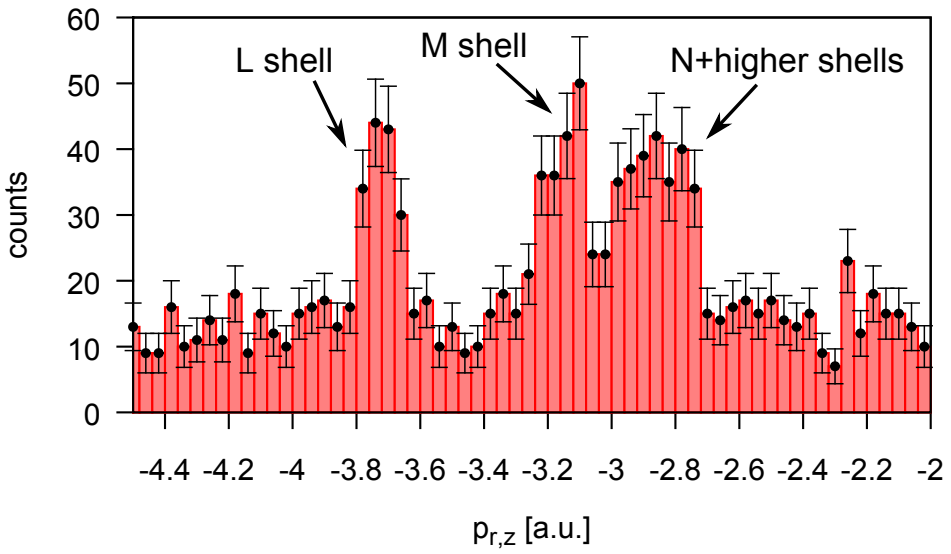

Figure 5.1: SDCS for single capture as a function of the longitudinal recoil ion momentum. The peaks correspond to electron capture into different shells according to table 5.1.

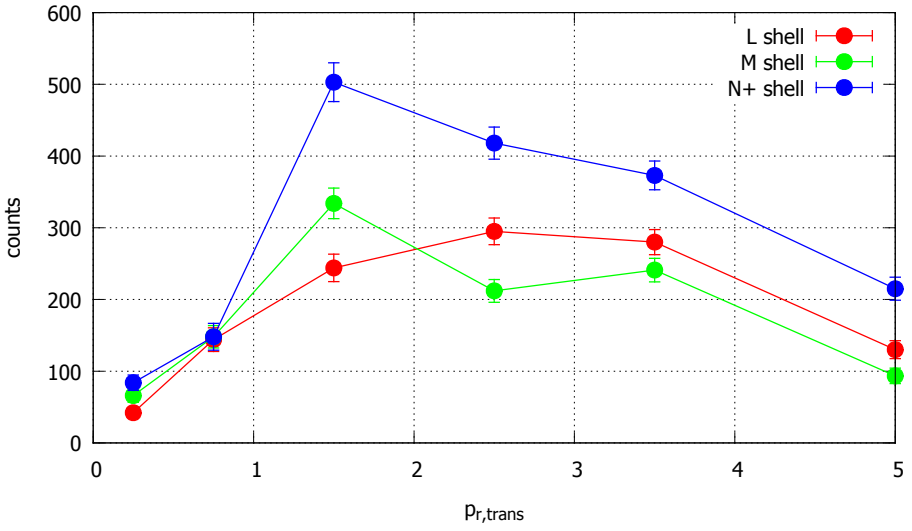

Figure 5.2: SDCS for single capture for different shells as a function of the transverse recoil ion momentum. The data points are cross normalized.

continuum. TI measurements are well suited for investigating electron correlations. As detailed in section 2.2.3, in the literature several mechanisms have been proposed and experimentally verified, some of them involving electronic correlation effects (Horsdal et al., 1986; Pálinkás et al., 1989), referred to as correlated TI, some of them not (Mergel et al., 1997; Schneider, 2012) (referred to as independent TI).

Most of the earlier works concentrated helium as a target (e.g. (Schneider, 2012; Schneider et al., 2013)). Though for helium the electronic correlation is rather strong, both correlated and independent TI have been investigated in two collision systems with different perturbation. While at $\eta = 1.1$ a.u. independent TI could be observed and reproduced theoretically, the collision system with $\eta = 0.5$ a.u. allowed to confirm a new TI process (electron-electron TI, (Voitkiv et al., 2008; Schulz et al., 2012)) besides the known correlated ones.

In the present work, a rather high perturbation was chosen with 16 MeV O^{7+} projectiles ($v_p = 6.3$ a.u., $\eta = 1.1$) to study the TI from a lithium target. The reaction equation is:

$$O^{7+} + Li \rightarrow O^{6+} + Li^{2+} + e^- \tag{5.2}$$

The relatively high perturbation was chosen essentially for two reasons: first, for lower perturbations the total cross section for TI is very low, and due to the overall lower target density achieved in the lithium MOT compared to a helium gas-jet the process would be essentially unobservable with the techniques available. Second, the same projectile was used to study TI from He ((Schneider et al., 2013; Schneider, 2012)). Hence, the cross sections can be compared and differences can be assigned to the target properties.

In the present experiment all the outgoing particles were detected in coincidence, i.e. the doubly ionized lithium ion, one free electron and a charge changed projectile. The electric and magnetic field were 0.6 V/cm and 6.5 G, respectively, resulting in a full longitudinal electron acceptance of about 0.8 a.u. and a transverse acceptance of 1 a.u..

In lithium the electron is captured most likely from the $1s$ state while the $2s$ (or $2p$) electron is ejected. Because these electrons are only weakly correlated and due to the large perturbation one might expect the independent TI process to be dominant. However, as the ionization potential of the $2s$ electron is only 5.4 eV, also shake-off can contribute significantly.

For this measurement the spectrometer voltage was switched as described in section 3.1.1, which resulted in a suppression of Li^+ background originating from single ionization. However, the switching reduced the resolution of the recoil ions. In SC the shells of O^{7+}, in which the electron is captured, could be resolved - this was not possible in TI (compare fig. 5.1 to fig. 5.3).

5.2.1 Results

In table 5.2 the binding energies of O^{7+} and the corresponding energy differences for transfer ionization are listed. As mentioned above, the different shells could not be distinguished in the experimental data (see fig. 5.3). Here only one broad peak is observed, whose main contribution is expected to be from the L-shell.

Shell	$E_{\text{bind},O^{7+}}$ [eV]	ΔE_{bind} [a.u.]
K	739	24.18
L	171	3.31
M	75	-0.22
N	41	-1.47

Table 5.2: Different shells of O^{7+} with corresponding binding energies. ΔE_{bind} includes the ionization potential to end in the $1s^1$ configuration of lithium (*NIST Atomic Spectra Database* 2013).

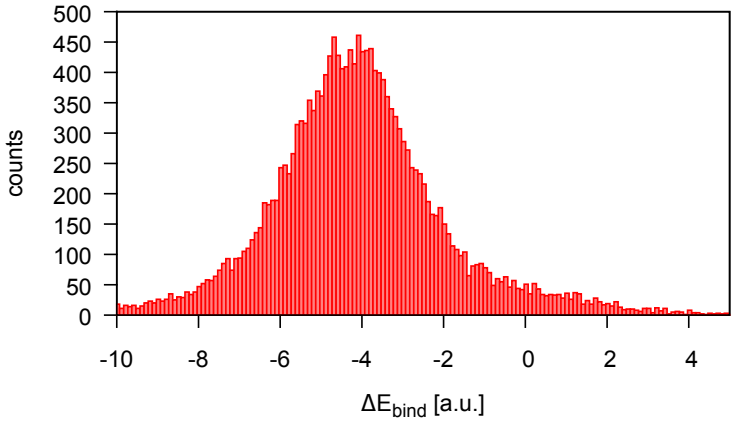

Figure 5.3: SDCS for transfer ionization as a function of the difference in binding energies (Q-value). Capture in different shells cannot be distinguished.

Comparison to transfer ionization with a helium target

In (Schneider, 2012; Schneider et al., 2013) a similar experiment was performed with a helium target. The projectile was also 16 MeV O^{7+} with the reaction equation:

$$O^{7+} + He \rightarrow O^{6+} + He^{2+} + e^- \tag{5.3}$$

At this relatively high perturbation of $\eta = 1.1$ a.u. the independent transfer ionization process is more likely than the correlated one. The electron emission characteristics are plotted in fig. 5.4 and compared to the present experiment.

In the scattering plane (a), the electrons are emitted in forward direction. In the graph the momentum transfer points in the upper half plane. At this high perturbation, the projectile drags the electrons into the forward direction (post collision interaction). The absence of perpendicular (Thomas TI) or backwards emission (eeTI) indicate the importance of the independent TI process. The differences between the helium and lithium target are rather small – at helium the electrons seem to be emitted at a slightly larger angle.

In the azimuthal plane (b), the electron emission differs strongly for the different targets. While the helium target TI shows a typical peak structure similar to single ionization with a pronounced peak in $\mathbf{q}$ direction and a small recoil peak, the electrons are emitted almost isotropically in lithium target TI. This is explained with the low ionization potential of the Li($2s$) electron. Usually the Li($1s$) electron is captured, which leaves the $2s$ electron for ionization. The ionization potential for

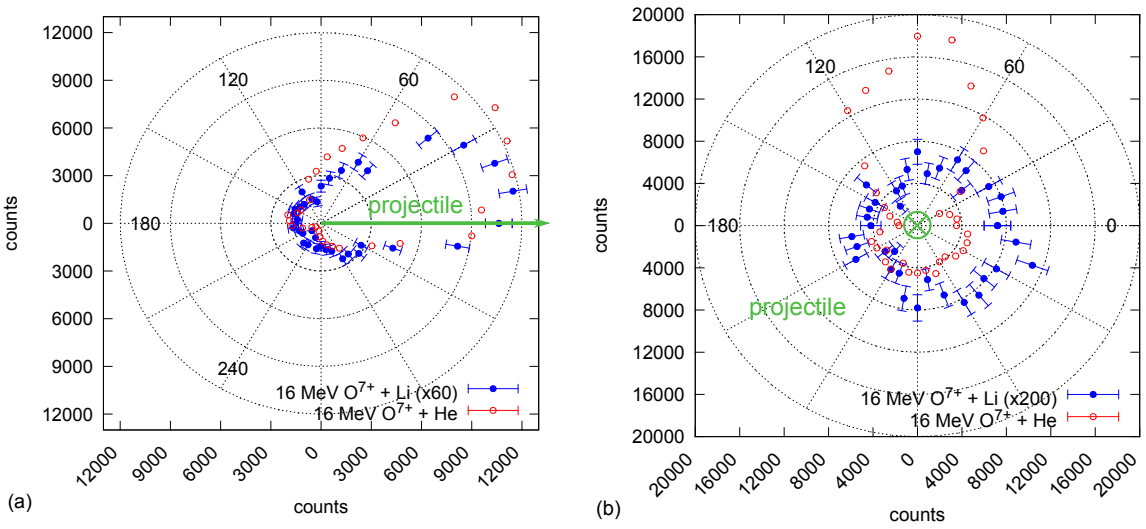

Figure 5.4: Comparison of the DDCS for transfer ionization in the scattering (a) and azimuthal (b) plane for a helium (red open circles) and a lithium (blue filled circles) target. The electron energy was fixed at 8 eV in the helium and 10 eV in the lithium measurement, the transverse momentum transfer was integrated.

the $2s$ electron is only 5.4 eV, while in the helium target the electrons are bound with an average energy of 40 eV. At this low ionization potential, a shake-off process, which is independent of the momentum transfer direction, is much more likely than in the helium case.

Comparison to theory

In independent TI the capture and the ionization process can be treated separately. We used CDW-EIS for calculating the ionization process and CDW for the capture process (Voitkiv, 2013).

The results for the scattering plane are shown in fig. 5.5. The binary peak is reproduced quite well, while theory seems to overestimate the recoil peak. The two narrow side peaks cannot be resolved in the experiment, so we convoluted the calculation with a Gaussian representing a resolution of about $\pm 15°$, which is plotted as a green line. The overall agreement is quite good, besides the overestimated recoil peak and a node at about 300°, which is not observed in the data.

The same theoretical calculation was performed in the azimuthal plane (fig. 5.6). Neither theory nor experimental data inhibit much structure, hence indicating a shake-off process. However, overall qualitative agreement in the azimuthal plane can be observed.

In conclusion, this measurement clearly showed the difference of the electron correlations in helium and lithium. The isotropic emission in the azimuthal plane with lithium in contrast to the SI emission pattern with helium is significant. The similarity to theory is overall satisfying.

5.3 Single ionization

In SI the projectile interacts with the target ion such that one electron is emitted to the continuum, resulting in three free particles in the final state. In the following

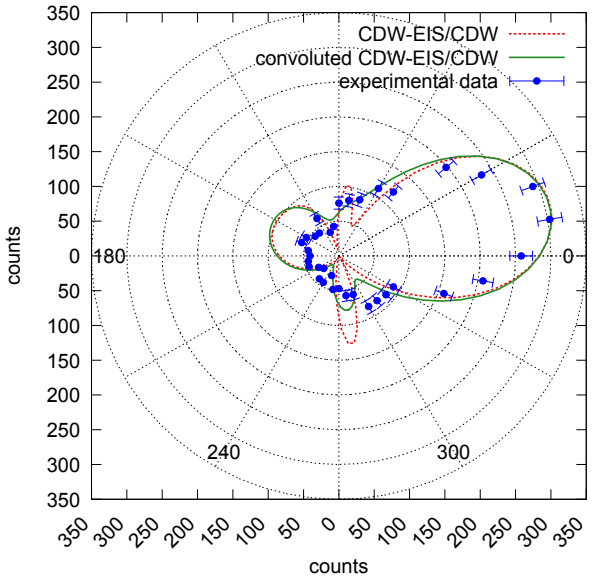

Figure 5.5: Theoretical and experimental data for transfer ionization in the scattering plane. Theory used $E_e = 8\,\text{eV}$ and $q_t = 3\,\text{a.u.}$. The experimental data is the SDCS ($d\sigma/d\Omega$), the theoretical values correspond to average of the energy and momentum transfer distributions. The green line is a convolution with a Gaussian to simulate the resolution of the experiment.

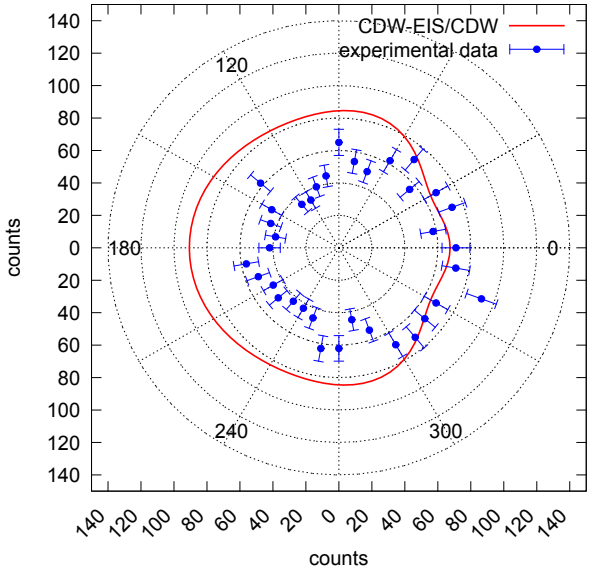

Figure 5.6: Theoretical and experimental data for transfer ionization in the azimuthal plane. Theory used $E_e = 8\,\text{eV}$ and $q_t = 3\,\text{a.u.}$. The experimental data is the SDCS ($d\sigma/d\Omega$), the theoretical values correspond to average of the energy and momentum transfer distributions.

data of two different collisions systems will be presented: 24 MeV O^{8+} ($v_p = 7.9$ a.u.) and 16 MeV Li^{2+} ($v_p = 9.8$ a.u.) projectiles corresponding to perturbations $\eta(O^{8+}) = 1.0$ a.u. and $\eta(Li^{2+}) = 0.2$ a.u. The reaction equation is:

$$O^{8+} + Li \rightarrow O^{8+} + Li^{+} + e^{-} \tag{5.4}$$

We detect lithium ions and electrons in coincidence. In the measurement at high perturbation the electric and magnetic field were 0.6 V/cm and 7.6 G, respectively, resulting in a longitudinal electron acceptance of about 0.8 a.u. and a transverse acceptance of about 1.2 a.u. In the lithium measurement the electric and magnetic field were 1.4 V/cm and 11.6 G, respectively, with a full longitudinal and transverse electron acceptance of about 1.2 a.u. and 1.9 a.u., respectively.

With only one electron in the final state this process is fairly simple. For helium targets it has been intensively investigated (Schulz et al., 2003; Moshammer et al., 2001; Moshammer et al., 1994). Contrary to helium, where both electrons populate the $1s$ state, in lithium the $1s$ or the $2s$ electron can be emitted to the continuum. The ionization potential differs, as the Li($1s$) electron is bound with 65.4 eV and the Li($2s$) electron with only 5.4 eV, which has implications on the collision process itself. The removal of a $1s$ or $2s$ electron can be distinguished in an experiment due to the different Q-values (cf. eq. (2.19)).

Moreover, the MOTReMi setup allows also to measure ionization of excited lithium targets. During the MOT cooling cycle the $2p$ state is populated with up to about 20% of the electrons are in the 2p state (see (Hubele, 2013)). Cross sections for the ionization of a $2p$ electron can be obtained by subtracting spectra with the laser beam switched on and off.

In the following, the ionization of $2s$, $2p$ and $1s$ electrons will be discussed.

5.3.1 $2s$ ionization

Ionization of the $2s$ electron was already investigated in (LaForge et al., 2013; Hubele et al., 2013) for a 24 MeV O^{8+} ($\eta_{O^{8+}} = 1.0$ a.u.) and 6 MeV H^{+} ($\eta_{H^{+}} = 0.1$ a.u.) projectile. The main focus on this chapter will be on a 16 MeV Li^{2+} projectile with an perturbation parameter of $\eta_{Li^{2+}} = 0.2$ a.u., which is a rather low perturbation close to the H^{+} case.

In fig. 5.7 the fully differential cross section is shown. The green and red arrows indicate the projectile beam and momentum transfer direction, respectively. The shape is similar to cross sections for helium (see e.g. fig. 2.7) with the main peak in **q** direction ('binary' peak) and a smaller peak in the opposite direction ('recoil' peak). The distribution has a smaller width than for helium, as the Compton profile, i.e. the mean electron velocity in the bound state is smaller. The narrower recoil peak is due to the small binding energy of the $2s$ electron, which is only $I_p = 5.4$ eV in comparison to $I_p = 24.6$ eV (*NIST Atomic Spectra Database* 2013) for ground-state ionization of helium. Hence a back-scattering at the target core is less probable as for higher binding energies.

The effect of the coherence of the projectile was discussed in section 2.1.3. Several publications (Schneider et al., 2013; Egodapitiya et al., 2011) were investigating this issue, triggered by a rather long-standing puzzle:

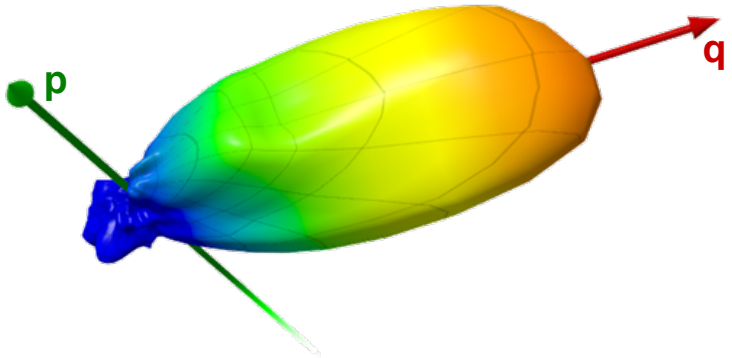

Figure 5.7: FDCS for $2s$ ionization of lithium. The projectile was 16 MeV Li^{2+}, at $E_e = 1\,\text{eV}$ and $q = 0.5\,\text{a.u.}$

In (Schulz et al., 2003) discrepancies between the measured and calculated cross section in 1.2 GeV C^{6+} were reported. While numerous quantum-mechanical calculations could not resolve these discrepancies (Madison et al., 2002; Madison et al., 2003) or only achieve qualitative agreement (Colgan et al., 2011), the rather simple approach, a convolution of the first Born approximation with classical elastic scattering (Schulz et al., 2007), significantly improved the agreement with the experimental data. The main difference between these calculation is the treatment of the nucleus-nucleus interaction: in the quantum mechanical calculations the projectiles are fully coherent, i.e. interference is possible for the projectile wave that is diffracted by the target atom. In the classical description the cross section is just convoluted over the elastic nucleus-nucleus scattering, thereby neglecting interference effects.

In fig. 5.8 the measured cross sections for 1.2 GeV C^{6+} and 3 MeV H^+ on helium are shown in the azimuthal plane (from (Wang et al., 2012)). The two collision systems have the same perturbation parameter and hence should show essentially the same angular distributions. This is indeed the case in the scattering plane (not shown here), where also theory agrees with both data sets. However, in the azimuthal plane the experimental data disagrees significantly. While the two peaks ('binary' and 'recoil' peak) are clearly separated in the H^+ collision system, the minimum is smeared out for the C^{6+} projectile (see fig. 5.8). The same general behavior can be seen for the calculations: the quantum mechanical theories (fully coherent description) agree qualitatively with H^+, the FBA with elastic scattering (incoherent description) with the C^{6+} data. This indicates a difference between the projectiles, which was found to be the transverse coherence length of the projectile, being $l_x^{C^{6+}} = 10^{-3}\,\text{a.u.}$ and $l_x^{H^+} = 3\,\text{a.u.}$ However, why can these discrepancies only be seen in the azimuthal plane?

To answer that question, it has to be clear which channels actually interfere. In (Sarkadi, 2010) an answer has been proposed: one channel is the electron-projectile interaction (a first order process), while a second one is the additional projectile - target core (or nucleus-nucleus) interaction, a second order process. This also explains why the interference can only be observed in the azimuthal plane. The scattering plane is dominated by the first channel, as the longitudinal momentum transfer is determined by kinematics. In contrast, the azimuthal plane is more likely to show higher order processes, as the departure from the q-direction is only possible by higher order processes (neglecting the electron momentum in the bound state),

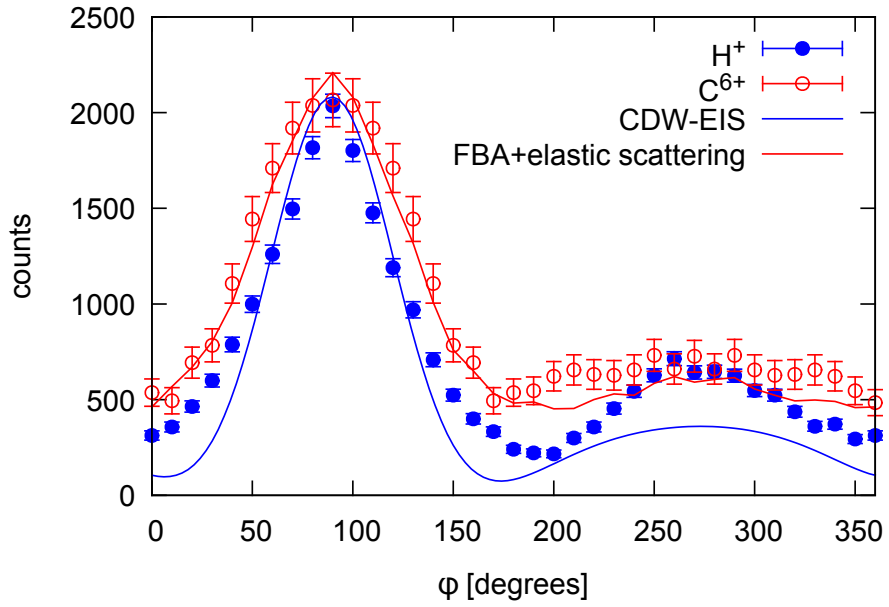

Figure 5.8: Coherence effects in the azimuthal plane. The FDCS for single ionization of 1.2 GeV C^{6+} and 3 MeV H^+ on helium collisions are plotted at $E_e = 6.5$ eV and $q = 0.75$ a.u., as well as two theories: CDW-EIS and a first Born approximation convolution with elastic scattering. (Wang et al., 2012)

which are dominated by the nucleus-nucleus interaction.

The comparison of the 16 MeV Li^{2+} and the 24 MeV O^{8+} on lithium collisions is not straightforward. The significantly lower ionization potential of the $2s$ electron in lithium compared to the $1s$ electron in helium shrinks the recoil peak. Hence it is much more difficult to see a minimum between the binary and the recoil peak. In fig. 5.9 (a) such an experimental cross section is shown. The recoil peak is very small, a statistically significant minimum cannot be observed. However, as mentioned above, the interference should be more pronounced for smaller impact parameters. This can be done by using data with core-hole creation (see section 5.3.3), which is shown in fig. 5.9 (b). Here the recoil peak is larger and a minimum separating the peaks can be observed. Unfortunately the statistical quality is limited in this case. Moreover, as will be discussed in section 5.3.3, several higher order mechanisms might contribute to this spectrum, which makes drawing a conclusion on coherence effects very difficult.

However, another hint about the influence of coherence effects can be obtained by the consideration of symmetries. As can be seen from eq. (2.41), a general property of the first Born approximation is the symmetry of the cross sections with respect to $\mathbf{q}$. Any deviation from this symmetry has to be assigned to higher order effects. Because in the here discussed situations the momentum transfer is close to be perpendicular to the projectile beam direction, such asymmetries can easily be investigated by comparing spectra for the azimuthal and the scattering plane. In fig. 5.10 the relative angle between the electron and the recoil ion is plotted against the momentum transfer in the scattering and the azimuthal plane for the Li^{2+} on lithium collision system. A distinct difference can be seen concerning the relative angle. In the scattering plane $\theta_{\mathrm{rel}} = 180°$, i.e. electron and recoil ion are emitted back to back. In the azimuthal plane this is only the case for small momentum transfers. At

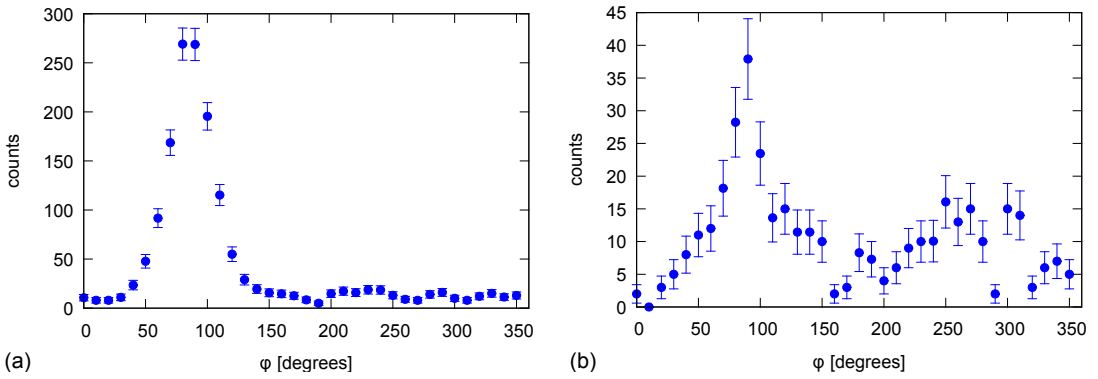

Figure 5.9: Cut of the FDCS in the azimuthal plane for pure $2s$ ionization (a) and for $2s$ ionization with core-hole creation (b). The collision system is 16 MeV Li^{2+}, the energy was fixed at $E_e = 2$ eV and the momentum transfer at $q = 0.7$ a.u.

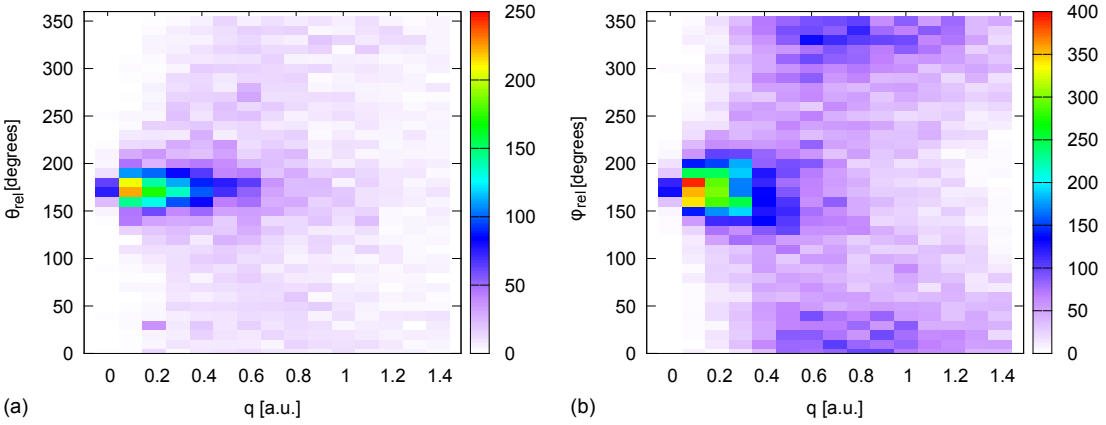

Figure 5.10: Relative angle over momentum transfer for single ionization in the scattering (a) and azimuthal plane (b). The collision system is 16 MeV Li^{2+} on lithium.

about $q = 0.6$ a.u. they are emitted in the same direction. These two cases are separated by a minimum, which can be caused by an interference effect. In O^{8+} on lithium collisions a similar effect can be observed (fig. 5.11). Here the minima are less pronounced, however, this can be explained by the higher perturbation in this collision system, which tends to wash out structures.

As pointed out before, any difference between the spectra in scattering and azimuthal plane can be assigned to higher order contributions. Though it is not surprising to see a rather strong asymmetry with respect to **q** for the high perturbation (Fischer et al., 2003a), for the Li^{2+} collisions one would, however, expect higher order contributions being rather insignificant. Though this statement is not proved by theoretical cross sections in this thesis, it still seems to be justified due to earlier calculated cross sections for the ionization of helium (Schulz et al., 2003; Wang et al., 2012). Similar to the conclusion drawn in (Wang et al., 2012) the asymmetry might be explained by the finite coherence length of the projectile wave, which was in the present case about 0.5 a.u. However, it should be noted that this interpretation still needs to be confirmed theoretically, but a fully quantum-mechanical calculation accounting for the coherence length is not available to date.

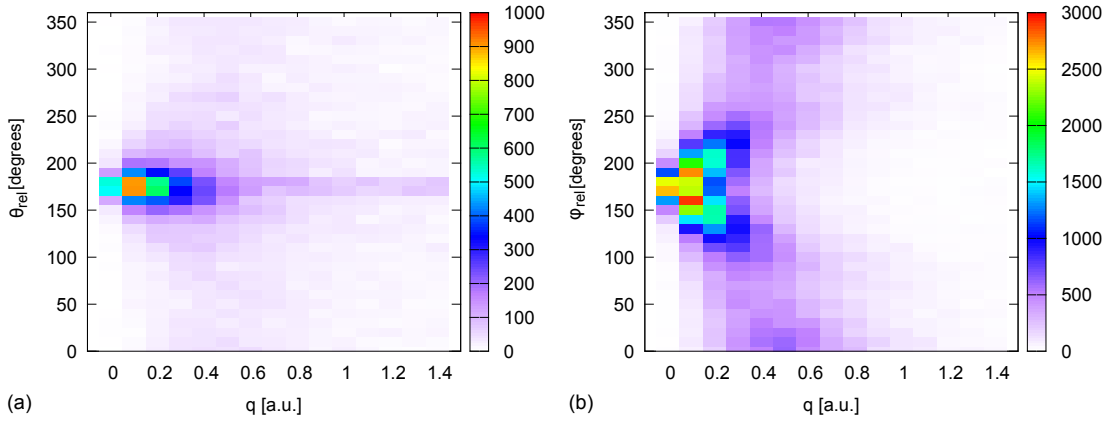

Figure 5.11: Relative angle over momentum transfer for single ionization in the scattering (a) and azimuthal plane (b). The collision system is 24 MeV O^{8+} on lithium.

In Hubele et al., 2013 a rather special feature was reported for $2s$ ionization of lithium by 24 MeV O^{8+}. In the azimuthal plane two side maxima were observed (see fig. 5.12 (a)) for low energies and high momentum transfers. This structure is non-existent for $2p$ ionization nor for $1s$ ionization of helium, and it is traced back to the nodal structure of the radial part of the wave function for the $2s$ state of lithium. As the inner maximum contains only a small part of the total flux, it can only have a significant influence for small impact parameters. This was confirmed by theoretical calculations, which only reproduced the triple peak structure, when the nucleus-nucleus interaction was included. The impact parameter is small for high momentum transfer between the two nuclei, which is the case for high momentum transfer and low electron energies, herewith explaining the chosen values $q = 1.0$ a.u. and $E_e = 2$ eV.

For the 16 MeV Li^{2+} projectile this structure cannot be observed (see fig. 5.12 (b)). Although some of the data points could be interpreted as separate peaks, the shape is by far not as pronounced as for the O^{8+} projectile. Though we do not have an intuitive explanation for the much weaker triple peak structure for the low perturbation, it shows very clear, that the collision dynamics strongly depends on both the target initial state and on higher order effects.

5.3.2 $2p$ ionization

The laser-cooling of the MOT allows to investigate the ionization of the excited target. Moreover, due to the combination of the Zeeman splitting in the ReMi magnetic field and the red-detuning of the laser light, the electrons predominantly populate only one magnetic sub-level, resulting in the polarization of the target and orientational dichroism.

Orientational dichroism is the breakdown of symmetry due to target polarization. When the initial state is spherically symmetric, only the projectile beam direction **p** and the momentum transfer **q** define the angular emission characteristics, resulting in a symmetry with respect to the **qp**-plane (i.e. scattering plane).

For a polarized target this symmetry is broken, as the initial state is not spherically symmetric anymore. This has already been investigated in electron-impact ionization of polarized sodium atoms (Dorn et al., 1998). There, the target atoms were

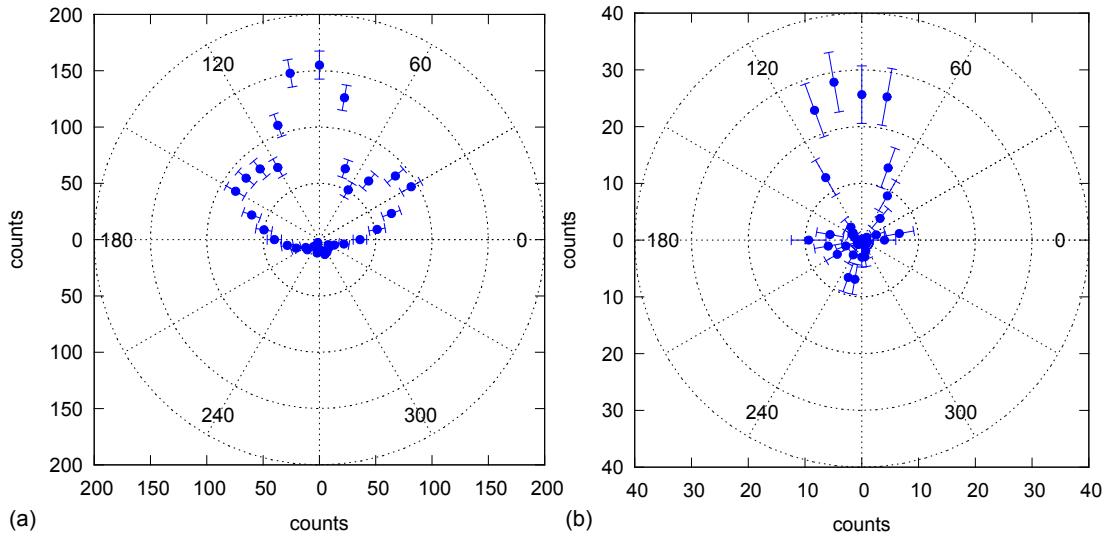

Figure 5.12: Cut of the FDCS for single ionization in the azimuthal plane. (a) shows the 24 MeV O^{8+} on lithium collision system at $q = 1.0$ a.u. and $E_e = 2$ eV, (b) shows the 16 MeV Li^{2+} collision system at $q = 1.2$ a.u. and $E_e = 2$ eV.

excited by left- and right-hand circularly polarized laser beams into the magnetic sub-levels $m_F = -3$ and $m_F = +3$ of the $^2P_{3/2}$ state. The emission angle of the electron showed a strong dependence on the initial magnetic sub-state.

In the MOTReMi setup about 20% of the electrons populate the $^2P_{3/2}$ state due to the cooling transition of the MOT. The homogeneous magnetic field of the ReMi leads to a Zeeman splitting of the $^2P_{3/2}$ state. The red-shifted cooling laser is then predominantly resonant to the $^2S_{1/2}$ to $^2P_{3/2}$ ($m_j = \pm 3/2$ or $m_l = \pm 1$) transition. The sign depends on the direction of the homogeneous magnetic field, in the O^{8+} measurement it was the $m_l = -1$, for Li^{2+} projectiles the $m_l = +1$ state. In our experiment, the degree of polarization is not 100%, i.e. the $m_l = 0$ state is also populated, however, the population in one magnetic sub-level is almost 90% (Hubele, 2013). It needs to be mentioned that due to the fine structure of lithium m_l is not a good quantum number at the present magnetic fields, i.e. m_l states mix with m_s to j and m_j (see also fig. 3.10). However, it can be seen that the four lowest lying hyperfine states have an $m_l = -1$ contribution of more than 90%.

The resulting fully differential cross sections for both collision systems are shown in fig. 5.13. A clear shift of the peaks from the q-direction can be seen. The direction of the shift is given by the magnetic field direction, which was turned between the measurements, resulting in two opposite shifts. In (b) the distribution is broader, which is due to the larger perturbation of this collision system.

An explanation of this effect can be given by considering the motion of the bound electrons. For a magnetic quantum number $m \neq 0$ a current density is assigned to the electrons:

$$\mathbf{j} = \frac{\hbar}{2m_e i}(\Psi^* \nabla \Psi - \Psi \nabla \Psi^*) \tag{5.5}$$

Classically, this can be understood as an initial velocity of an electron in radial direction in the donut-shaped $2p$ orbital fig. 5.17. This directed velocity of the bound electron influences the emission angle, resulting in the observed shift. When the magnetic field direction is turned, the sign of the lowest magnetic quantum

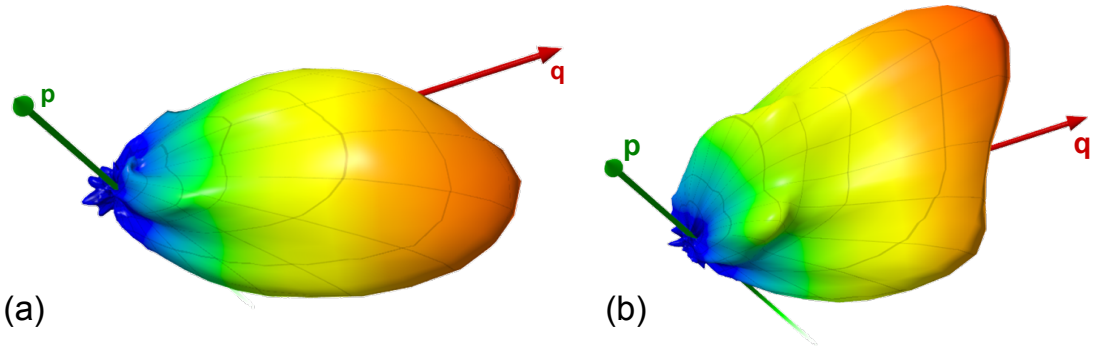

Figure 5.13: The FDCS show an orientational dichroism in both collision systems. Ionization of the $2p$ electron in lithium by 16 MeV Li^{2+} at $q = 0.5$ a.u. and $E_e = 1$ eV (a) and by 24 MeV O^{8+} at $q = 0.3$ a.u. and $E_e = 1.5$ eV (b) projectile.

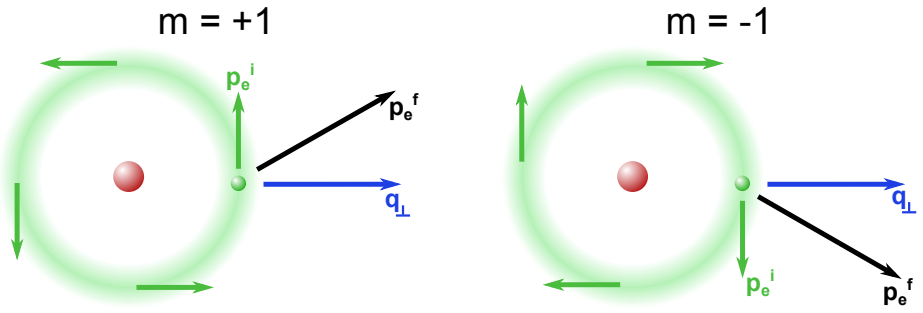

Figure 5.14: Illustration of the orientational dichroism in the azimuthal plane. The initial electron momentum $\mathbf{p}_e^i$ influences its emission direction $\mathbf{p}_e^f$ at the same transverse momentum transfer $\mathbf{q}_\perp$. Hence the sign of the populated magnetic quantum number m changes the orientation of the dichroism.

number changes. Thus, the direction of the current density is reversed and the shift of the electron emission angle is, too. This asymmetry is only observed in the azimuthal plane, which is the plane perpendicular to the projectile momentum. The momentum transfer vector is almost parallel to this plane ($\mathbf{q}_\perp \gg \mathbf{q}_\parallel$), therefore we can restrict this problem to two dimensions. In fig. 5.14 an illustration of this effect is shown in the azimuthal plane.

Dependence of the orientational dichroism to the momentum transfer

The direction of the angular shift due to orientational dichroism also depends on the magnitude of the momentum transfer. In fig. 5.15 the electron emission angle in the azimuthal plane for the Li^{2+} projectile is shown for an electron energy of $E_e = 2$ eV and three different momentum transfers. The coordinate system is chosen in such a way that the momentum transfer points in 90° direction. While at $q = 0.5$ a.u. the peak is shifted to smaller angles, the distribution for $q = 0.8$ a.u. is shifted to higher angles with a side-peak at smaller angles. At $q = 0.7$ a.u. a double peak structure can be observed. The theoretical calculations (Voitkiv, 2013) qualitatively agree with the experimental data. The change of emission direction as well as the double peak structures are well reproduced.

This dependence of the dichroism on the momentum transfer can be explained in the same classical picture as we did for the m-dependence. When the final electron energy is fixed (like in our case at $E_e^f = 2$ eV), the magnitude of the transverse

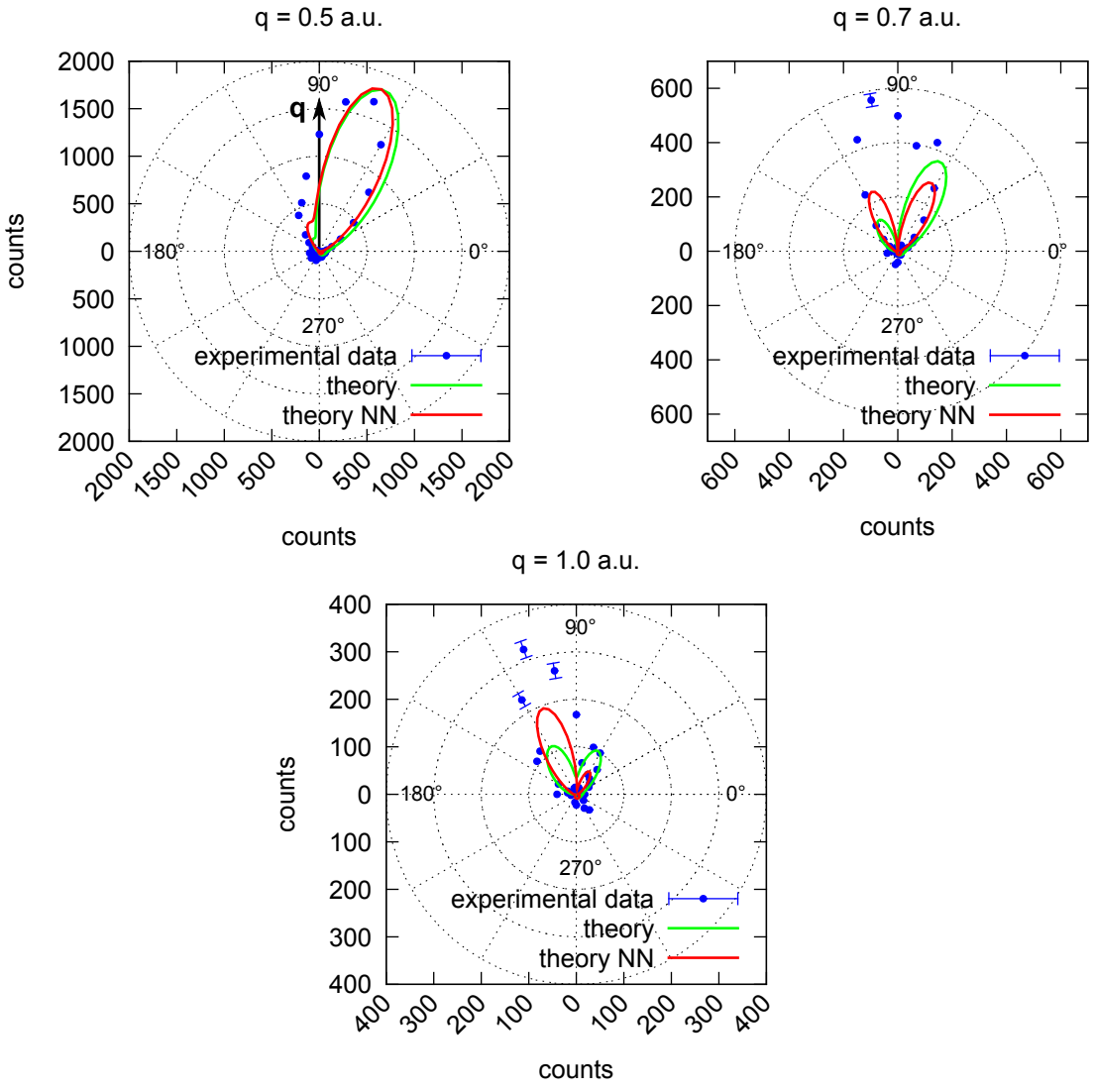

Figure 5.15: FDCS for $2p$ ionization for different momentum transfers. The electron energy was fixed at $E_e = 2\,\text{eV}$. The theories are CDW-EIS calculations with and without nucleus-nucleus (NN) interaction and were normalized to the experimental data at $q = 0.4\,\text{a.u.}$ (see fig. 7.1).

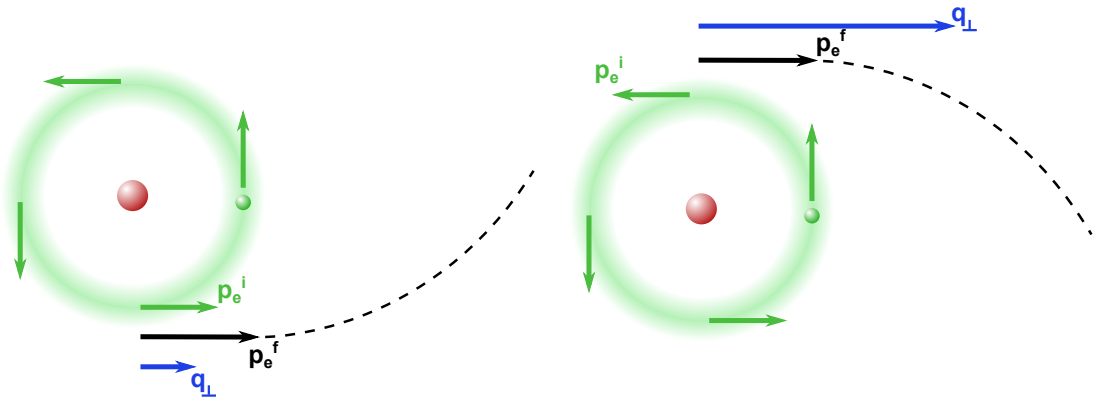

Figure 5.16: Illustration of the orientational dichroism in the azimuthal plane. The length of the transverse momentum transfer $\mathbf{q}_\perp$ chooses the angle between $\mathbf{q}_\perp$ and the initial electron momentum $\mathbf{p}_e^i$. After the collision, the electron trajectory is bend by the Coulomb interaction with the target core.

momentum transfer determines the emission direction of the electron relative to the atom. Energy conservation gives:

$$\frac{(\mathbf{p}_e^i + \mathbf{q}_\perp)^2}{2} - I_p = E_e^f \tag{5.6}$$

with the initial electron momentum $\mathbf{p}_e^i$, the transverse momentum transfer $\mathbf{q}_\perp$ and the ionization potential I_p. Estimating the initial kinetic energy of the electron with the virial theorem (i.e. assuming a $1/r$ potential) gives $E_{\text{kin}} = I_p$ and the scalar product introduces the angle θ between $\mathbf{p}_e^i$ and $\mathbf{q}_\perp$, resulting in

$$\frac{\mathbf{q}_\perp{}^2}{2} + \sqrt{2I_p} \cdot \cos(\theta) = E_e^f \tag{5.7}$$

This equation explains qualitatively the observation: for a certain magnitude of the transverse momentum transfer the emission angle θ can be determined, thus defining the direction of the electron momentum with respect to the momentum transfer after the collision. An illustration of two special cases is shown in fig. 5.16. In (a) $q_\perp$ is smaller than the final electron momentum p_e^f, therefore the initial electron momentum has to point in the same direction. In (b) the momentum transfer is larger than the final electron momentum, hence the initial electron momentum has to point in the opposite direction. Momentum transfers with a length in between these extreme values are related to a initial electron momenta at the angle θ given by eq. (5.7). This alone does not explain the asymmetry: for very small and very large momentum transfers the electron is emitted in $\mathbf{q}$-direction (as shown in fig. 5.16), which is evidently not observed in the experimental data.

However, when the interaction between the electron and the target core is considered (dashed lines in fig. 5.16), the reason for the asymmetry becomes clear. The Coulomb force bends the trajectory towards the atomic core, resulting in different emission angles for the electrons, whose momenta pointed in the same direction after the collision.

Quantum mechanically, the symmetry can be explained by an interference of different partial waves. Starting with a polarized $2p$ state ((l,m)=(1,1) or (1,-1)), the dominating dipole transition can result in a $1s$ (0,0) or different 3d states ((2,0)(2,±1)(2,±2)).

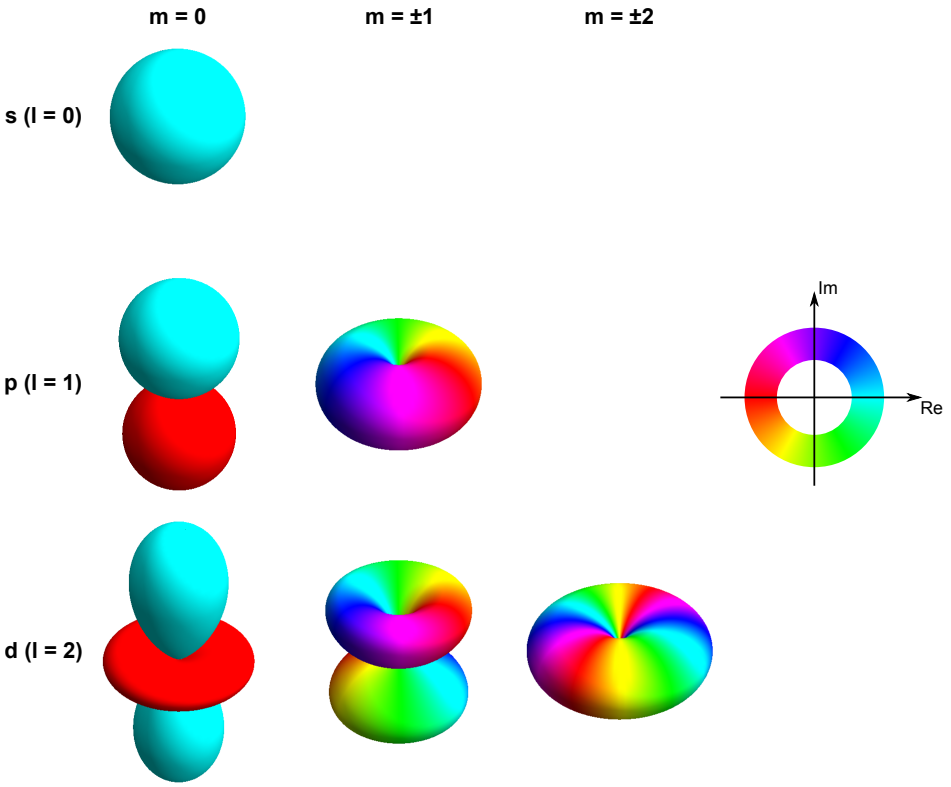

Figure 5.17: Spherical harmonics and phase information for the s, p and d orbital. The phase is plus for the light blue in (l,m)=(0,0) and minus for red. The initial state is (1,±1), a dipole transition can lead to all s and d orbitals. The relative phase shift determines the interference pattern.

The corresponding orbitals are shown in fig. 5.17. The interference is supposed to be between (0,0) and (2,0) or (2,±2), as a transition to (2,±1) would require a $\Delta m = 0$ transition, i.e. a momentum transfer parallel to the beam direction (or quantization axis). In general, the electron emission pattern can be interpreted as an interference of these partial waves (with different amplitudes and phases). The dichroism is due to an asymmetric contribution of positive and negative m_l's.

In order to systematically study the dichroism, the asymmetry parameter A was introduced:

$$A = \frac{N_{0°-90°} - N_{90°-180°}}{N_{0°-90°} + N_{90°-180°}} \tag{5.8}$$

where $N_{0°-90°}$ and $N_{90°-180°}$ is the sum over all events emitted to angles between 0° and 90° or 90° and 180°, respectively. The dependence of this asymmetry parameter on the momentum transfer at $E_e^f = 2\,\text{eV}$ is shown in fig. 5.18, as well as theoretical calculations with and without nucleus-nucleus interaction. A sinusoidal behavior can be observed. The data points larger than $q = 0.9\,\text{a.u.}$ seem to be far off, however, this can be caused by the rather poor statistics at high momentum transfers. The polar plots for each data point and the corresponding theory are shown in the appendix (section 7.2). Theory and experimental data agree qualitatively, besides overestimating the magnitude of the asymmetry. As already mentioned earlier, the calculation with nucleus-nucleus interaction agrees better with the experimental data, the zero-point differs only slightly.

For higher electron energies the same behavior can be observed (see fig. 5.19). The

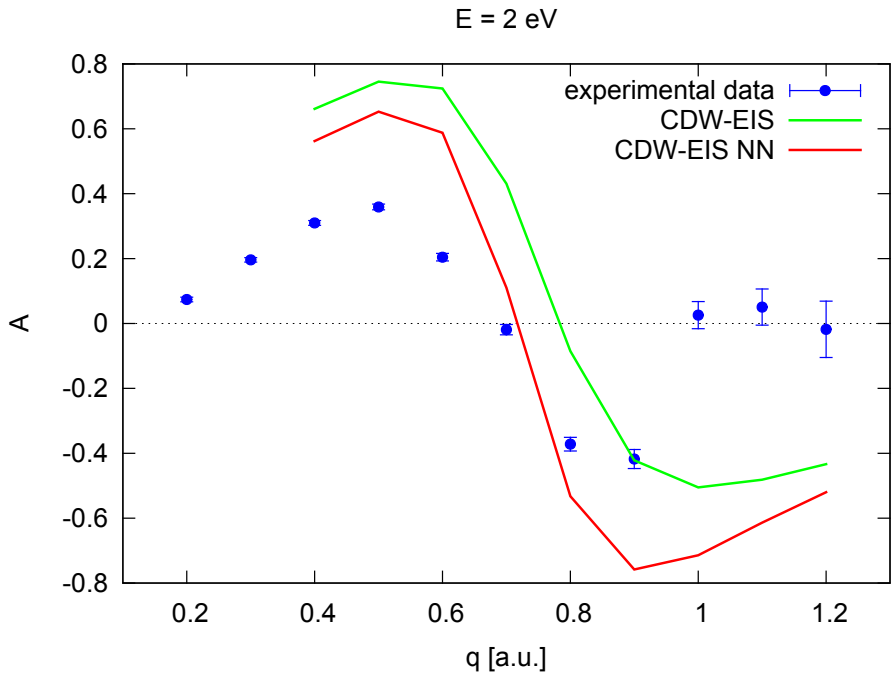

Figure 5.18: Dependence of the asymmetry parameter to the momentum transfer for ionization of the $2p$ electron. The projectile is 16 MeV Li^{2+}, the energy is fixed at $E_e^f = 2\,\text{eV}$. The inclusion of the nucleus-nucleus (NN) interaction improves the agreement of the theory with the experimental data.

zero-crossing is at a different value for the momentum transfer, which can be explained by the shift of the q-θ-dependence (eq. (5.7)) caused by the different final electron energy. Theoretical calculations (only for the case of $E_e^f = 6\,\text{eV}$) again agree qualitatively with the experimental data.

The asymmetry parameter for a 24 MeV O^{8+} is shown in fig. 5.20 for the electron energies $E_e^f = 2\,\text{eV}$ and $E_e^f = 10\,\text{eV}$. The overall sinusoidal behavior is similar to the lithium case, however, certain differences are visible. First, the magnitude of the asymmetry is smaller, which can be explained by the much larger perturbation of this collision system, i.e. the electrons are strongly influenced by the field of the projectile core, thus reducing the influence of the target core. Second, the zero-crossing is shifted to higher energies. For $E_e^f = 2\,\text{eV}$ it is at about $q = 1.2\,\text{a.u.}$, comparable to an energy of $E_e^f = 10\,\text{eV}$ in the Li^{2+} collision system. This might be caused by the influence of the nucleus-nucleus interaction.

5.3.3 Core-hole creation

In lithium single ionization does not only occur for outer shell electrons, but there is also the possibility of inner shell ionization (Fischer et al., 2012; Hubele, 2013). In fig. 5.21 the singly differential cross sections as a function of electron energy are shown for the two different Q values 5.4 eV and 65 eV, corresponding to $2s$ and $1s$ binding energies, respectively. Also plotted are CDW-EIS calculations for $2s$ and $1s$ ionization. While theory for L-shell ionization agrees fairly well with the experimental data, for K-shell ionization there are strong deviations, especially at low energies. One important limitation of the used calculation is, that the target

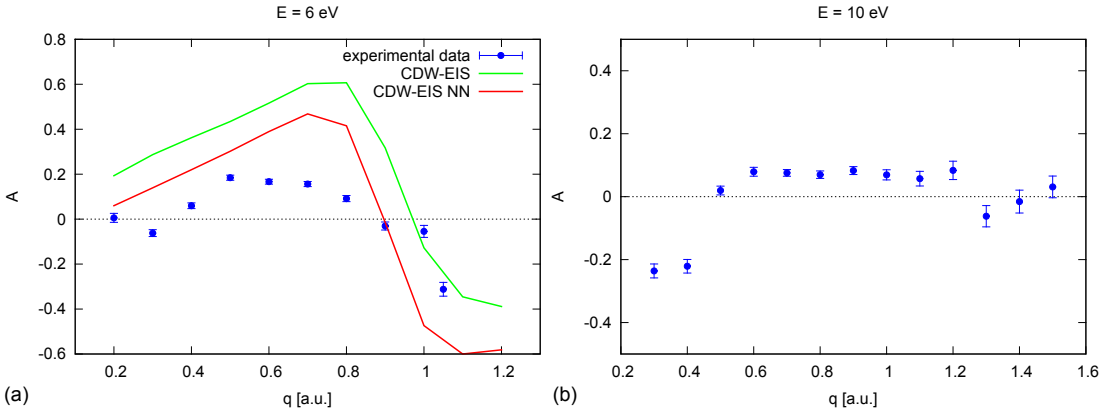

Figure 5.19: Dependence of the asymmetry parameter to the momentum transfer for ionization of the $2p$ electron. The projectile is 16 MeV Li^{2+}, the energy is fixed at $E_e^f = 6\,\text{eV}$ (a) and $E_e^f = 10\,\text{eV}$ (b).

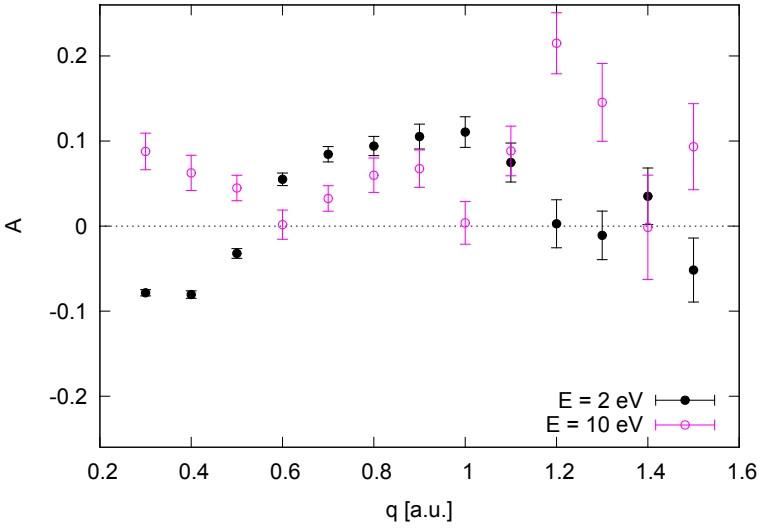

Figure 5.20: Dependence of the asymmetry parameter to the momentum transfer for ionization of the $2p$ electron. The projectile is 24 MeV O^{8+}, the energy is fixed at $E_e^f = 2\,\text{eV}$ and $E_e^f = 10\,\text{eV}$.

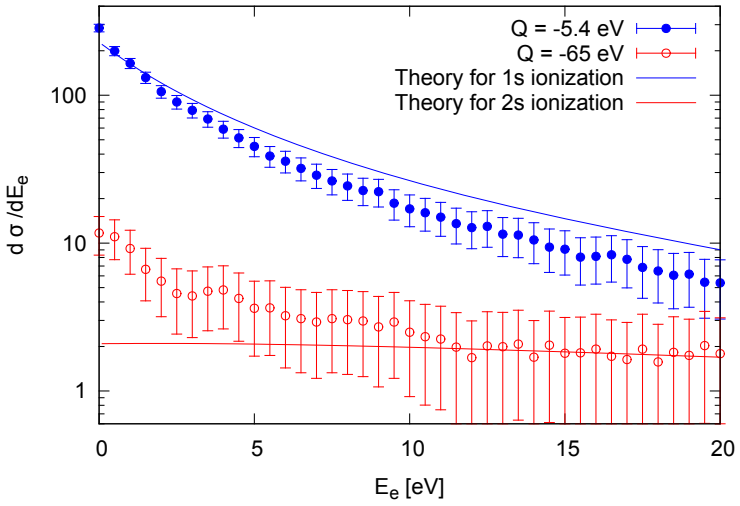

Figure 5.21: SDCS for different Q-values. The energy dependence is shown for single ionization of lithium by a 24 MeV O^{8+} projectile. CDW-EIS results for $1s$ and $2s$ ionization are plotted as lines.

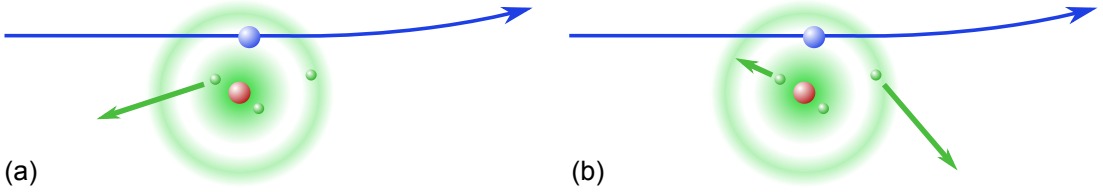

Figure 5.22: Illustration of $1s$ ionization (a) and ionization-excitation (b). Both processes have the same Q value and result in the same final state.

initial state is approximated with a single electron wave function in a Hartree-Fock potential. This seems to be reasonable for the description of $2s$ ionization. However, for $1s$ ionization, where the impact parameters are very small, two-electron effects can become important. E.g. the ionization of the 1s electron will result with high probability in double ionization, because the valence electron, which is 10 times weaker bound, will be emitted simultaneously.

Moreover, another process might occur, namely the excitation of the $1s$-electron with the simultaneous ejection of the $2s$ electron (see fig. 5.22). This mechanism results in the same final state (or in a state with a very similar Q-value) as the direct $1s$ ionization and cannot be separated in our experiment. However, such an excitation-ionization process is not accounted for in the calculation and it is expected to be more likely at small electron energies, as an emission of a stronger bound electron results in a larger electron momentum (and therefore electron energy) in the final state. As the two active electrons are only weakly correlated, excitation plus ionization is likely to proceed by two independent interactions of the projectile with the target rather than by electron-electron interaction, especially at the large perturbation of $\eta = 1$ a.u.

This process allows to study interesting aspects of ionization and of excitation. $2s$ ionization can be measured impact-parameter-selective, as the ionization-excitation process only occurs at close collisions. On the other hand, differential data on excitation can be gained by employing the ionized electron as a marker.

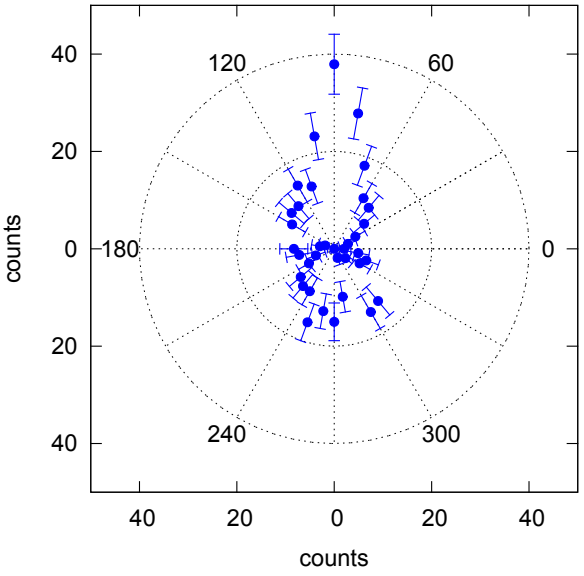

Figure 5.23: FDCS for core-hole creation for the $1s^2 2s$ configuration. The collision system is 16 MeV Li^{2+} on lithium, here at an electron energy of $E_e = 2$ eV and a momentum transfer $q = 0.7$ a.u.

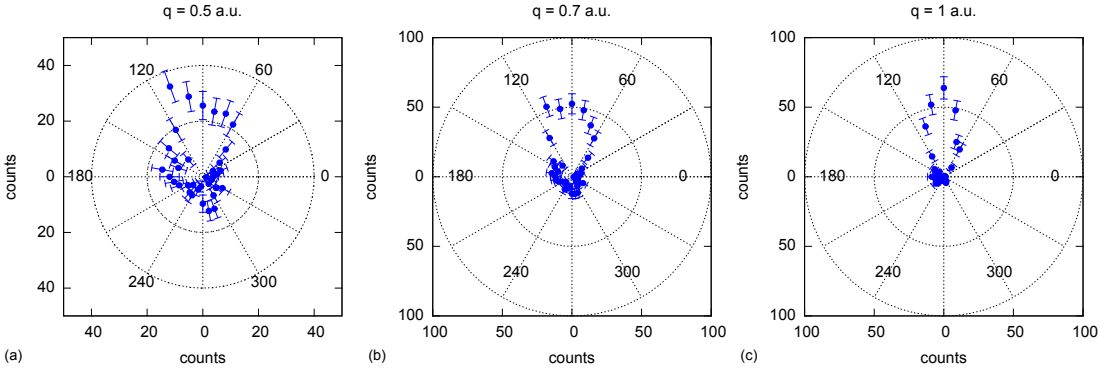

Figure 5.24: FDCS for core-hole creation for the $1s^2 2s$ configuration. The collision system is 16 MeV Li^{2+} on lithium, here at an electron energy of $E_e = 20$ eV and a momentum transfer of $q = 0.5$ a.u. (a), $q = 0.7$ a.u. (b) and $q = 1.0$ a.u. (c).

Additionally, when ionization-excitation is occurring, a dependence on the configuration of the valence electron should be seen. As stated in the previous chapters, this allows to investigate $2s$ and $2p$ ionization, in this case combined with core-hole excitation.

5.3.3.1 Ionization and core-hole creation for the $1s^2 2s$ configuration

For the initial configuration $1s^2 2s$ the FDCS in the azimuthal plane are shown for $E_e = 2$ eV and $q = 0.7$ a.u. in fig. 5.23 and for $E_e = 20$ eV and $q = 0.5$ a.u.,$q = 0.7$ a.u. and $q = 1.0$ a.u. in fig. 5.24. The general structure is similar to earlier observed cross sections for helium targets. There is a larger peak (the 'binary' peak) in the direction of the momentum transfer and a smaller one (the 'recoil' peak) in the opposite direction. As it is expected, the relative importance of the recoil peak decreases with larger energy and momentum transfer (Fischer et al., 2003a).

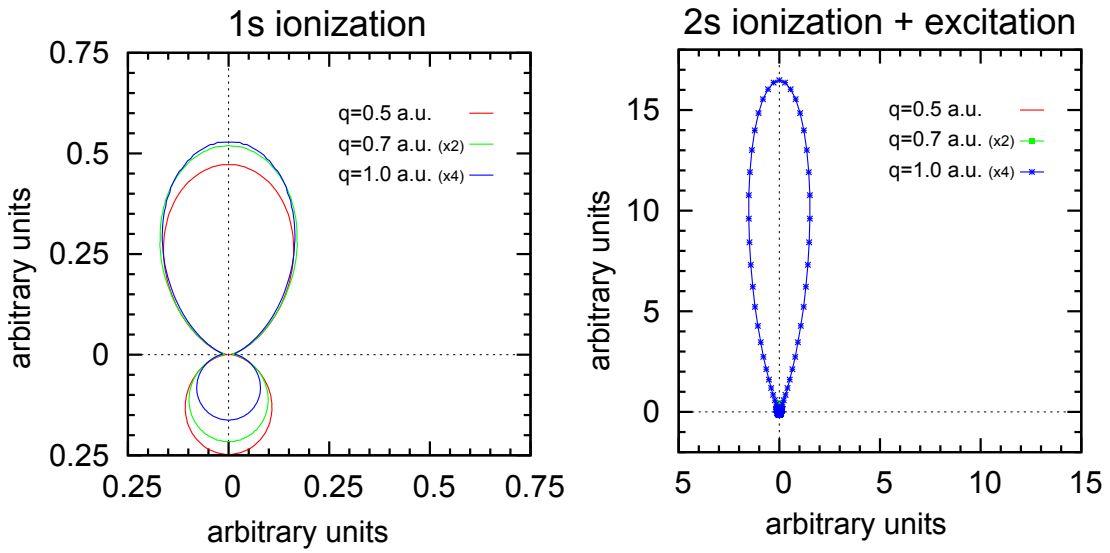

Figure 5.25: IMPACT calculation of the FDCS for $1s$ ionization and $2s$ ionization + excitation. The lithium target is ionized by a 16 MeV Li^{2+} projectile with a constant final electron energy of $E_e = 20\,\text{eV}$ for different momentum transfers. The calculations for different q in the ionization+excitation case cannot be distinguished (Kheifets, 2013).

Two calculations with different theories were performed (Kheifets, 2013). One used an independent electron approximation (coded IMPACT, (Sidorovich et al., 1985)), while a second employed channel coupling (CCC, (Kheifets et al., 1999)). In the IMPACT code the ejected electron energy was fixed at 20 eV, while in the CCC calculation the momentum transfer was kept constant at 88 eV. Each model calculated $1s$ ionization as well as ionization-excitation as two separated steps. The resulting spectra are shown in fig. 5.25 and fig. 5.26.

The IMPACT calculation shows a distinct difference between the two processes. For ionization-excitation, the recoil peak is completely absent independent of the momentum transfer. Comparing to the experimental data in fig. 5.24, the ionization-excitation process seems to happen preferably at high q, where no recoil peak is observed. However, the calculation for $1s$ ionization shows a decrease of the recoil peak with a simultaneous growth of the binary peak with increasing momentum transfer. This can also explain the general trend of the observations, but a complete absence of the recoil peak cannot be seen here. The CCC calculations do not differ much for the two processes. Here a shrinking of the recoil peak with increasing q can be observed as well as an overall magnitude increase. These features are consistent with the experimental data.

For ionization-excitation the two calculations differ greatly, as no recoil peak can be seen in the IMPACT theory for any momentum transfer, while CCC shows a recoil peak that shrinks with increasing q. In the experimental data, a recoil peak is only present for small momentum transfers, at $q = 1.0\,\text{a.u.}$ it is completely gone. This indicates that at lower momentum transfer ionization-excitation can be described by channel coupling (CCC) and at higher q two independent interactions with the projectile (IMPACT) are mainly contributing to the cross section. This can, once more, be understood considering the impact parameter: two independent interactions with the projectile require close collisions, resulting in large momentum transfers.

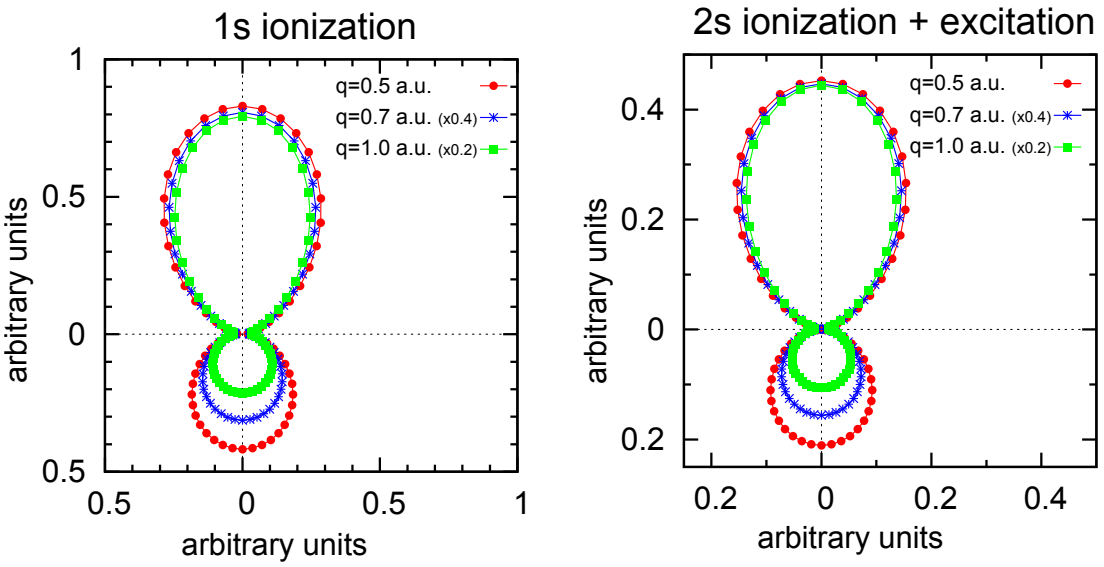

Figure 5.26: CCC calculation of the FDCS for $1s$ ionization and $2s$ ionization + excitation. The lithium target is ionized by a 16 MeV Li^{2+} projectile with a constant energy transfer of 88 eV for different momentum transfers (Kheifets, 2013).

It has to be noted that the cross sections can be influenced by the interference of the two processes (see also section 2.1.3 and section 5.3.1), which are not accounted for in the calculations.

5.3.3.2 Ionization and core-hole creation for the $1s^2 2p$ configuration

As explained in section 5.3.2, the ionization of a $2p$ electron shows orientational dichroism, which is caused by the polarization of our lithium target. This effect should also be observable for the ionization-excitation process. In the following the asymmetry parameter introduced in section 5.3.2 will be used to compare the dichroism with core-hole excitation to the one for pure $2p$ ionization.

What can we expect from the dichroism in $2p$ ionization with core-hole creation? First, it provides further evidence of the occurrence of ionization-excitation. In $1s$ ionization no dichroism can appear (neglecting electronic correlation), because the $1s$ wave function is isotropic. For ionization-excitation, the $2p$ electron can be ionized, which should feature a dichroism comparable to the one seen in direct $2p$ ionization. Second, the course of the single differential cross-section for core hole creation (red open circles in fig. 5.21) can be investigated. As stated before, the ionization-excitation process is expected to happen more likely at small electron energies, where the discrepancies to the $1s$ theory are most distinct. When this is the case, the dichroism should become less pronounced at higher energies.

In fig. 5.27 the q-dependence of the asymmetry parameter for pure $2p$ (blue) and $2p$ ionization with core hole creation is shown for $E_e = 2$ eV for the 16 MeV Li^{2+} projectile. The polar plots for each data point can be found in section 7.2. The asymmetry has the same magnitude as in direct $2p$ ionization, however, the asymmetry seems to be reversed, i.e. the sinusoidal progression is shifted by about 180°. This can be explained by the difference of the processes: while pure $2p$ ionization is possible for large impact parameters, $2p$ ionization with core-hole creation requires close collisions, i.e. small impact parameters. In close collisions the momentum transfer is

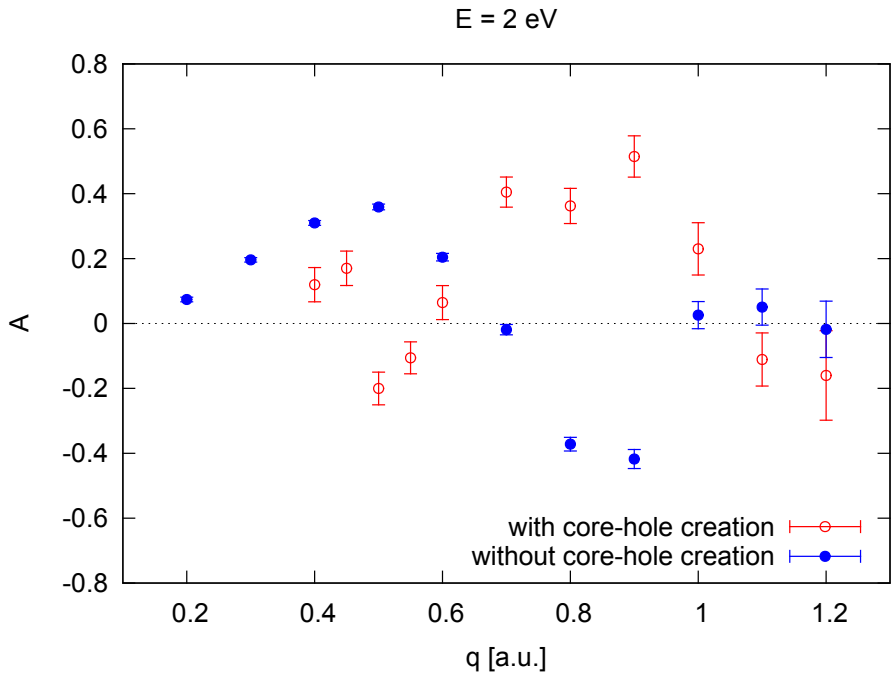

Figure 5.27: Dependence of the asymmetry parameter to the momentum transfer for ionization of the $2p$ electron. The projectile is 16 MeV Li^{2+}, the energy is fixed at $E_e^f = 2\,\text{eV}$.

larger, hence the recoil ion receives a bigger momentum than in pure $2p$ ionization. This results in an overall shifted distribution of the asymmetry parameter.

At an energy of $E_e^f = 10\,\text{eV}$ the magnitude of the asymmetry should decrease, as $1s$ ionization is supposed to dominate here. This is not the case, the asymmetry is similar to what is observed in fig. 5.28.

Similar observation are made for the 24 MeV O^{8+} projectile; the asymmetry parameter is plotted at $E_e^f = 2\,\text{eV}$ in fig. 5.29. Again, the shape is shifted and the magnitude of the asymmetry parameter is now even larger in the case of core-hole creation. Here the higher perturbation of this collision system has to be considered, which leads to higher order effects.

It should be emphasized, that the here discussed process of excitation and ionization is an ideal test ground for few-electron and higher-order theories. However, the theoretical modelling of the different reaction channels, their interference, and the influence of electronic correlation is extremely challenging and presently there is no calculation available that accounts for all these effects. Still, the analysis of the qualitative features of experimental spectra provides some insight in the effects that influence the correlated few-particle dynamics.

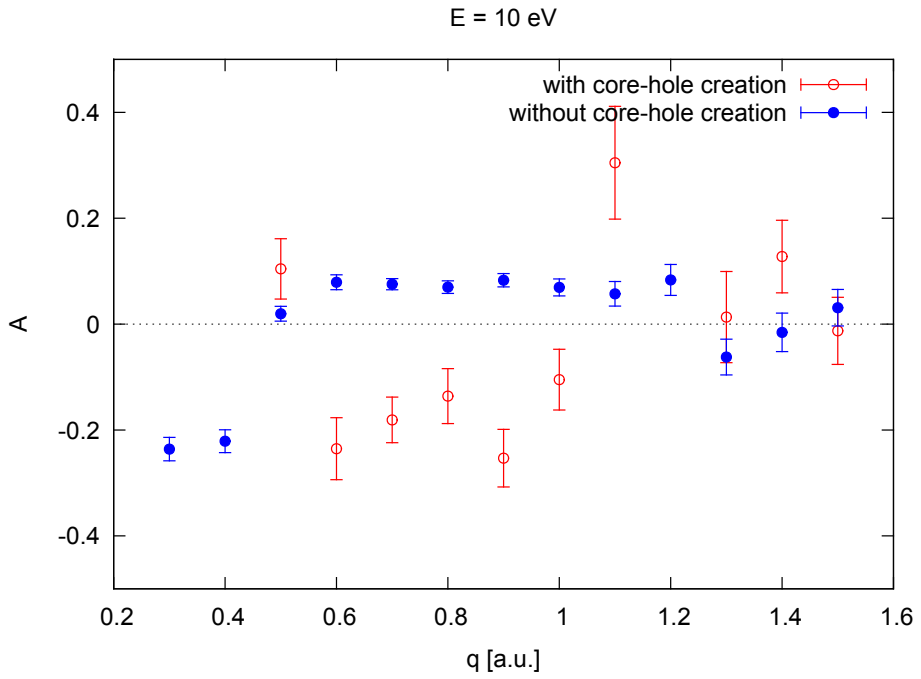

Figure 5.28: Dependence of the asymmetry parameter to the momentum transfer for ionization of the $2p$ electron. The projectile is 16 MeV Li^{2+}, the energy is fixed at $E_e^f = 10\,\text{eV}$.

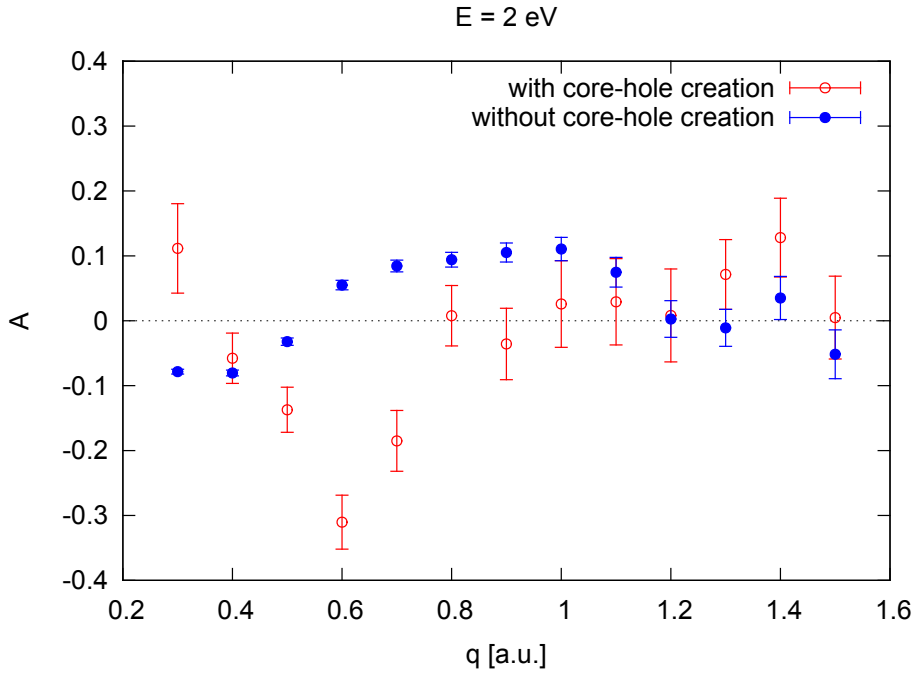

Figure 5.29: Dependence of the asymmetry parameter to the momentum transfer for ionization of the $2p$ electron. The projectile is 24 MeV O^{8+}, the energy is fixed at $E_e^f = 2\,\text{eV}$.

6. Summary and outlook

In the course of this work the dynamics of one- and two-electron transitions in collisions of ions with lithium was investigated. The measurements were enabled by a novel experimental apparatus, the MOTReMi. In the MOTReMi, laser cooling and trapping techniques in a magneto-optical trap (MOT) are applied for target preparation in a momentum imaging spectrometer, i.e. in a reaction microscope (ReMi). This new apparatus overcomes limitations of conventional reaction microscopes (equipped with gas-jet targets) with respect to the momentum resolution of the recoil ions and with respect to the target species (typically noble gases). In the present experiments lithium was chosen as target. With its three electrons, it is still a rather simple atom, but at the same time its electronic structure is more variegated than that of helium which was used as a target in most earlier experiments. Lithium has two strongly correlated electrons in the K-shell and one weakly correlated (hydrogen-similar) valence electron. Therefore, by choosing the active electron it becomes possible to 'tune' the electronic correlation. Moreover, the optical trapping in a MOT has the advantage of allowing to use excited and even polarized target atoms.

Technically, the combination of MOT and ReMi represents a large challenge, because the magnetic fields required for the MOT (quadrupole field) and the ReMi (homogeneous field) are essentially incompatible. These challenges have been solved in the present experiments by a sophisticated switching cycle of the MOT field and by employing a trapping scheme different from conventional MOTs, called 'vortex-force atom trap' (Walker et al., 1992a).
The MOTReMi was operated in the ion storage ring TSR, which provides ionic projectiles with energies in the MeV range. The ions are electron-cooled, hence their transverse coherence length, which recently is discussed to influence significantly the collision dynamics (Colgan et al., 2011; Walters and Whelan, 2012; Wang et al., 2012; Kouzakov et al., 2012; Schulz et al., 2013; Kouzakov et al., 2013; Feagin and Hargreaves, 2013), is rather large compared to single-pass experiments.

In this work collisions between lithium and 16 MeV O^{7+} as well as 16 MeV Li^{2+} projectiles were investigated. The studies with the former projectile species were focused on the measurements single electron capture (SC, where a target electron is

captured by the projectile) and transfer ionization (TI, where one target electron is captured and a second one ionized), while for the latter mainly single ionization (SI, where one target electron is ionized) was investigated.

In the SC measurements cross sections differential in the projectile scattering angle as well as selective with respect to the final state, in which the active electron was captured, were obtained. Overall, these measurements turned out to be extremely challenging, because, the signal-to-noise ratio is strongly limited by the very low capture cross section and the low target density.

The main interest in the TI measurements was the comparison to previous measurements with the same projectile, but helium as target. In this experiment similar challenges as in the case of SC arise, however, for TI the signal-to-noise ratio was significantly improved by switching the spectrometer fields synchronously to the detection of a charge-changed projectile. As two electrons are involved in the TI process, the difference in electron correlations between the two targets resulted in different emission characteristics of the ionized electron. While the emission characteristics are similar in the scattering plane (spanned by projectile momentum and momentum transfer), the azimuthal plane (perpendicular to the projectile momentum) inhibits large differences. While in the collision with helium a electron emission pattern similar to single ionization is observed, the lithium data shows isotropic emission. These differences are explained by the very different electronic structure of the two target species which result in the dominance of different reaction mechanisms. For lithium the shake-off of the loosely bound valence electron is much more likely than for helium. For helium, in turn, the ionization of the second electron is predominantly caused by a second interaction with the projectile. A comparison to theoretical calculations showed overall satisfactory agreement.

The main results in this work are related to SI measurements. These are divided into three parts: $2s$ ionization, $2p$ ionization and core-hole creation.

The ionization of the $2s$ electron in lithium is a process which is assumed to be very similar to the ionization of the hydrogen ground state. Due to the rather low perturbation of $\eta = 0.2$ a.u. for the Li^{2+} projectile and the small ionization potential the ionization cross section is dominated by dipole transitions which result in fully differential cross sections with a double lobe structure, i.e. a pronounced peak in direction of the momentum transfer ('binary' peak) and a smaller one in the opposite direction ('recoil' peak) (Schulz et al., 2001). In the first Born approximation the double lobe emission pattern should be symmetric with respect to the momentum transfer direction. In earlier measurements with a helium target strong deviations from this symmetry have been observed (Schulz et al., 2003). Several possible explanations were discussed, most recently the influence of the projectile coherence length in accord to experimental observations with a coherent beam (Wang et al., 2012). But also other effects were considered to cause the deviations, among them the experimental resolution (Olson and Fiol, 2005; Dürr et al., 2007) and electronic correlation effects in the helium target (Olson and Fiol, 2003). In the present experiment the resolution is substantially improved and correlation effects are much weaker for the lithium valence electron. Therefore, and investigation of this process for lithium target might shed more light on the origin of the long-standing puzzle. In the present investigations, also asymmetries with respect to the momentum transfer direction are found which, similar to (Wang et al., 2012), are assigned to the finite

projectile coherence length.

Due to the optical excitation in the MOT, also the ionization of the $2p$ electron can be studied. in the present experiment only one magnetic sub-level of the target (e.g. $m_L = 1$) is predominantly populated, corresponding to a polarization of the target. The additional direction introduced by the polarization axis results in a further symmetry breaking: For an isotropic target state the FDCS has to be symmetric to the scattering plane, which is defined by the momentum vectors of the incoming and outgoing projectile. Due to the axis introduced by the target orientation the electron flux is significantly shifted in one direction out of the scattering plane. This shift has been systematically investigated as a function of momentum transfer and electron energy and the underlying collision dynamics was explained in an intuitive classical picture. The comparisons to a CDW-EIS model show and overall very good agreement.

Another single ionization process discussed in this work is accompanied with the creation of a core-hole in the lithium target. In general, this final state can be reached through two pathways (Fischer et al., 2012): First, by the direct ionization of the K-shell electron, and second, by the excitation of the inner electron and the simultaneous emission of the valence electron. For ionization and core-hole creation of the $1s^2 2s$ configuration the dependence on the momentum transfer was investigated. For low momentum transfer a binary and a recoil peak can be observed in the azimuthal plane. With increasing momentum transfer the recoil peak vanishes and the binary peak becomes more narrow. Two different theoretical calculations led to the conclusion that at the lower end of momentum transfer the ionization-excitation process takes place by a coupling between the electrons, while at higher momentum transfers two independent interactions with the projectile are preferred. This seems reasonable, as the momentum transfer is larger for small impact parameters, which are needed for two independent interactions. Ionization and core-hole creation of the $1s^2 2p$ configuration shows a clearly visible dichroism. Its dependence on the momentum transfer is also sinusoidal, however, it is shifted in comparison to the pure $2p$ ionization. In (Fischer et al., 2012) the ionization-excitation process was supposed to be only dominant for small electron energies, which would result in a smaller dichroism at larger energies – this can be confirmed by the presented data.

Future experiments with the MOTReMi are planned in the CRYRING facility, which is currently built at GSI. The CRYRING has an ion energy range from 300 keV/u up to 14 MeV/u, hence allowing measurements with collision systems of much higher perturbations than in the TSR. In the long term even anti-protons will be available, opening other interesting fields of physics for reaction microscopes.

7. Appendix

7.1 Atomic Units

Atomic units are commonly used in atomic physics, as here their values are much easier to handle than the SI units. The basic consept of the atomic units are that the electron mass m_e, its charge e, the reduced Planck's constant and Coulomb's constant are set equal to unity:

$$m_e = e = \hbar = \frac{1}{4\pi\epsilon} = 1 \tag{7.1}$$

The conversion factors to the SI system are listed in table 7.1, as well as some other useful relations.

Physical quantity	a.u.	SI units	Special
mass	m_e	$9.1094 \times 10^{-31}\,\mathrm{kg}$	1823^{-1} u
ang. mom.	$\hbar$	$1.0546 \times 10^{-34}\,\mathrm{J\,s}$	
charge	e	$1.6022 \times 10^{-19}\,\mathrm{C}$	
length	a_0	$5.2918 \times 10^{-11}\,\mathrm{m}$	$0.53\,\text{Å}$
energy	E_h	$4.3597 \times 10^{-18}\,\mathrm{J}$	$27.2141\,\mathrm{eV}$
time	$\hbar/\mathrm{E}_h$	$2.4189 \times 10^{-17}\,\mathrm{s}$	
velocity	v_0	$2.1877 \times 10^{6}\,\mathrm{m\,s^{-1}}$	
momentum	$\mathrm{m}_e\mathrm{v}_0$	$1.9929 \times 10^{-24}\,\mathrm{kg\,m\,s^{-1}}$	
el. pot.	E_h/e	$27.211\,\mathrm{V}$	

$p_e\,[\text{a.u.}] = 0.27 \cdot \sqrt{E\,[\mathrm{eV}]}$	$1\,\mathrm{eV} \mathrel{\hat{=}} 8065.66\,\mathrm{cm^{-1}}$
$B\,[\mathrm{G}] = 357/T_{cyc}\,[\mathrm{ns}]$	$1\,\mathrm{u} \mathrel{\hat{=}} 1.66 \times 10^{-27}\,\mathrm{kg}$
$r_e\,[\mathrm{mm}] = 33.7 \cdot \sqrt{E\,[\mathrm{eV}]}/B\,[\mathrm{G}]$	

Table 7.1: Conversion factors from atomic units to Si units and assorted useful relations.

7.2 FDCS for 2p ionization used for the asymmetry parameter

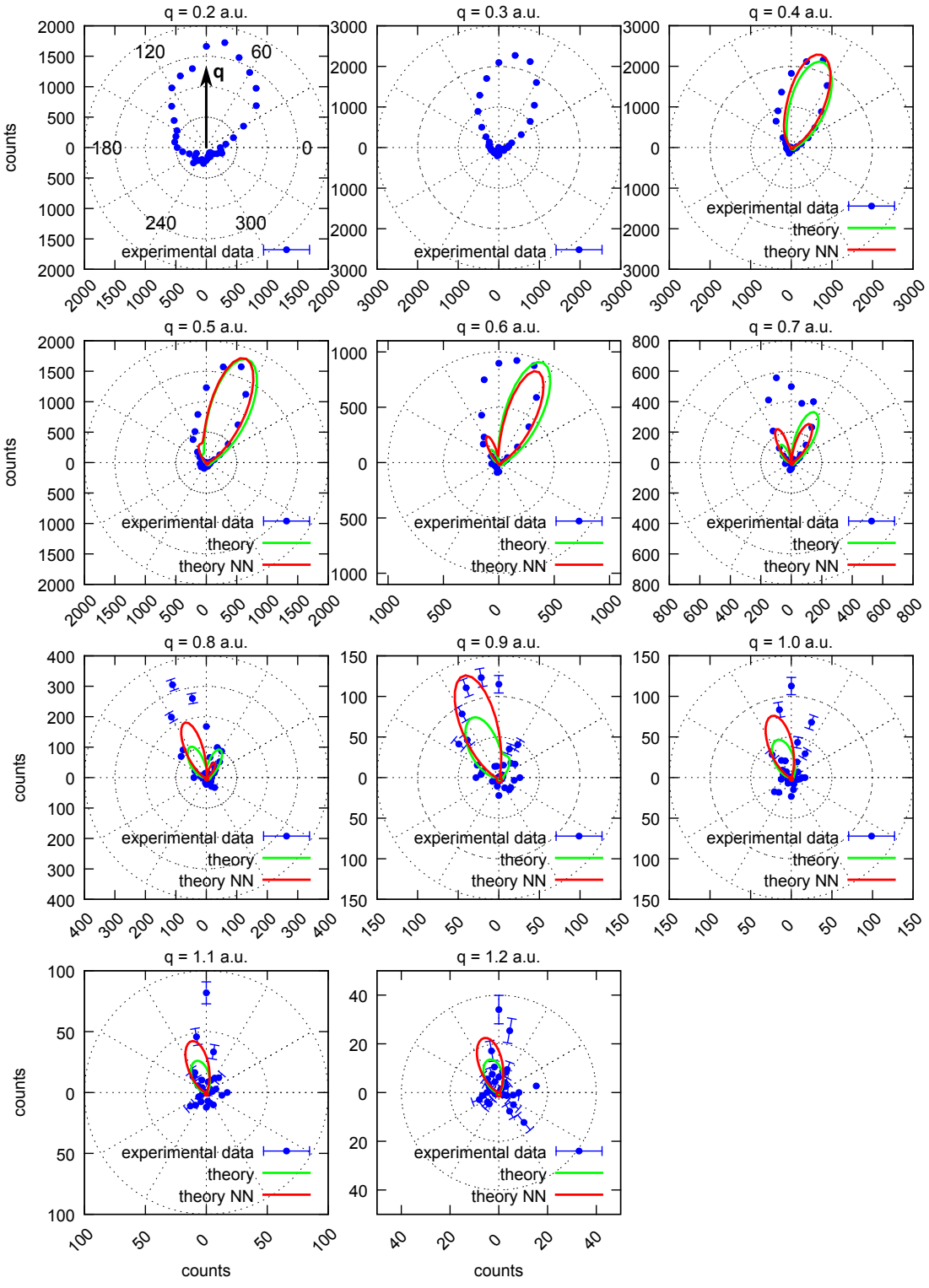

Figure 7.1: Collision system: 16 MeV Li^{2+}; $E_e = 2$ eV; without core-hole creation. Theoretical calculation are based on the CDW-EIS theory with and without nucleus-nucleus interaction. It was normalized to the data at $q = 0.5$ a.u..

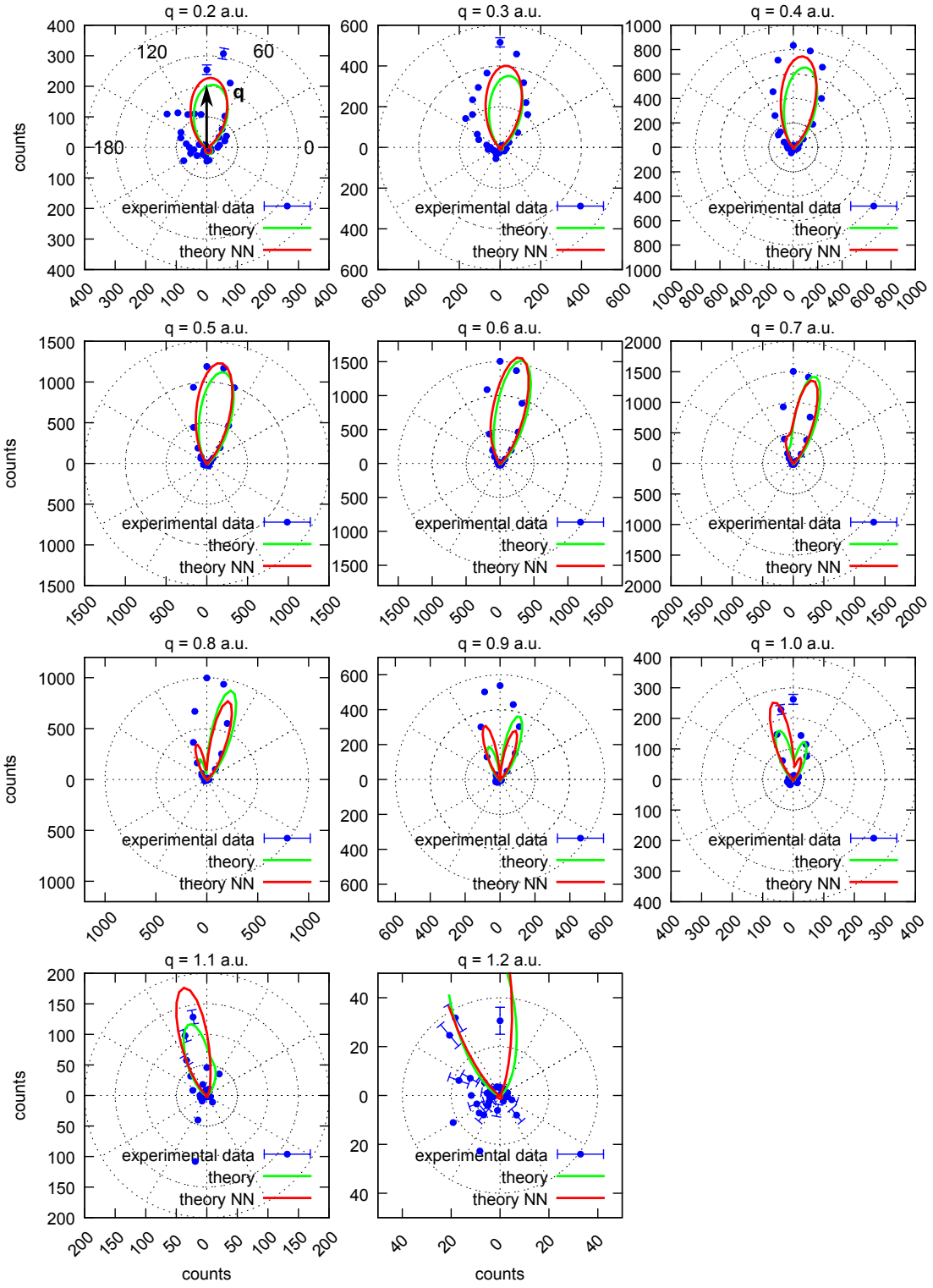

Figure 7.2: Collision system: 16 MeV Li^{2+}; $E_e = 6$ eV; without core-hole creation. Theoretical calculation are based on the CDW-EIS theory with and without nucleus-nucleus interaction. It was normalized to the data at $q = 0.5$ a.u..

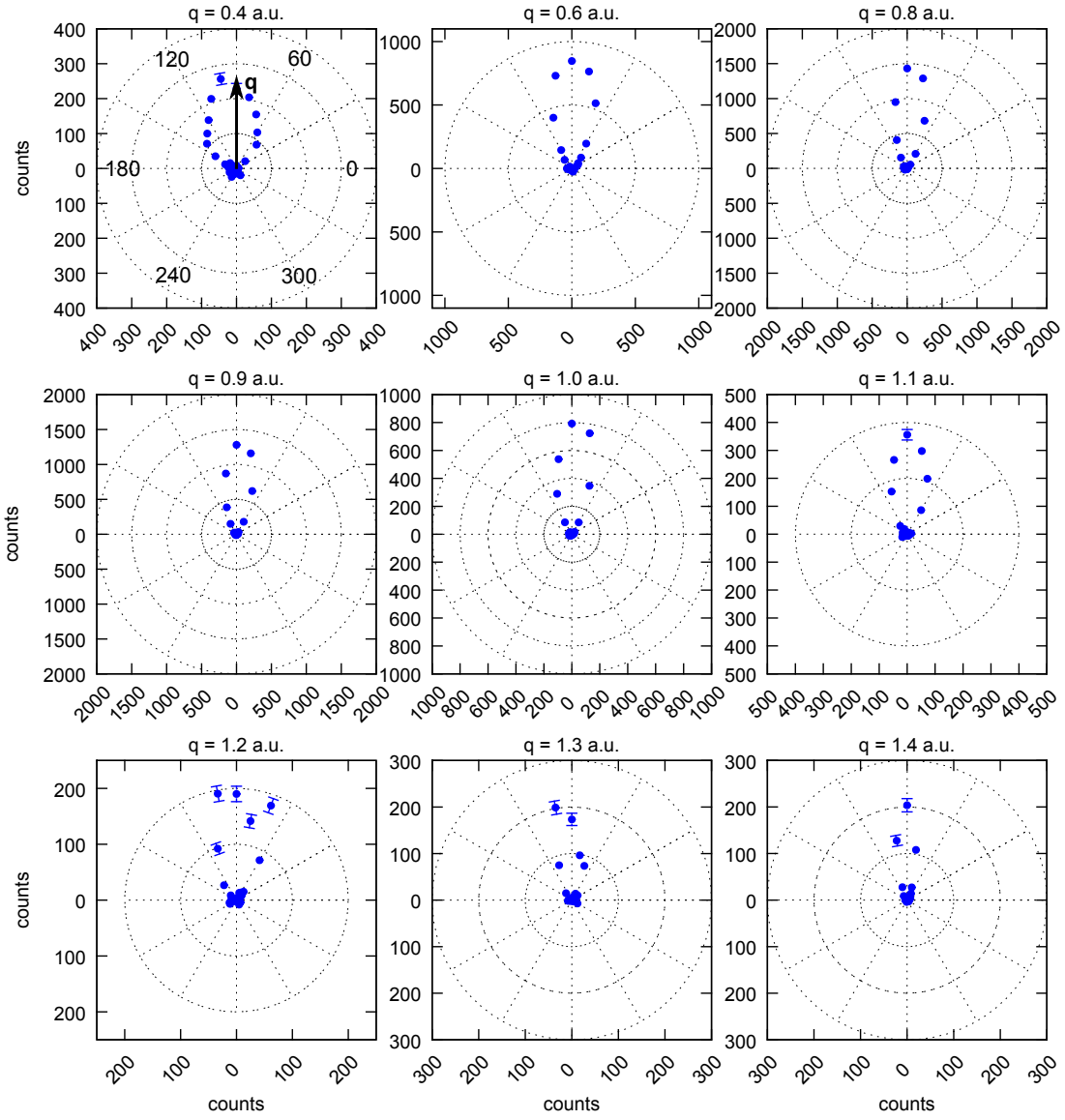

Figure 7.3: Collision system: 16 MeV Li^{2+}; $E_e = 10$ eV; without core-hole creation.

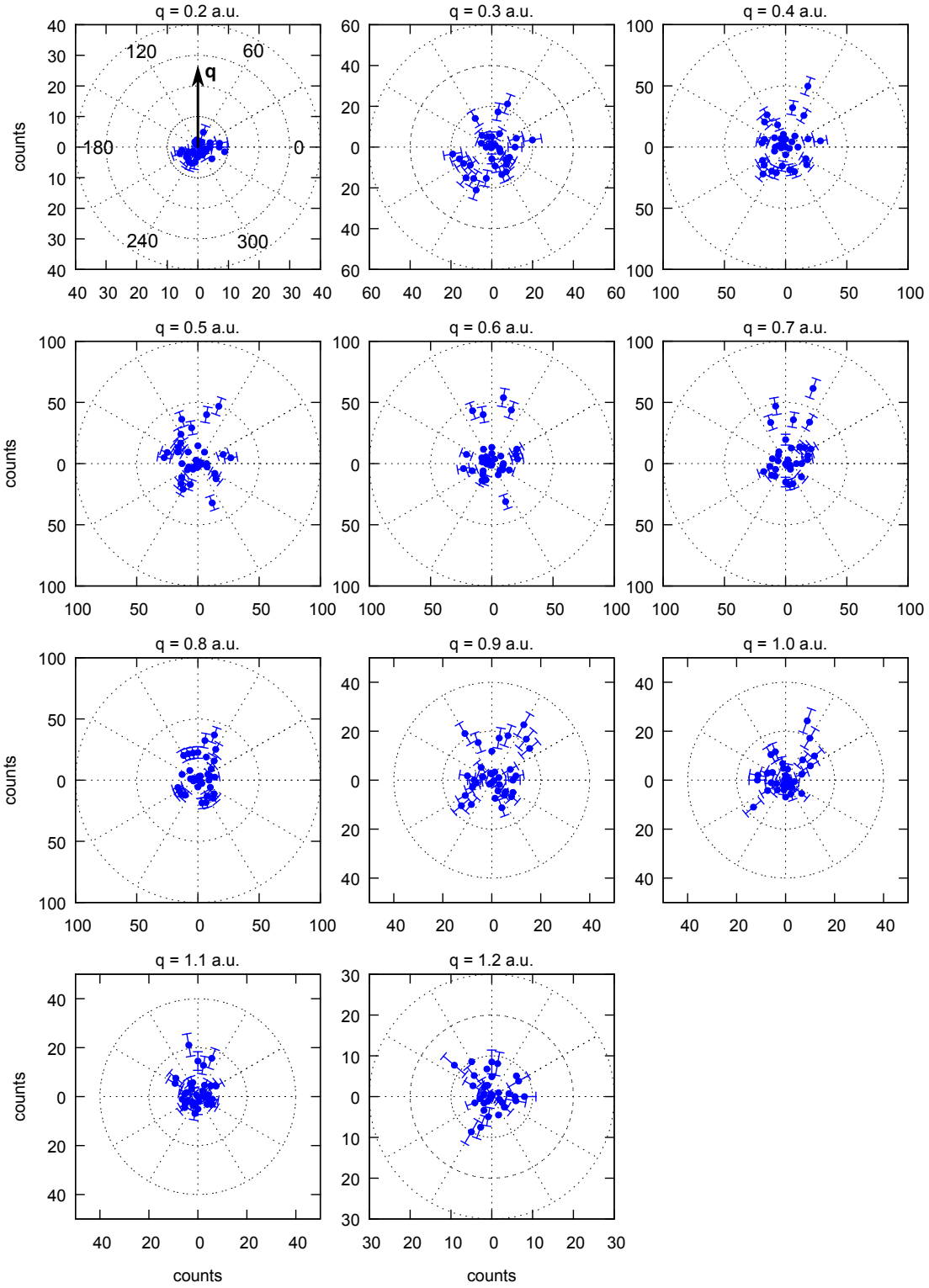

Figure 7.4: Collision system: 16 MeV Li^{2+}; $E_e = 2$ eV; with core-hole creation.

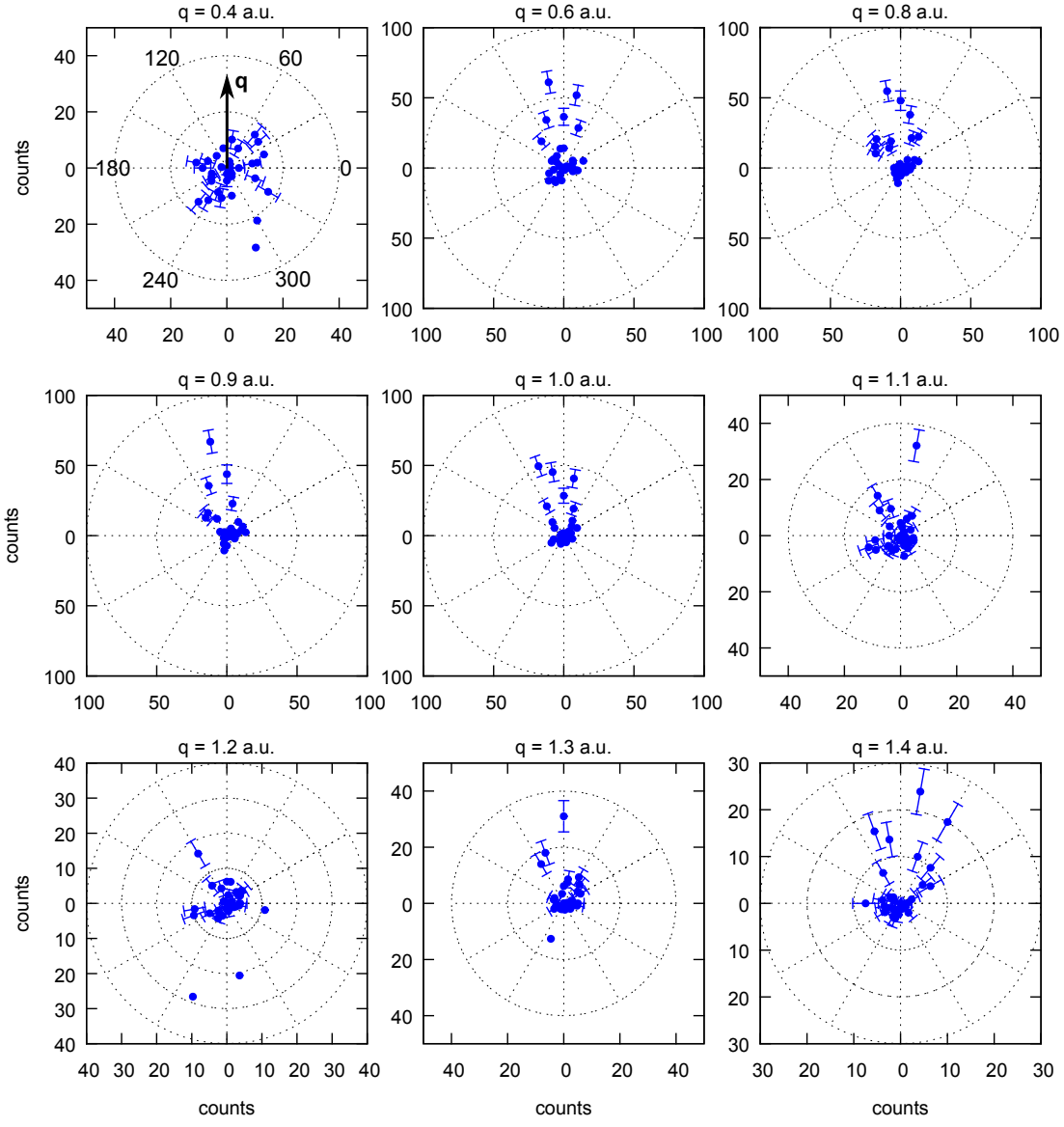

Figure 7.5: Collision system: 16 MeV Li^{2+}; $E_e = 10$ eV; with core-hole creation.

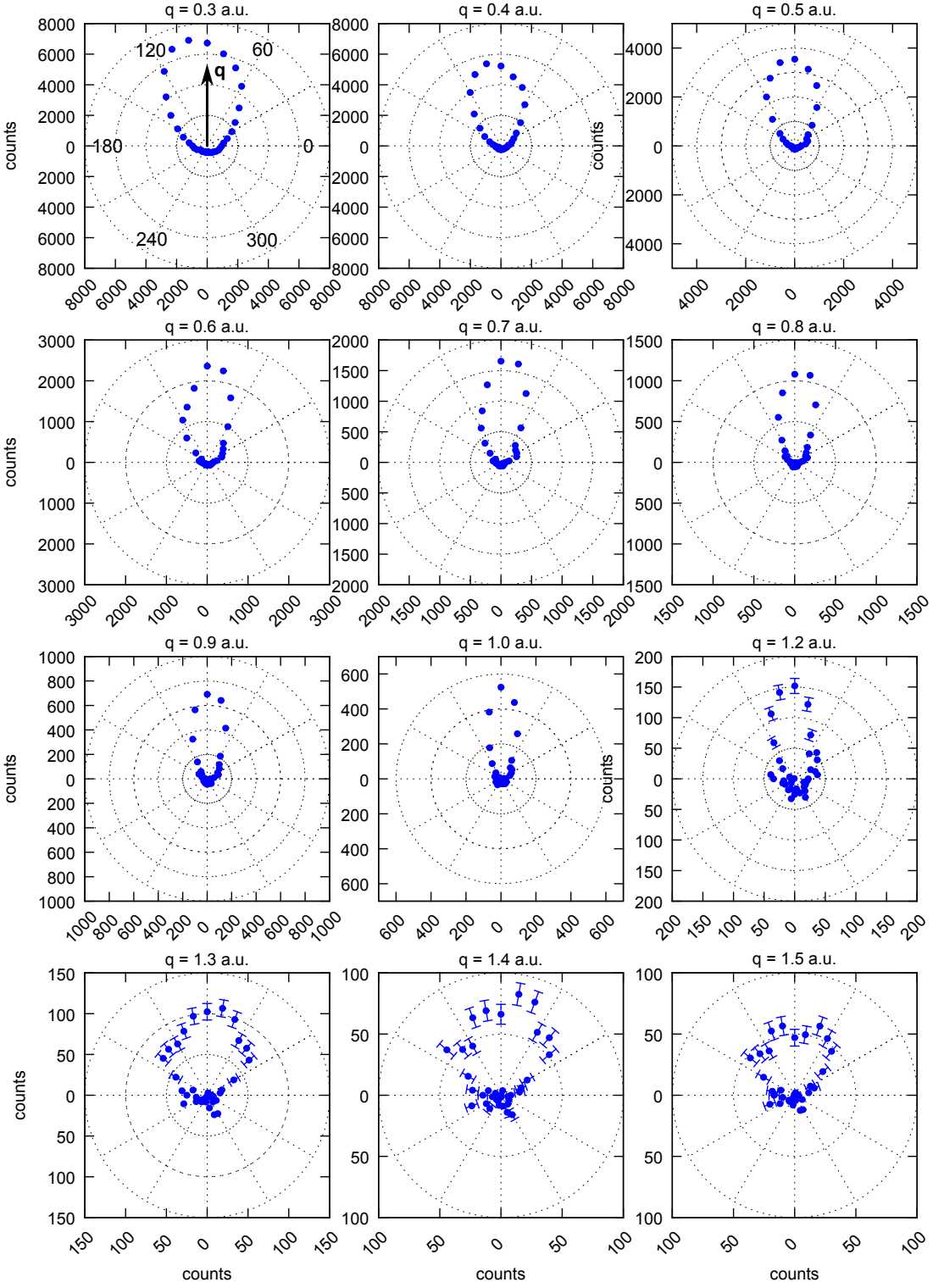

Figure 7.6: Collision system: 24 MeV O^{8+}; $E_e = 2$ eV; without core-hole creation.

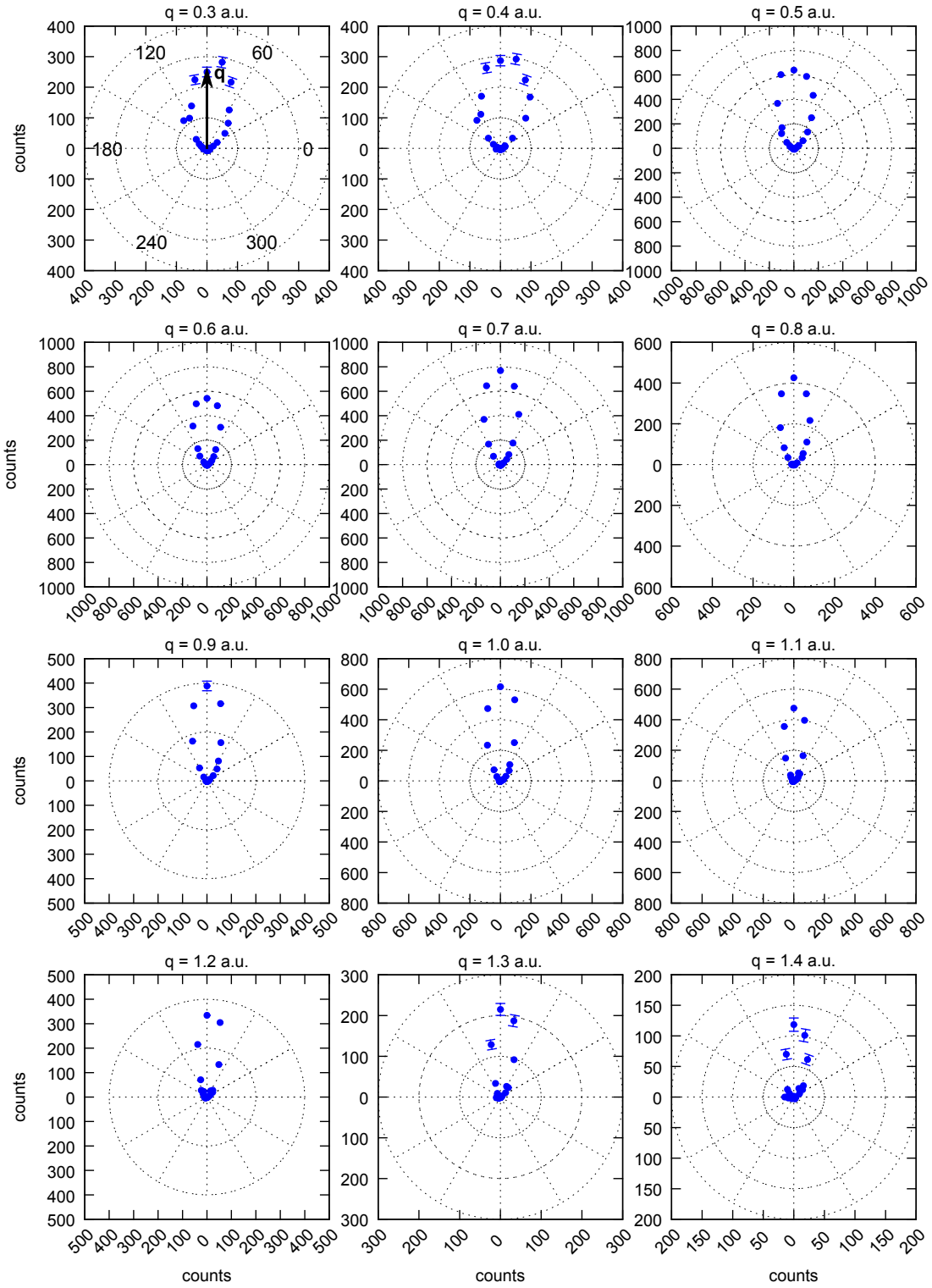

Figure 7.7: Collision system: 24 MeV O^{8+}; $E_e = 10$ eV; without core-hole creation.

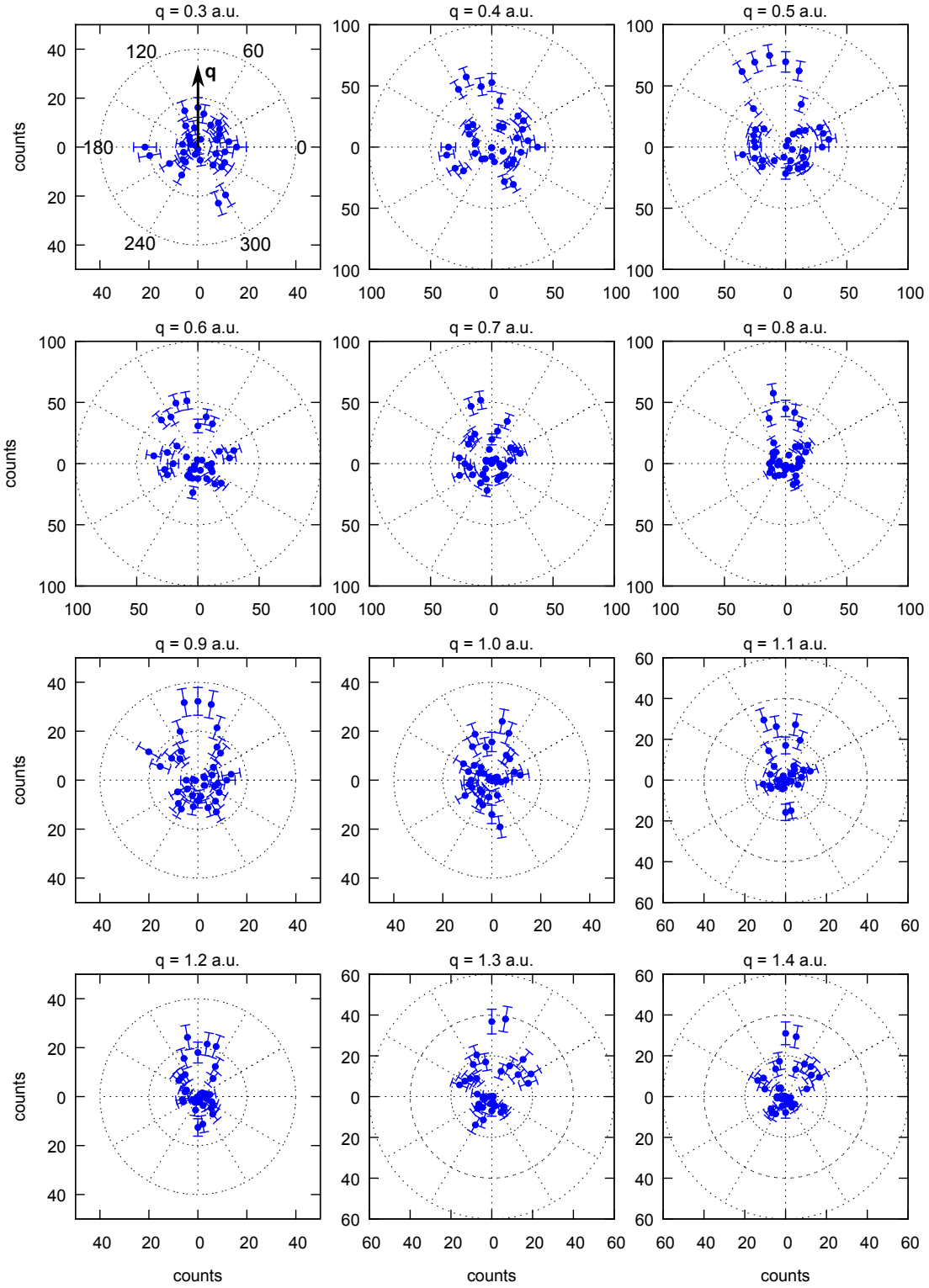

Figure 7.8: Collision system: 24 MeV O^{8+}; $E_e = 2$ eV; with core-hole creation.

Bibliography

Alexander, J. S. et al. (2008). "Interference effects due to projectile target nucleus scattering in single ionization of H_2 by 75 keVproton impact". In: *Phys. Rev. A* 78 (6), p. 060701. URL: http://link.aps.org/doi/10.1103/PhysRevA.78.060701.

Belkic, Dz (1978). "A quantum theory of ionisation in fast collisions between ions and atomic systems". In: *Journal of Physics B: Atomic and Molecular Physics* 11.20, p. 3529. URL: http://stacks.iop.org/0022-3700/11/i=20/a=015.

Belkic, Dz. et al. (1984). "Computation of total cross-sections for electron capture in high energy collisions. III". In: *Computer physics communication*.

Bellm, S. et al. (2006). "Electron-Impact Ionization and Excitation of Helium to the n = 1-4 Ionic States". In: *Phys. Rev. Lett.* 96 (22), p. 223201. URL: http://link.aps.org/doi/10.1103/PhysRevLett.96.223201.

Bjorklund, G.C. et al. (1983). "Frequency modulation (FM) spectroscopy". English. In: *Applied Physics B* 32.3, pp. 145–152. ISSN: 0946-2171. URL: http://dx.doi.org/10.1007/BF00688820.

Blieck, J. et al. (2008). "A new magneto-optical trap-target recoil ion momentum spectroscopy apparatus for ion-atom collisions and trapped atom studies". In: *Rev. Sci. Instrum.* 79, p. 103102.

Born, Max (1926). "Zur Quantenmechanik der Stoßvorgänge". German. In: *Zeitschrift für Physik* 37.12, pp. 863–867. ISSN: 0044-3328. URL: http://dx.doi.org/10.1007/BF01397477.

Bray, Igor (2002). "Close-Coupling Approach to Coulomb Three-Body Problems". In: *Phys. Rev. Lett.* 89 (27), p. 273201. URL: http://link.aps.org/doi/10.1103/PhysRevLett.89.273201.

Bray, Igor and Dmitry V. Fursa (1996). "Calculation of ionization within the close-coupling formalism". In: *Phys. Rev. A* 54 (4), pp. 2991–3004. URL: http://link.aps.org/doi/10.1103/PhysRevA.54.2991.

Bray, Igor and Andris T. Stelbovics (1992). "Convergent close-coupling calculations of electron-hydrogen scattering". In: *Phys. Rev. A* 46 (11), pp. 6995–7011. URL: http://link.aps.org/doi/10.1103/PhysRevA.46.6995.

Bray, Igor and Andris T. Stelbovics (1993). "Calculation of the total ionization cross section and spin asymmetry in electron-hydrogen scattering from threshold to 500 eV". In: *Phys. Rev. Lett.* 70 (6), pp. 746–749. URL: http://link.aps.org/doi/10.1103/PhysRevLett.70.746.

Briggs, J S and K Taulbjerg (1979). "Charge transfer by a double-scattering mechanism involving target electrons". In: *Journal of Physics B: Atomic and Molecular Physics* 12.15, p. 2565. URL: http://stacks.iop.org/0022-3700/12/i=15/a=017.

Brinkmann, H.C. and H.A. Kramers (1930). "Zur Theorie der Einfangung von Elektronen durch α-Teilchen." In: Proceedings Koninklijke Akademie van Wetenschappen 33.

Chu, S. et al. (1987). "Laser Cooling and Trapping of Atoms". In: *Laser Spectroscopy VIII*.

Clementi, E. and D. L. Raimondi (1963). "Atomic Screening Constants from SCF Functions". In: *The Journal of Chemical Physics* 38.11, pp. 2686–2689. URL: http://scitation.aip.org/content/aip/journal/jcp/38/11/10.1063/1.1733573.

Clementi, Enrico and Carla Roetti (1974). "Roothaan-Hartree-Fock atomic wavefunctions: Basis functions and their coefficients for ground and certain excited states of neutral and ionized atoms, Z$\leq$54". In: *Atomic Data and Nuclear Data Tables* 14.3, pp. 177 –478. ISSN: 0092-640X. URL: http://www.sciencedirect.com/science/article/pii/S0092640X74800161.

Cocke, C.L and R.E Olson (1991). "Recoil ions". In: *Physics Reports* 205.4, pp. 153 – 219. ISSN: 0370-1573. URL: http://www.sciencedirect.com/science/article/pii/037015739190072T.

Colgan, J et al. (2011). "Fully differential cross sections for the single ionization of He by C^{6+} ions". In: *Journal of Physics B: Atomic, Molecular and Optical Physics* 44.17, p. 175205. URL: http://stacks.iop.org/0953-4075/44/i=17/a=175205.

Coplan, M. A. et al. (1994). "(e,2e) spectroscopy". In: *Rev. Mod. Phys.* 66 (3), pp. 985–1014. URL: http://link.aps.org/doi/10.1103/RevModPhys.66.985.

Crothers, D S F and J F McCann (1983). "Ionisation of atoms by ion impact". In: *Journal of Physics B: Atomic and Molecular Physics* 16.17, p. 3229. URL: http://stacks.iop.org/0022-3700/16/i=17/a=015.

Das, Dipankar and Vasant Natarajan (2007). "Absolute frequency measurement of the lithium *D* lines: Precise determination of isotope shifts and fine-structure intervals". In: *Phys. Rev. A* 75 (5), p. 052508. URL: http://link.aps.org/doi/10.1103/PhysRevA.75.052508.

Davis, B. and A.H. Barnes (1929). "The Capture of Electrons by Swiftly Moving Alpha Particles". In: *Physical Review* 34.

Davis, Bergen (1923). "The Capture of Electrons by Swiftly Moving Alpha Particles". In: *Nature* 111, pp. 706–706.

Demtröder, Wolfgang (2002). *Experimentalphysik 2*. Springer.

Dorn, A. et al. (1998). "Orientational Dichroism in the Electron-Impact Ionization of Laser-Oriented Atomic Sodium". In: *Phys. Rev. Lett.* 80 (2), pp. 257–260. URL: http://link.aps.org/doi/10.1103/PhysRevLett.80.257.

Dumond, J.W.M. (1933). "The Linear Momenta of Electrons in Atoms and in Solid Bodies as Revealed by X-Ray Scattering". In: *Reviews of Modern Physics* 5, pp. 1–33.

Dürr, M. et al. (2007). "Analysis of experimental data for ion-impact single ionization of helium with Monte Carlo event generators based on quantum theory". In: *Phys. Rev. A* 75 (6), p. 062708. URL: http://link.aps.org/doi/10.1103/PhysRevA.75.062708.

Egodapitiya, K. N. et al. (2011). "Manipulating Atomic Fragmentation Processes by Controlling the Projectile Coherence". In: *Phys. Rev. Lett.* 106 (15), p. 153202. URL: http://link.aps.org/doi/10.1103/PhysRevLett.106.153202.

Ehrhardt, H. et al. (1969). "Ionization of Helium: Angular Correlation of the Scattered and Ejected Electrons". In: *Phys. Rev. Lett.* 22 (3), pp. 89–92. URL: http://link.aps.org/doi/10.1103/PhysRevLett.22.89.

Ehrhardt, H. et al. (1986). "Differential cross sections of direct single electron impact ionization". English. In: *Zeitschrift für Physik D Atoms, Molecules and Clusters* 1.1, pp. 3–32. ISSN: 0178-7683. URL: http://dx.doi.org/10.1007/BF01384654.

Eichler, J. and U. Wille (1974). "Two-Center Thomas-Fermi Model for Adiabatic Ion-Atom Collisions". In: *Phys. Rev. Lett.* 33 (2), pp. 56–59. URL: http://link.aps.org/doi/10.1103/PhysRevLett.33.56.

Fainstein, P D et al. (1991). "Two-centre effects in ionization by ion impact". In: *Journal of Physics B: Atomic, Molecular and Optical Physics* 24.14, p. 3091. URL: http://stacks.iop.org/0953-4075/24/i=14/a=005.

Fainstein, P. D. et al. (1996). "Angular asymmetry of low-energy electron emission in ion-atom collisions". In: *Phys. Rev. A* 53 (5), pp. 3243–3246. URL: http://link.aps.org/doi/10.1103/PhysRevA.53.3243.

Feagin, James M. and Leigh Hargreaves (2013). "Loss of wave-packet coherence in stationary scattering experiments". In: *Phys. Rev. A* 88 (3), p. 032705. URL: http://link.aps.org/doi/10.1103/PhysRevA.88.032705.

Fiol, J et al. (2006). "Critical comparison between theory and experiment for C^{6+} +He fully differential ionization cross sections". In: *Journal of Physics B: Atomic, Molecular and Optical Physics* 39.14, p. L285. URL: http://stacks.iop.org/0953-4075/39/i=14/a=L02.

Fischer, D et al. (2003a). "Fully differential cross sections for the single ionization of helium by ion impact". In: *Journal of Physics B: Atomic, Molecular and Optical Physics* 36.17, p. 3555. URL: http://stacks.iop.org/0953-4075/36/i=17/a=301.

Fischer, D. et al. (2003b). "Projectile-Charge Sign Dependence of Four-Particle Dynamics in Helium Double Ionization". In: *Phys. Rev. Lett.* 90 (24), p. 243201. URL: http://link.aps.org/doi/10.1103/PhysRevLett.90.243201.

Fischer, D. et al. (2006). "Experimental separation of the Thomas charge-transfer process in high-velocity p-He collisions". In: *Phys. Rev. A* 73 (5), p. 052713. URL: http://link.aps.org/doi/10.1103/PhysRevA.73.052713.

Fischer, D. et al. (2012). "Ion-Lithium Collision Dynamics Studied with a Laser-Cooled In-Ring Target". In: *Phys. Rev. Lett.* 109 (11), p. 113202. URL: http://link.aps.org/doi/10.1103/PhysRevLett.109.113202.

Fischer, Daniel (2003). "Mehr-Teilchen-Dynamik in der Einfach- und Doppelionisation von Helium durch geladene Projektile". PhD thesis. Ruperto-Carola University of Heidelberg.

Foster, M. et al. (2006). "Unexpected Higher-Order Effects in Charged Particle Impact Ionization at High Energies". In: *Phys. Rev. Lett.* 97 (9), p. 093202. URL: http://link.aps.org/doi/10.1103/PhysRevLett.97.093202.

Gayet, R. and A. Salin (1991). "Differential scattering in ionisation processes". In: *Nuclear Instruments and Methods in Physics Research Section B: Beam Interactions with Materials and Atoms* 56.0, pp. 82 –85. ISSN: 0168-583X. URL: http://www.sciencedirect.com/science/article/pii/0168583X9195977L.

go4 website. Accessed 11/2013. URL: http://www-win.gsi.de/go4/.

Grieser, M. et al. (2012). "Storage ring at HIE-ISOLDE". English. In: *The European Physical Journal Special Topics* 207.1, pp. 1–117. ISSN: 1951-6355. URL: http://dx.doi.org/10.1140/epjst/e2012-01599-9.

Griffith, David J. (2012). *Introduction to electrodynamics*. Pearson education.

Gulyas, L et al. (1995). "CDW-EIS theory of ionization by ion impact with Hartree-Fock description of the target". In: *Journal of Physics B: Atomic, Molecular and Optical Physics* 28.2, p. 245. URL: http://stacks.iop.org/0953-4075/28/i=2/a=013.

Horsdal, Erik et al. (1986). "Critical Angle in Electron Capture". In: *Phys. Rev. Lett.* 57 (12), pp. 1414–1416. URL: http://link.aps.org/doi/10.1103/PhysRevLett.57.1414.

Horsdal-Pedersen, E. et al. (1983). "Experimental Observation of the Thomas Peak in High-Velocity Electron Capture by Protons from He". In: *Phys. Rev. Lett.* 50 (24), pp. 1910–1913. URL: http://link.aps.org/doi/10.1103/PhysRevLett.50.1910.

Hubele, R. et al. (2013). "Polarization and Interference Effects in Ionization of Li by Ion Impact". In: *Phys. Rev. Lett.* 110 (13), p. 133201. URL: http://link.aps.org/doi/10.1103/PhysRevLett.110.133201.

Hubele, Renate (2013). "Kinematisch vollständige und zustands-selektive Untersuchung der stoßinduzierten Einfachionisation von Lithium". PhD thesis. Ruperto-Carola University of Heidelberg.

Jauncey, G. E. M. (1925). "Quantum Theory of the Unmodified Spectrum Line in the Compton Effect". In: *Phys. Rev.* 25 (3), pp. 314–321. URL: http://link.aps.org/doi/10.1103/PhysRev.25.314.

Kernphysik, Max-Planck-Institut für. *The Heidelberg Ion Beam Facilities*. Accessed: August 2013. URL: http://www.mpi-hd.mpg.de/blaum/accelerators/index.de.html.

Kheifets, A. S. (2013). private communication.

Kheifets, A S et al. (1999). "Convergent calculations for simultaneous electron-impact ionization-excitation of helium". In: *Journal of Physics B: Atomic, Molecular and Optical Physics* 32.15, p. L433. URL: http://stacks.iop.org/0953-4075/32/i=15/a=104.

Kim, Hong-Keun et al. (2012). "Electron transfer in fast proton-helium collisions". In: *Phys. Rev. A* 85 (2), p. 022707. URL: http://link.aps.org/doi/10.1103/PhysRevA.85.022707.

Kollmus, H. et al. (2002). "Simultaneous Projectile-Target Ionization: A Novel Approach to (e,2e) Experiments on Ions". In: *Phys. Rev. Lett.* 88 (10), p. 103202. URL: http://link.aps.org/doi/10.1103/PhysRevLett.88.103202.

Kouzakov, Konstantin A. et al. (2012). "Singly ionizing 100 MeV/amu C^{6+} + He collisions with small momentum transfer". In: *Phys. Rev. A* 86 (3), p. 032710. URL: http://link.aps.org/doi/10.1103/PhysRevA.86.032710.

– (2013). "Reply to 'Comment on 'Singly ionizing 100 MeV/amu C^{6+} + He collisions with small momentum transfer'". In: *Phys. Rev. A* 87 (4), p. 046702. URL: http://link.aps.org/doi/10.1103/PhysRevA.87.046702.

LaForge, A C et al. (2013). "Initial-state selective study of ionization dynamics in ion-Li collisions". In: *Journal of Physics B: Atomic, Molecular and Optical Physics* 46.3, p. 031001. URL: http://stacks.iop.org/0953-4075/46/i=3/a=031001.

Lahmam-Bennani, A (1991). "Recent developments and new trends in (e,2e) and (e,3e) studies". In: *Journal of Physics B: Atomic, Molecular and Optical Physics* 24.10, p. 2401. URL: http://stacks.iop.org/0953-4075/24/i=10/a=001.

– (2002). "Thirty years of experimental electron-electron (e,2e) coincidence studies: achievements and perspectives". In: *Journal of Electron Spectroscopy and Related Phenomena* 123.2. Determination of cross-sections and momentum profiles of atoms, molecules and condensed matter, pp. 365 –376. ISSN: 0368-2048. URL: http://www.sciencedirect.com/science/article/pii/S0368204802000336.

Madison, D et al. (2002). "Comparison of theoretical and absolute experimental fully differential cross sections for ion-atom impact ionization". In: *Journal of Physics B: Atomic, Molecular and Optical Physics* 35.15, p. 3297. URL: http://stacks.iop.org/0953-4075/35/i=15/a=305.

Madison, D. H. et al. (2003). "Probing Scattering Wave Functions Close to the Nucleus". In: *Phys. Rev. Lett.* 91 (25), p. 253201. URL: http://link.aps.org/doi/10.1103/PhysRevLett.91.253201.

Mancev, I et al. (2003). "Electron capture from helium atoms by fast protons". In: *Journal of Physics B: Atomic, Molecular and Optical Physics* 36.13, p. 2733. URL: http://stacks.iop.org/0953-4075/36/i=13/a=305.

McAlexander, W. I. et al. (1996). "Radiative lifetime of the $2P$ state of lithium". In: *Phys. Rev. A* 54 (1), R5–R8. URL: http://link.aps.org/doi/10.1103/PhysRevA.54.R5.

McConkey, J. W. et al. (1972). "Differential Cross Sections in the Electron Impact Ionization of Atoms and Molecules". In: *Phys. Rev. Lett.* 29 (1), pp. 1–4. URL: http://link.aps.org/doi/10.1103/PhysRevLett.29.1.

McDowell, M.R.C. and J.P. Coleman, eds. (1970). *Introduction to the theory of ion-atom collisions*. North-Holland Publishing Company.

McGovern, M. et al. (2010). "Coincidence studies of He ionized by C^{6+}, Au^{24+}, and Au^{53+}". In: *Phys. Rev. A* 81 (4), p. 042704. URL: http://link.aps.org/doi/10.1103/PhysRevA.81.042704.

McGuire, J. H. (1997). *Electron correlation dynamics in atomic collisions*. Cambridge Universty Press.

MCP Delay Line Detector Manual. Version 9.22.1003.1. RoentDek. RoentDek Handels GmbH, Im Vogelsang 8, D-65779 Kelkheim-Ruppertshain.

Mergel, V. et al. (1997). "Intra-atomic Electron-Electron Scattering in p-He Collisions (Thomas Process) Investigated by Cold Target Recoil Ion Momentum Spectroscopy". In: *Phys. Rev. Lett.* 79 (3), pp. 387–390. URL: http://link.aps.org/doi/10.1103/PhysRevLett.79.387.

Mergel, V. et al. (2001). "Strong Correlations in the He Ground State Momentum Wave Function Observed in the Fully Differential Momentum Distributions for the p+He Transfer Ionization Process". In: *Phys. Rev. Lett.* 86 (11), pp. 2257–2260. URL: http://link.aps.org/doi/10.1103/PhysRevLett.86.2257.

Metcalf, H. J. and P. van der Straten (1999). *Laser Cooling and Trapping*. Springer.

Misra, Deepankar et al. (2004). "Interference Effect in Electron Emission in Heavy Ion Collisions with H_2 Detected by Comparison with the Measured Electron Spectrum from Atomic Hydrogen". In: *Phys. Rev. Lett.* 92 (15), p. 153201. URL: http://link.aps.org/doi/10.1103/PhysRevLett.92.153201.

Montenegro, E. C. et al. (1992). "Separation of the screening and antiscreening effects in the electron loss of He^+ and H_2 and He". In: *Phys. Rev. Lett.* 69 (21), pp. 3033–3036. URL: http://link.aps.org/doi/10.1103/PhysRevLett.69.3033.

Moshammer, R. et al. (1994). "Low-Energy Electrons and Their Dynamical Correlation with Recoil Ions for Single Ionization of Helium by Fast, Heavy-Ion Impact". In: *Phys. Rev. Lett.* 73 (25), pp. 3371–3374. URL: http://link.aps.org/doi/10.1103/PhysRevLett.73.3371.

Moshammer, R. et al. (1996). "Double Ionization of Helium and Neon for Fast Heavy-Ion Impact: Correlated Motion of Electrons from Bound to Continuum States". In: *Phys. Rev. Lett.* 77 (7), pp. 1242–1245. URL: http://link.aps.org/doi/10.1103/PhysRevLett.77.1242.

Moshammer, R. et al. (1999). "Initial State Dependence of Low-Energy Electron Emission in Fast Ion Atom Collisions". In: *Phys. Rev. Lett.* 83 (23), pp. 4721–4724. URL: http://link.aps.org/doi/10.1103/PhysRevLett.83.4721.

Moshammer, R. et al. (2001). "Three-Body Coulomb Problem Probed by Mapping the Bethe Surface in Ionizing Ion-Atom Collisions". In: *Phys. Rev. Lett.* 87 (22), p. 223201. URL: http://link.aps.org/doi/10.1103/PhysRevLett.87.223201.

Ngoko Djiokap, J. M. et al. (2010). "Electron-impact ionization excitation of helium in the quasiphoton regime". In: *Phys. Rev. A* 81 (4), p. 042712. URL: http://link.aps.org/doi/10.1103/PhysRevA.81.042712.

NIST Atomic Spectra Database (2013). URL: http://www.nist.gov/pml/data/asd.cfm.

NIST Atomic Weights and Isotopic Compositions (2013). URL: http://www.nist.gov/pml/data/comp.cfm.

Olson, R E and J Fiol (2003). "Dynamics underlying fully differential cross sections for fast C $^{6+}$ + He collisions". In: *Journal of Physics B: Atomic, Molecular and Optical Physics* 36.20, p. L365. URL: http://stacks.iop.org/0953-4075/36/i=20/a=L03.

Olson, R. E. and J. Fiol (2005). "Extreme Sensitivity of Differential Momentum Transfer Cross Sections to Target Atom Initial Conditions". In: *Phys. Rev. Lett.* 95 (26), p. 263203. URL: http://link.aps.org/doi/10.1103/PhysRevLett.95.263203.

Oppenheimer, J. R. (1928). "On the Quantum Theory of the Capture of Electrons". In: *Phys. Rev.* 31 (3), pp. 349–356. URL: http://link.aps.org/doi/10.1103/PhysRev.31.349.

Pálinkás, J. et al. (1989). "Observation of electron-electron scattering in electron capture by fast protons from He". In: *Phys. Rev. Lett.* 63 (22), pp. 2464–2467. URL: http://link.aps.org/doi/10.1103/PhysRevLett.63.2464.

Pflüger, Thomas (2012). "Electron Impact Ionization Studies of Small Rare Gas Clusters". PhD thesis. Ruperto-Carola University of Heidelberg.

Repnow, R. et al. (1974). "The Heidelberg MP tandem Van de Graaff". In: *Nuclear Instruments and Methods* 122.0, pp. 179 –189. ISSN: 0029-554X. URL: http://www.sciencedirect.com/science/article/pii/0029554X74904819.

Rescigno, T. N. et al. (1999). "Collisional Breakup in a Quantum System of Three Charged Particles". In: *Science* 286.5449, pp. 2474–2479. URL: http://www.sciencemag.org/content/286/5449/2474.abstract.

Rodriguez, V. D. and R. O. Barrachina (1998). "Projectile angular distribution in He single ionization by proton impact as a function of the ejected-electron energy". In: *Phys. Rev. A* 57 (1), pp. 215–220. URL: http://link.aps.org/doi/10.1103/PhysRevA.57.215.

ROOT website. Accessed 11/2013. URL: http://root.cern.ch/drupal/.

Rudd, M. E. et al. (1992). "Electron production in proton collisions with atoms and molecules: energy distributions". In: *Rev. Mod. Phys.* 64 (2), pp. 441–490. URL: http://link.aps.org/doi/10.1103/RevModPhys.64.441.

Rutherford, E. (1924). "XXIV. The capture and loss of electrons by α particles". In: *Philosophical Magazine Series 6* 47.278, pp. 277–303. URL: http://www.tandfonline.com/doi/abs/10.1080/14786442408634367.

Sakhelashvili, G. et al. (2005). "Triple Coincidence (e,γ2e) Experiment for Simultaneous Electron Impact Ionization Excitation of Helium". In: *Phys. Rev. Lett.* 95 (3), p. 033201. URL: http://link.aps.org/doi/10.1103/PhysRevLett.95.033201.

Sarkadi, L. (2010). "Classical trajectory Monte Carlo model calculations for ionization of atomic hydrogen by 75-keV proton impact". In: *Phys. Rev. A* 82 (5), p. 052710. URL: http://link.aps.org/doi/10.1103/PhysRevA.82.052710.

Schmidt, L. Ph. H. et al. (2008). "Young-Type Interference in Collisions between Hydrogen Molecular Ions and Helium". In: *Phys. Rev. Lett.* 101 (17), p. 173202. URL: http://link.aps.org/doi/10.1103/PhysRevLett.101.173202.

Schneider, K. et al. (2013). "Role of Projectile Coherence in Close Heavy Ion-Atom Collisions". In: *Phys. Rev. Lett.* 110 (11), p. 113201. URL: http://link.aps.org/doi/10.1103/PhysRevLett.110.113201.

Schneider, Katharina (2012). "Dynamics in charge transfer and ionization processes in fast ion-helium collisions". PhD thesis. Ruperto-Carola University of Heidelberg.

Schöffler, M. (2006). "Grundzustandskorrelationen und dynamische Prozesse untersucht in Ion-Helium Stößen". PhD thesis. Johann Wolfgang Goethe Universität Frankfurt.

Schöffler, M. S. et al. (2013). "Transfer ionization and its sensitivity to the ground-state wave function". In: *Phys. Rev. A* 87 (3), p. 032715. URL: http://link.aps.org/doi/10.1103/PhysRevA.87.032715.

Schuch, R. et al. (1988). "Charge- and angle-correlated inelasticities in collisions of bare fast carbon ions with neon". In: *Phys. Rev. Lett.* 60 (10), pp. 925–928. URL: http://link.aps.org/doi/10.1103/PhysRevLett.60.925.

Schulz, M et al. (2001). "Triply differential single ionization cross sections in coplanar and non-coplanar geometry for fast heavy ion-atom collisions". In: *Journal of Physics B: Atomic, Molecular and Optical Physics* 34.9, p. L305. URL: http://stacks.iop.org/0953-4075/34/i=9/a=104.

Schulz, M. et al. (2003). "Three-dimensional imaging of atomic four-body processes". In: *Nature* 422.6927, pp. 48–50. ISSN: 0028-0836. URL: http://dx.doi.org/10.1038/nature01415.

Schulz, M. et al. (2007). "Reconciliation of measured fully differential single ionization data with the first Born approximation convoluted with elastic scattering". In: *Phys. Rev. A* 76 (3), p. 032712. URL: http://link.aps.org/doi/10.1103/PhysRevA.76.032712.

Schulz, M. et al. (2012). "Strongly Enhanced Backward Emission of Electrons in Transfer and Ionization". In: *Phys. Rev. Lett.* 108 (4), p. 043202. URL: http://link.aps.org/doi/10.1103/PhysRevLett.108.043202.

Schulz, M. et al. (2013). "Comment on 'Singly ionizing 100-MeV/amu C^{6+} + He collisions with small momentum transfer'". In: *Phys. Rev. A* 87 (4), p. 046701. URL: http://link.aps.org/doi/10.1103/PhysRevA.87.046701.

Sell, Martin (2010). "Entwicklung, Aufbau und Test eines ortsempfindlichen Teilchendetektors zur Untersuchung von Stößen zwischen Ionen und lasergekühlten Atomen". MA thesis. Ruperto-Carola University of Heidelberg.

Senftleben, Arne (2009). "Kinematically complete study on electron impact ionisation of aligned hydrogen molecules". PhD thesis. Ruperto-Carola University of Heidelberg.

Sharma, S. et al. (2012). "Projectile coherence effects in electron capture by protons colliding with H_2 and He". In: *Phys. Rev. A* 86 (2), p. 022706. URL: http://link.aps.org/doi/10.1103/PhysRevA.86.022706.

Sidorovich, V. A. et al. (1985). "Calculation of charge-changing cross sections in collisions of H^+, He^{2+} and Li^{3+} with He atoms". In: *Phys. Rev. A* 31 (4), pp. 2193–2201. URL: http://link.aps.org/doi/10.1103/PhysRevA.31.2193.

Slater, J.C. (1930). "Atomic shielding constants". In: *Physical Review* 36.

Steinmann, Jochen (2007). "Multiphoton Ionization of Laser Cooled Lithium". PhD thesis. Ruperto-Carola University of Heidelberg.

Stolterfoht, N. et al. (1998). "Two- and Three-Body Effects in Single Ionization of Li by 95 MeV/u Ar^{18+} Ions: Analogies with Photoionization". In: *Phys. Rev. Lett.* 80 (21), pp. 4649–4652. URL: http://link.aps.org/doi/10.1103/PhysRevLett.80.4649.

Stolterfoht, N. et al. (2001). "Evidence for Interference Effects in Electron Emission from H_2 Colliding with 60 MeV/u Kr^{34+} Ions". In: *Phys. Rev. Lett.* 87 (2), p. 023201. URL: http://link.aps.org/doi/10.1103/PhysRevLett.87.023201.

Tanis, J. A. et al. (1999). "Production of Hollow Lithium by Multielectron Correlation in 95 MeV/nucleon Ar^{18+} + Li Collisions". In: *Phys. Rev. Lett.* 83 (6), pp. 1131–1134. URL: http://link.aps.org/doi/10.1103/PhysRevLett.83.1131.

Taylor, John R. (2006). *Scattering Theory*. www.doverpublications.com.

The ORNL CFADC Redbooks (2014). URL: http://www-cfadc.phy.ornl.gov/redbooks/.

Thomas, L. H. (1927). "On the Capture of Electrons by Swiftly Moving Electrified Particles". English. In: *Proceedings of the Royal Society of London. Series A, Containing Papers of a Mathematical and Physical Character* 114.768, pp. 561–576. ISSN: 09501207. URL: http://www.jstor.org/stable/94828.

Tiecke, T. G. et al. (2009). "High-flux two-dimensional magneto-optical-trap source for cold lithium atoms". In: *Phys. Rev. A* 80 (1), p. 013409. URL: http://link.aps.org/doi/10.1103/PhysRevA.80.013409.

Toptica. *High Power Diode Lasers and Amplifiers*. Accessed: 2013. URL: http://www.toptica.com.

Tuan, T. F. and E. Gerjuoy (1960). "Charge Transfer in Molecular Hydrogen". In: *Phys. Rev.* 117 (3), pp. 756–763. URL: http://link.aps.org/doi/10.1103/PhysRev.117.756.

Ullrich, J and V. Shevelko (2003). *Many-Particle Quantum Dynamics in Atomic and Molecular Fragm.* Springer.

Ullrich, J et al. (1989). "Influence of ionised electrons on heavy nuclei angular differential scattering cross sections". In: *Journal of Physics B: Atomic, Molecular and Optical Physics* 22.4, p. 627. URL: http://stacks.iop.org/0953-4075/22/i=4/a=009.

Ullrich, J. et al. (2003). "Recoil-ion and electron momentum spectroscopy: reaction-microscopes". In: *Reports on Progress in Physics* 66, p. 1463.

Vinitsky, P. S. et al. (2005). "Fast proton-hydrogen charge exchange reaction at small scattering angles". In: *Phys. Rev. A* 71 (1), p. 012706. URL: http://link.aps.org/doi/10.1103/PhysRevA.71.012706.

Vogt, H. et al. (1986). "Experimental Test of Higher-Order Electron-Capture Processes in Collisions of Fast Protons with Atomic Hydrogen". In: *Phys. Rev. Lett.* 57 (18), pp. 2256–2259. URL: http://link.aps.org/doi/10.1103/PhysRevLett.57.2256.

Voitkiv, A. (2013). private communication.

Voitkiv, A B et al. (2003). "On the higher-order effects in target single ionization by bare ions in the perturbative regime". In: *Journal of Physics B: Atomic, Molecular and Optical Physics* 36.12, p. 2591. URL: http://stacks.iop.org/0953-4075/36/i=12/a=316.

Voitkiv, B. et al. (2008). "Mechanism for Electron Transfer in Fast Ion-Atomic Collisions". In: *Phys. Rev. Lett.* 101 (22), p. 223201. URL: http://link.aps.org/doi/10.1103/PhysRevLett.101.223201.

Walker, T. et al. (1992a). "A vortex-force atom trap". In: *Physics Letters A* 163, pp. 309–312.

Walker, T. et al. (1992b). "Spin-polarized spontaneous-force atom trap". In: *Phys. Rev. Lett.* 69 (15), pp. 2168–2171. URL: http://link.aps.org/doi/10.1103/PhysRevLett.69.2168.

Walters, H. R. J. and Colm T. Whelan (2012). "Ionization of He by C^{6+}, C^{6-}, e^- and e^+". In: *Phys. Rev. A* 85 (6), p. 062701. URL: http://link.aps.org/doi/10.1103/PhysRevA.85.062701.

Wang, X. et al. (2011). "Mutual projectile and target ionization in 1-MeV/amu N^{4+} and N^{5+}+He collisions". In: *Phys. Rev. A* 84 (2), p. 022707. URL: http://link.aps.org/doi/10.1103/PhysRevA.84.022707.

Wang, X et al. (2012). "Projectile coherence effects in single ionization of helium". In: *Journal of Physics B: Atomic, Molecular and Optical Physics* 45.21, p. 211001. URL: http://stacks.iop.org/0953-4075/45/i=21/a=211001.

Wiley, W. C. and I. H. McLaren (1955). "Time-of-Flight Mass Spectrometer with Improved Resolution". In: *Phys. Rev. Lett.* 26 (12).

Young, Thomas (1804). "The Bakerian Lecture: Experiments and Calculations Relative to Physical Optics". In: *Philosophical Transactions of the Royal Society of London* 94, pp. 1–16. URL: http://www.jstor.org/stable/107135.

Zatsarinny, Oleg and Klaus Bartschat (2011). "Nonperturbative Treatment of Ionization with Excitation of Helium by Electron Impact". In: *Phys. Rev. Lett.* 107 (2), p. 023203. URL: http://link.aps.org/doi/10.1103/PhysRevLett.107.023203.